Calculation of nonleptonic kaon decay amplitudes from K→π matrix elements in quenched domain-wall QCD

doi: 10.1103/PhysRevD.68.014501

Calculation of nonleptonic kaon decay amplitudes from $K\to\pi$ matrix elements in quenched domain-wall QCD

J. Noaki,[1,*] S. Aoki,[1] Y. Aoki,[1,2,*] R. Burkhalter,[2] S. Ejiri,[2,†] M. Fukugita,[3] S. Hashimoto,[4] N. Ishizuka,[1,2] Y. Iwasaki,[1,2] T. Izubuchi,[5] K. Kanaya,[1,2] T. Kaneko,[4] Y. Kuramashi,[4] V. Lesk,[2] K. I. Nagai,[2,‡] M. Okawa,[4] Y. Taniguchi,[1] A. Ukawa,[1,2] and T. Yoshié[1,2]

(CP-PACS Collaboration)

[1]*Institute of Physics, University of Tsukuba, Tsukuba, Ibaraki 305-8571, Japan*
[2]*Center for Computational Physics, University of Tsukuba, Tsukuba, Ibaraki 305-8577, Japan*
[3]*Institute for Cosmic Ray Research, University of Tokyo, Kashiwa 277-8582, Japan*
[4]*High Energy Accelerator Research Organization (KEK), Tsukuba, Ibaraki 305-0801, Japan*
[5]*Institute of Theoretical Physics, Kanazawa University, Ishikawa 920-1192, Japan*

(Received 17 August 2001; revised manuscript received 25 March 2002; published 3 July 2003)

We explore the application of the domain wall fermion formalism of lattice QCD to calculate the $K\to\pi\pi$ decay amplitudes in terms of the $K^+\to\pi^+$ and $K^0\to 0$ hadronic matrix elements through relations derived in chiral perturbation theory. Numerical simulations are carried out in quenched QCD using the domain-wall fermion action for quarks and a renormalization group-improved gauge action for gluons on a $16^3\times 32\times 16$ and $24^3\times 32\times 16$ lattice at $\beta=2.6$ corresponding to the lattice spacing $1/a\approx 2$ GeV. Quark loop contractions which appear in Penguin diagrams are calculated by the random noise method, and the $\Delta I=1/2$ matrix elements which require subtractions with the quark loop contractions are obtained with a statistical accuracy of about 10%. We investigate the chiral properties required of the $K^+\to\pi^+$ matrix elements. Matching the lattice matrix elements to those in the continuum at $\mu=1/a$ using the perturbative renormalization factor to one loop order, and running to the scale $\mu=m_c=1.3$ GeV with the renormalization group for $N_f=3$ flavors, we calculate all the matrix elements needed for the decay amplitudes. With these matrix elements, the $\Delta I=3/2$ decay amplitude $\mathrm{Re}\,A_2$ shows a good agreement with experiment after an extrapolation to the chiral limit. The $\Delta I=1/2$ amplitude $\mathrm{Re}\,A_0$, on the other hand, is about 50–60 % of the experimental one even after chiral extrapolation. In view of the insufficient enhancement of the $\Delta I=1/2$ contribution, we employ the experimental values for the real parts of the decay amplitudes in our calculation of ε'/ε. The central values of our result indicate that the $\Delta I=3/2$ contribution is larger than the $\Delta I=1/2$ contribution so that ε'/ε is negative and has a magnitude of order 10^{-4}. We discuss in detail possible systematic uncertainties, which seem too large for a definite conclusion on the value of ε'/ε.

DOI: 10.1103/PhysRevD.68.014501 PACS number(s): 11.15.Ha, 12.38.Gc

I. INTRODUCTION

Understanding nonleptonic weak processes of the kaon, in particular, the $K\to\pi\pi$ decay, represents one of the keys to establishing the standard model and probing the physics beyond it. This decay exhibits two significant phenomena: namely, the $\Delta I=1/2$ rule, which is a large enhancement of the decay mode with $\Delta I=1/2$ relative to that with $\Delta I=3/2$, and direct *CP* violation [1,2], which is naturally built in the model for three or more families of quarks [3]. While both of these phenomena are well established by experiment, theoretical calculations with sufficient reliability that allow examinations of the standard model predictions against the experimental results are yet to be made. The main reason for this status is the difficulty in calculating the hadronic matrix elements of local operators which appear in the effective weak Hamiltonian for the decay amplitudes. At the energy scales relevant for these operators, analytic treatments such as the $1/N_c$ expansion are not sufficiently powerful to reliably evaluate the effect of the strong interactions in the matrix elements. In fact, the $\Delta I=1/2$ rule, which is supposed to arise from QCD effects, has not been quantitatively explained by analytic methods so far. With these backgrounds, Monte Carlo simulations of lattice QCD provide a hopeful method for the calculation of the decay amplitudes.

A natural framework for theoretical calculations of the decay amplitudes is provided by the effective weak Hamiltonian H_W, which follows from an operator product expansion (OPE) of weak currents [4]:

$$H_W=\frac{G_F}{\sqrt{2}}V_{\mathrm{us}}V_{\mathrm{ud}}^*\sum_i W_i(\mu)Q_i(\mu). \tag{1.1}$$

Here the Wilson coefficients W_i contain the effects of the energy scales higher than μ so that they can be calculated perturbatively. Nonperturbative QCD effects are contained in

*Present address: RIKEN BNL Research Center, Brookhaven National Laboratory, Upton, NY 11973, USA.
†Present address: Universitaet Bielefeld, Fakultat fuer Physik, Universitaetsstrasse 25, 33615 Bielefeld, Germany.
‡Present address: NIC/DESY Zeuthen, Platanenallee 6, D-15738 Zeuthen, Germany.

the matrix elements of the local operators Q_i, and the calculation of these matrix elements, often called hadronic matrix elements (HME), is the task of lattice QCD [5–8]. Our aim in this paper is to report on our attempt to obtain these matrix elements through numerical simulations of lattice QCD using the domain wall formalism [9–11] for quarks.

The amplitudes for $K\to\pi\pi$ decay with $\Delta I=1/2$ and 3/2 are written as the matrix elements of H_W,

$$\langle(\pi\pi)_I|H_W|K^0\rangle\equiv A_I e^{i\delta_I}, \tag{1.2}$$

where the subscript $I=0$ or 2 denotes the isospin of the final state corresponding to $\Delta I=1/2$ or 3/2, and δ_I is the phase shift from final state interactions $\pi\pi\to\pi\pi$ caused by QCD effects. The $\Delta I=1/2$ rule, which is one of the focuses of our calculation, is described by the ratio of isospin amplitudes A_I:

$$\omega^{-1}\equiv\frac{\mathrm{Re}\,A_0}{\mathrm{Re}\,A_2}\approx 22.2. \tag{1.3}$$

Another focus is the parameter ε'/ε of direct *CP* violation in the standard model. The recent experimental results are

$$\frac{\varepsilon'}{\varepsilon}\equiv\frac{\omega}{\sqrt{2}|\varepsilon|}\left[\frac{\mathrm{Im}\,A_2}{\mathrm{Re}\,A_2}-\frac{\mathrm{Im}\,A_0}{\mathrm{Re}\,A_0}\right]$$
$$=\begin{cases}(20.7\pm 2.8)\times 10^{-4} & (\mathrm{KTeV})[1],\\ (15.3\pm 2.6)\times 10^{-4} & (\mathrm{NA48})[2].\end{cases} \tag{1.4}$$

In the numerical simulation of lattice QCD, matrix elements are generally extracted from Euclidean correlation functions of the relevant operators and those which create the initial and final states in their lowest energy levels. For sufficiently large Euclidean time distances, excited states damp out and the matrix elements of the lowest energy states are left. In fact, the kaon *B* parameter B_K has been successfully obtained from the three-point correlation function of K^0 and $\overline{K^0}$ and an insertion of the $\Delta S=2$ weak Hamiltonian [12]. However, in the calculation of the four-point function, $\langle\pi(t_2)\pi(t_1)H_W(t_H)K(t_K)\rangle$, necessary for the $K\to\pi\pi$ decay, there is a severe limitation as pointed out by Maiani and Testa [13]. They have shown that it is difficult to obtain the matrix elements unless the momentum of each of the two pions in the final state is set to zero.

One of the ways to overcome the difficulty pursued in the past is to calculate the matrix elements with the two pions at rest, allowing a nonzero energy transfer $\Delta E=2m_\pi-m_K$ at the weak operator. This generally causes mixings of unphysical lower dimension operators through renormalization, which has to be removed. (See Ref. [8] and references therein.) Furthermore, the unphysical amplitudes obtained with $\Delta E\neq 0$ need to be extrapolated to physical ones by use of some effective theories such as chiral perturbation theory. Due to these problems and numerical difficulties of extracting reasonable signals from four-point functions, this approach has not been successful for the $\Delta I=1/2$ amplitude despite many efforts over the years [14]. For the $\Delta I=3/2$ amplitude for which the operator mixing is absent, on the other hand, a recent study has obtained a result in agreement with experiment [16].

Several proposals have been presented over the years for extracting the physical amplitude from the four-point functions [17–19]. Feasibility studies for implementing them in practical simulations are yet to come, however.

In this paper we explore a method proposed by Bernard *et al.* [15] which is alternative to calculating the three-point function. In this method, which we shall call as reduction method, chiral perturbation theory (χPT) is used to relate the matrix elements for $K\to\pi\pi$ to those for $K\to\pi$ and $K\to 0$ (vacuum), and the latter amplitudes are calculated in lattice QCD. Since this calculation involves only three- and two-point correlation functions, the Maiani-Testa problem mentioned above is avoided. Statistical fluctuations are also expected to be diminished compared with the case of four-point correlation functions.

Early attempts with this method [14] encountered large statistical fluctuations in the correlation functions so that meaningful results were difficult to obtain. For the Wilson fermion action or its $\mathcal{O}(a)$ improved version, there is an added difficulty that the mixing of operators of wrong chirality caused by explicit chiral symmetry breaking of the action has to be removed. The mixing problem has been resolved only for the $\Delta I=3/2$ operators so far [20–22].

The first results on the $\Delta I=1/2$ rule and ε'/ε calculated with this method were recently reported [23] using the staggered fermion action which keeps the $U(1)$ subgroup of chiral symmetry. In this work, however, a large dependence of the $\Delta I=3/2$ amplitude on the meson mass was seen, which made the chiral extrapolation difficult. Moreover, large uncertainties due to perturbative renormalization factors depending on the value of the matching point were reported. Hence clear statements on the viability of the method were difficult to make from this work.

In this paper we report on our attempt to apply the domain-wall fermion formalism of lattice QCD [9–11] to the calculation of $K\to\pi\pi$ decay amplitudes in the context of the reduction method. A major advantage of this approach over the conventional fermion formalisms is that full chiral symmetry can be expected to be realized for sufficiently large lattice sizes in the fifth dimension. Good chiral property of one of the $K\to\pi$ matrix elements, equivalent to the kaon *B* parameter, was observed in the pioneering application of the formalism [24]. Detailed investigations into the realization of the chiral limit have been made in the quenched approximation for the plaquette and a renormalization group (RG)-improved gluon action [25–27]. It was found that the use of RG-improved action leads to much better chiral properties compared to the case of the plaquette action for similar lattice spacings [26]. This prompts us to adopt the RG-improved action in our simulation.

Another possible advantage of the domain wall formalism is $\mathcal{O}(a^2)$ scaling violation from the fermion sector as opposed to $\mathcal{O}(a)$ for the Wilson case. Indeed our domain wall fermion calculation of B_K [28] exhibits only a small scaling violation. The magnitude of violation is much smaller compared to the staggered fermion case [29] which is also ex-

pected to be $\mathcal{O}(a^2)$. An improved scaling behavior may be enhanced with the use of the RG-improved gluon action.

This paper is organized as follows. In Sec. II, we summarize the main points of the χPT reduction method. For the construction of the formulas which relate the matrix elements for $K\to\pi$ and the $K\to\pi\pi$ decay amplitudes, the relations between the four quark operators Q_i and χPT operators are considered at tree level on the basis of chiral transformation properties. The necessity of chiral symmetry on the lattice is emphasized. In Sec. III we summarize the details of our numerical simulation procedure. We discuss the form of lattice actions and the choice of an optimal set of simulation parameters from the point of view of chiral properties. Some of the technical issues are also explained including renormalization of the four-quark operators and RG-running of the matrix elements to the relevant energy scale. The numerical results are reported in Secs. IV and V. The former contains results of hadronic matrix elements. In particular, we show that the subset of $K\to\pi$ matrix elements which are expected to vanish in the chiral limit satisfy this requirement. We then present the physical matrix elements and combine them with the Wilson coefficients, which are already calculated perturbatively. This leads us to results for the $\Delta I=1/2$ rule and ε'/ε. Our conclusions are given in Sec. VI.

A preliminary report of the present work was presented in Ref. [30]. We refer to Refs. [31,32] for a similar attempt, and Refs. [33,8] for reviews.

II. CHIRAL PERTURBATION THEORY REDUCTION METHOD

A. Local operators

We carry out our analyses choosing the energy scale μ in the OPE for the weak Hamiltonian (1.1) equal to the charm quark mass $m_c=1.3$ GeV. In this case only u,d, and s quarks appear in the local four-quark operators. Conventionally these operators are written as

$$Q_1=[\bar{s}_a\gamma_\mu(1-\gamma_5)u_b][\bar{u}_b\gamma_\mu(1-\gamma_5)d_a], \tag{2.1}$$

$$Q_2=[\bar{s}_a\gamma_\mu(1-\gamma_5)u_a][\bar{u}_b\gamma_\mu(1-\gamma_5)d_b], \tag{2.2}$$

$$Q_3=[\bar{s}_a\gamma_\mu(1-\gamma_5)d_a]\sum_q\,[\bar{q}_b\gamma_\mu(1-\gamma_5)q_b], \tag{2.3}$$

$$Q_4=[\bar{s}_a\gamma_\mu(1-\gamma_5)d_b]\sum_q\,[\bar{q}_b\gamma_\mu(1-\gamma_5)q_a], \tag{2.4}$$

$$Q_5=[\bar{s}_a\gamma_\mu(1-\gamma_5)d_a]\sum_q\,[\bar{q}_b\gamma_\mu(1+\gamma_5)q_b], \tag{2.5}$$

$$Q_6=[\bar{s}_a\gamma_\mu(1-\gamma_5)d_b]\sum_q\,[\bar{q}_b\gamma_\mu(1+\gamma_5)q_a], \tag{2.6}$$

$$Q_7=\frac{3}{2}[\bar{s}_a\gamma_\mu(1-\gamma_5)d_a]\sum_q\,e_q[\bar{q}_b\gamma_\mu(1+\gamma_5)q_b], \tag{2.7}$$

$$Q_8=\frac{3}{2}[\bar{s}_a\gamma_\mu(1-\gamma_5)d_b]\sum_q\,e_q[\bar{q}_b\gamma_\mu(1+\gamma_5)q_a], \tag{2.8}$$

$$Q_9=\frac{3}{2}[\bar{s}_a\gamma_\mu(1-\gamma_5)d_a]\sum_q\,e_q[\bar{q}_b\gamma_\mu(1-\gamma_5)q_b], \tag{2.9}$$

$$Q_{10}=\frac{3}{2}[\bar{s}_a\gamma_\mu(1-\gamma_5)d_b]\sum_q\,e_q[\bar{q}_b\gamma_\mu(1-\gamma_5)q_a], \tag{2.10}$$

where the indices a,b denote color, and the summation over q appearing in Q_3 to Q_{10} runs over the three light flavors, $q=u,d,s$, with the charge $e_u=2/3$ and $e_d=e_s=-1/3$.

With the use of Fierz rearrangements, one can derive the relations,

$$Q_4=Q_2+Q_3-Q_1, \tag{2.11}$$

$$Q_9=\frac{3}{2}Q_1-\frac{1}{2}Q_3, \tag{2.12}$$

$$Q_{10}=\frac{3}{2}Q_2-\frac{1}{2}Q_4=Q_2-\frac{1}{2}Q_3+\frac{1}{2}Q_1. \tag{2.13}$$

Hence Q_4, Q_9, and Q_{10} are not independent operators. We emphasize that these relations do not hold in general d-dimensions where Fierz rearrangements cannot be used.

In terms of the irreducible representations of the chiral $SU(3)_L\otimes SU(3)_R$ group, Q_i's are classified as

$$Q_1,Q_2,Q_9,Q_{10}:\quad (27_L,1_R)\oplus(8_L,1_R), \tag{2.14}$$

$$Q_3,Q_4,Q_5,Q_6:\quad (8_L,1_R), \tag{2.15}$$

$$Q_7,Q_8:\quad (8_L,8_R). \tag{2.16}$$

The operators $Q_i(i=1,\ldots,10)$ are invariant under *CPS* symmetry, i.e., the product of *CP* transformation and $d\leftrightarrow s$ interchange. A basis of operators which are irreducible under chiral symmetry and invariant under *CPS* is given by

$$(8_L,1_R):X_1=(\bar{s}d)_L(\bar{u}u)_L-(\bar{s}u)_L(\bar{u}d)_L, \tag{2.17}$$

$$(8_L,1_R):X_2=(\bar{s}d)_L[(\bar{u}u)_L+2(\bar{d}d)_L+2(\bar{s}s)_L]+(\bar{s}u)_L(\bar{u}d)_L, \tag{2.18}$$

$$(27_L,1_R):X_3=(\bar{s}d)_L[2(\bar{u}u)_L-(\bar{d}d)_L-(\bar{s}s)_L]+2(\bar{s}u)_L(\bar{u}d)_L, \tag{2.19}$$

$$(8_L,1_R):Y_1=(\bar{s}d)_L[(\bar{u}u)_R+(\bar{d}d)_R+(\bar{s}s)_R],\quad {Y_1}^c, \tag{2.20}$$

$$(8_L,8_R):Y_2=(\bar{s}d)_L[2(\bar{u}u)_R-(\bar{d}d)_R-(\bar{s}s)_R],\quad {Y_2}^c, \tag{2.21}$$

where $(\bar{s}d)_L=\bar{s}\gamma_\mu(1-\gamma_5)d$ and $(\bar{s}d)_R=\bar{s}\gamma_\mu(1+\gamma_5)d$. The color and spinor indices are summed within each current except for ${Y_i}^c$ for which the color summation is taken across

the two currents. While X_i's have the Lorentz structure of $L\otimes L$, Y_i's have that of $L\otimes R$. All the independent local operators are written as linear combinations of these operators:

$$Q_1=\frac{1}{2}X_1+\frac{1}{10}X_2+\frac{1}{5}X_3, \tag{2.22}$$

$$Q_2=-\frac{1}{2}X_1+\frac{1}{10}X_2+\frac{1}{5}X_3, \tag{2.23}$$

$$Q_3=\frac{1}{2}X_1+\frac{1}{2}X_2, \tag{2.24}$$

$$Q_5=Y_1, \tag{2.25}$$

$$Q_6={Y_1}^c, \tag{2.26}$$

$$Q_7=\frac{1}{2}Y_2, \tag{2.27}$$

$$Q_8=\frac{1}{2}Y_2^c. \tag{2.28}$$

The expressions for the dependent operators $Q_{4,9,10}$ are easily derived using Eqs. (2.11)–(2.13).

The final states in the $K\to\pi\pi$ decay can have either isospin $I=0$ or 2, i.e., $\Delta I=1/2$ or 3/2. Hence Q_i's are decomposed as

$$Q_i=Q_i^{(0)}+Q_i^{(2)}. \tag{2.29}$$

This decomposition is accomplished by constructing another basis of irreducible representations with the intrinsic isospin I. The details are described in Appendix A.

B. Chiral perturbation theory

In the low energy region of strong interactions, the octet of pseudoscalar mesons $\pi^0,\pi^\pm,K^0,\overline{K^0},K^\pm,\eta$ play a principal role as the Nambu-Goldstone bosons of spontaneously broken chiral symmetry $SU(3)_L\otimes SU(3)_R\to SU(3)_V$. In chiral perturbation theory (χPT) as a low energy effective theory of QCD, these Nambu-Goldstone boson fields are used to parametrize the broken axial symmetry, and we collect them in a 3×3 matrix,

$$\Sigma=(e^{i\Phi/f}), \tag{2.30}$$

$$\Phi=\sum_a \lambda^a\phi^a = \begin{bmatrix} \frac{1}{\sqrt{2}}\pi^0+\frac{1}{\sqrt{6}}\eta^0 & \pi^+ & K^+ \\ \pi^- & -\frac{1}{\sqrt{2}}\pi^0+\frac{1}{\sqrt{6}}\eta^0 & K^0 \\ K^- & \overline{K^0} & -\frac{2}{\sqrt{6}}\eta^0 \end{bmatrix}, \tag{2.31}$$

where λ^a are Gell-Mann matrices, and f is the decay constant. Under $SU(3)_L\otimes SU(3)_R$ chiral transformation, $\Sigma\in SU(3)$ transforms as

$$\Sigma\to g_R\Sigma g_L^\dagger,\quad \Sigma^\dagger\to g_L\Sigma^\dagger g_R^\dagger. \tag{2.32}$$

The chiral Lagrangian to the lowest order, with the additional mass term, is given by

$$\mathcal{L}_\chi=\frac{f^2}{4}\mathrm{tr}(\partial_\mu\Sigma^\dagger\partial_\mu\Sigma)-\frac{f^2}{4}\mathrm{tr}[M(\Sigma^\dagger+\Sigma)], \tag{2.33}$$

where $M=(2B_0)\cdot\mathrm{diag}[m_u,m_d,m_s]$ denotes the quark mass matrix and B_0 is a parameter. In terms of Σ, the left- and right-handed currents are given by

$$(L_\mu)^i_j=\frac{i}{2}f^2(\partial_\mu\Sigma^\dagger\cdot\Sigma)^j_i,\ (R_\mu)^i_j=\frac{i}{2}f^2(\partial_\mu\Sigma\cdot\Sigma^\dagger)^j_i, \tag{2.34}$$

respectively.

The idea of the χPT reduction method by Bernard *et al.* [15] is to relate the hadronic matrix elements for $K\to\pi\pi$ decays to those for $K\to\pi$ and $K\to0$ (vacuum) using χPT, and calculate the latter through numerical simulations of lattice QCD. As the first step of the χPT reduction method, we construct operators in χPT which correspond to X_i's and Y_i's in QCD, i.e., those which transform under the same irreducible representations of $SU(3)_L\otimes SU(3)_R$ and invariant under *CPS* symmetry. In the following, we discuss the case of $\{(27_L,1_R),(8_L,1_R)\}$ and $(8_L,8_R)$ representations separately.

C. Reduction method for $(27_L,1_R)$ and $(8_L,1_R)$ operators

For the irreducible representations $(27_L,1_R)$ and $(8_L,1_R)$, which cover $Q_1,\ldots,Q_6,Q_9$ and Q_{10}, the product of left-handed currents $(L_\mu)^i_j(L_\mu)^k_l$ is one of the candidates for the operator to the lowest order in χPT. An explicit form of the operators, which are also *CPS* invariant, is given by

$$(8_L,1_R):\mathbf{A}=(L_\mu)^i_3(L_\mu)^2_i, \tag{2.35}$$

$$(27_L,1_R):\mathbf{C}=3(L_\mu)^2_3(L_\mu)^1_1+2(L_\mu)^1_3(L_\mu)^2_1, \tag{2.36}$$

where $\mathbf{A}$ corresponds to X_1 or X_2, while $\mathbf{C}$ is the counterpart of X_3. The latter is decomposed into two parts with $I=0$ and 2 in the same way as X_3 (see Appendix A):

$$\mathbf{C}=\frac{1}{3}\mathbf{C}^{(0)}+\frac{5}{3}\mathbf{C}^{(2)}, \tag{2.37}$$

where

$$\mathbf{C}^{(0)}=(L_\mu)^1_1(L_\mu)^2_3+(L_\mu)^2_1(L_\mu)^1_3+2(L_\mu)^2_2(L_\mu)^2_3-3(L_\mu)^3_3(L_\mu)^2_3, \tag{2.38}$$

$$\mathbf{C}^{(2)}=(L_\mu)^1_1(L_\mu)^2_3+(L_\mu)^2_1(L_\mu)^1_3-(L_\mu)^2_2(L_\mu)^2_3. \tag{2.39}$$

In addition to the operators above, there is another $(8_L,1_R)$ operator which is allowed from *CPS* invariance:

$$
\begin{aligned}
(8_L,1_R)\ :\ \mathbf{B} &= (\Sigma M + M\Sigma^\dagger)_3^2 \\
&= B_0(m_s+m_d)(\Sigma+\Sigma^\dagger)_3^2 \\
&\quad - B_0(m_s-m_d)(\Sigma-\Sigma^\dagger)_3^2 \\
&= -i\frac{4}{f^2}\partial_\mu\left[\frac{m_s+m_d}{m_s-m_d}(V_\mu)_3^2 - \frac{m_s-m_d}{m_s+m_d}(A_\mu)_3^2\right],
\end{aligned}
\tag{2.40}
$$

where $V_\mu=(R_\mu+L_\mu)/2$ and $A_\mu=(R_\mu-L_\mu)/2$ are vector and axial vector currents with L_μ and R_μ defined in Eq. (2.34). The equation of motion for Σ is used to derive the third line from the second line in Eq. (2.40).

The counterpart of this operator for QCD can be obtained easily by $SU(3)_L\otimes SU(3)_R$ and *CPS* symmetry,

$$
\begin{aligned}
Q_{\rm sub} &= (m_s+m_d)\bar{s}d - (m_s-m_d)\bar{s}\gamma_5 d \\
&= \partial_\mu\left[\frac{m_s+m_d}{m_s-m_d}\bar{s}\gamma_\mu d - \frac{m_s-m_d}{m_s+m_d}\bar{s}\gamma_\mu\gamma_5 d\right],
\end{aligned}
\tag{2.41}
$$

where the equation of motion for s and d quark fields is used.

For physical $K\to\pi\pi$ processes, $Q_{\rm sub}$, and hence **B**, do not contribute since these operators are a total derivative of local operators and the energy-momentum injected at the weak operator vanishes. However, for the unphysical processes such as $K\to\pi$ and $K\to 0$ (vacuum) which we are to calculate on the lattice, the matrix elements of $Q_{\rm sub}$ or **B** do not vanish due to a finite energy-momentum transfer for $m_s\neq m_d$. Therefore a mixing between Q_i's and $Q_{\rm sub}$ in $K\to\pi$ matrix elements exists which should be removed. We should also note that this mixing inevitably arises in the case of $m_d=m_s$, as is often chosen in numerical simulations on the lattice, since $Q_{\rm sub}$ is not a total divergence for this case.

We assume that there are linear relations in the sense of matrix elements between the local operators $\{Q_i(i=1,\ldots,6,9,10),Q_{\rm sub}\}$ and $\{\mathbf{A},\mathbf{B},\mathbf{C}\}$ which belong to the same representations, i.e., $\{(27_L,1_R),(8_L,1_R)\}$:

$$
Q_i^{(0)} = a_i\mathbf{A} + b_i\mathbf{B} + c_i^{(0)}\mathbf{C}^{(0)}, \tag{2.42}
$$

$$
Q_{\rm sub} = r\mathbf{B}, \tag{2.43}
$$

$$
Q_i^{(2)} = c_i^{(2)}\mathbf{C}^{(2)}, \tag{2.44}
$$

where the coefficients $a_i, b_i, c_i^{(I)}$, and r are unknown parameters. Taking the matrix elements of the two sides of Eqs. (2.42), (2.43) and (2.44) for $K^0\to 0$, $K^+\to\pi^+$, and $K^0\to\pi^+\pi^-$, one obtains

$$
\langle 0|Q_i^{(0)} - \alpha_i Q_{\rm sub}|K^0\rangle = 0, \tag{2.45}
$$

$$
\langle\pi^+|Q_i^{(0)} - \alpha_i Q_{\rm sub}|K^+\rangle = \frac{2p_K\cdot p_\pi}{f^2}(a_i - c_i^{(0)}) + \mathcal{O}(p^4), \tag{2.46}
$$

$$
\langle\pi^+|Q_i^{(2)}|K^+\rangle = -\frac{2p_K\cdot p_\pi}{f^2}c_i^{(2)} + \mathcal{O}(p^4), \tag{2.47}
$$

$$
\langle\pi^+\pi^-|Q_i^{(0)}|K^0\rangle = \frac{\sqrt{2}}{f^3}(m_K^2-m_\pi^2)(a_i - c_i^{(0)}) + \mathcal{O}(p^4), \tag{2.48}
$$

$$
\langle\pi^+\pi^-|Q_i^{(2)}|K^0\rangle = -\frac{\sqrt{2}}{f^3}(m_K^2-m_\pi^2)c_i^{(2)} + \mathcal{O}(p^4), \tag{2.49}
$$

where $\alpha_i\equiv b_i/r$ in Eqs. (2.45) and (2.46), p_K and p_π are the momenta of kaon and pion, respectively, and p denotes either of them. In Eqs. (2.48) and (2.49), m_K and m_π are the physical meson masses. After eliminating $a_i - c_i^{(0)}$ from Eqs. (2.46) and (2.48), we arrive at the relation between $\langle\pi^+\pi^-|Q_i^{(0)}|K^0\rangle$ and $\langle\pi^+|Q_i^{(0)}|K^+\rangle$ in the $I=0$ case:

$$
\begin{aligned}
\langle\pi^+\pi^-|Q_i^{(0)}|K^0\rangle &= \frac{(m_K^2-m_\pi^2)}{\sqrt{2}f(p_K\cdot p_\pi)}\langle\pi^+|Q_i^{(0)} - \alpha_i Q_{\rm sub}|K^+\rangle \\
&\quad + \mathcal{O}(p^2),
\end{aligned}
\tag{2.50}
$$

$$
\alpha_i = \frac{\langle 0|Q_i^{(0)}|K^0\rangle}{\langle 0|Q_{\rm sub}|K^0\rangle}, \quad i=1,\ldots,6,9,10. \tag{2.51}
$$

The $K\to 0$ (vacuum) matrix elements are used only to determine the α_i's which govern the subtraction of unphysical contributions originating from $Q_{\rm sub}$. The relation for the $I=2$ case is derived in the same way from Eqs. (2.47) and (2.49):

$$
\begin{aligned}
\langle\pi^+\pi^-|Q_i^{(2)}|K^0\rangle &= \frac{(m_K^2-m_\pi^2)}{\sqrt{2}f(p_K\cdot p_\pi)}\langle\pi^+|Q_i^{(2)}|K^+\rangle \\
&\quad + \mathcal{O}(p^2), \quad i=1,\ldots,6,9,10.
\end{aligned}
\tag{2.52}
$$

Let us note that the essential point of the reduction method is a calculation of the parameters $a_i - c_i^{(0)}$ and $c_i^{(2)}$ from $K\to\pi$ three-point correlation functions in numerical simulations of lattice QCD. Since these parameters appear in Eqs. (2.46) and (2.47) as the coefficients of $p_K\cdot p_\pi$, their values are sensitive to the chiral properties of the $K\to\pi$ matrix elements on the left-hand side of these equations. Hence $SU(3)_L\otimes SU(3)_R$ chiral symmetry on the lattice is an indispensable requirement for a successful calculation using this method.

D. Reduction method for $(8_L,8_R)$ operators

In order to construct $(8_L,8_R)$ operators in χPT, we observe that $(\Sigma)_j^i(\Sigma^\dagger)_l^k$ transforms as $(8_R,8_L)$ [34–36] where (j,k) and (l,i) correspond to 8_L and 8_R, respectively. One finds a *CPS* invariant operator

$$\mathbf{D}=3\Sigma_3^1(\Sigma^\dagger)_1^2 \tag{2.53}$$

as the counterpart of Y_2. The decomposition into the $I=0$ and 2 part is given by

$$\mathbf{D}=\mathbf{D}^{(0)}+\mathbf{D}^{(2)}, \tag{2.54}$$

$$\mathbf{D}^{(0)}=2\Sigma_3^1(\Sigma^\dagger)_1^2-\Sigma_3^2(\Sigma^\dagger)_1^1+\Sigma_3^2(\Sigma^\dagger)_2^2, \tag{2.55}$$

$$\mathbf{D}^{(2)}=\Sigma_3^1(\Sigma^\dagger)_1^2+\Sigma_3^2(\Sigma^\dagger)_1^1-\Sigma_3^2(\Sigma^\dagger)_2^2. \tag{2.56}$$

Assuming linear relations between $\{Q_7^{(I)},Q_8^{(I)}\}$ and $\mathbf{D}^{(I)}$'s,

$$Q_i^{(0)}=d_i^{(0)}\mathbf{D}^{(0)},\quad Q_i^{(2)}=d_i^{(2)}\mathbf{D}^{(2)}\quad (i=7,8), \tag{2.57}$$

with the unknown parameters $d_i^{(I)}$'s, we take the matrix elements of the two sides for $K\to\pi\pi$ and $K\to\pi$ to obtain

$$\begin{aligned}
&\langle\pi^+|Q_i^{(0)}|K^+\rangle=4d_i^{(0)}/f^2+\mathcal{O}(p^2),\\
&\langle\pi^+\pi^-|Q_i^{(0)}|K^0\rangle=-2\sqrt{2}d_i^{(0)}/f^3+\mathcal{O}(p^2),\\
&\langle\pi^+|Q_i^{(2)}|K^+\rangle=2d_i^{(2)}/f^2+\mathcal{O}(p^2),\\
&\langle\pi^+\pi^-|Q_i^{(2)}|K^0\rangle=-\sqrt{2}d_i^{(2)}/f^3+\mathcal{O}(p^2).
\end{aligned} \tag{2.58, 2.59}$$

These relations lead to the reduction formulas for $(8_L,8_R)$ operators, namely,

$$\langle\pi^+\pi^-|Q_i^{(I)}|K^0\rangle=-\frac{1}{\sqrt{2}f}\langle\pi^+|Q_i^{(I)}|K^+\rangle+\mathcal{O}(p^2),\quad i=7,8 \tag{2.60}$$

which is common for the $I=0$ and 2 components.

III. DETAILS OF SIMULATIONS

A. Lattice actions

The RG-improved gauge action we use is defined by

$$S_{\text{gluon}}=\frac{1}{g^2}\left\{c_0\sum_{\text{plaquette}}\text{Tr}\,U_{\text{pl}}+c_1\sum_{1\times2\ \text{rectangle}}\text{Tr}\,U_{\text{rtg}}\right\}, \tag{3.1}$$

where the coefficients of the plaquette and 1×2 Wilson loop terms take the values $c_0=3.648$ and $c_1=-0.331$ [37]. This action is expected to lead to a faster approach of physical observables to the continuum limit than with the unimproved plaquette gauge action.

In order to satisfy the requirement of chiral symmetry on the lattice, we use the domain-wall formalism [9] for the quark action. Adopting the Shamir's formulation [10,11], the action is written as

$$S_F=-\sum_{xy,st}\overline{\psi}_s(x)D_{st}^{DW}(x,y)\psi_t(y), \tag{3.2}$$

$$D^{DW}=D^W+D^5, \tag{3.3}$$

$$\begin{aligned}
D_{st}^W(x,y)=\sum_\mu\Bigg[&\frac{r-\gamma_\mu}{2a}U_\mu(x)\,\delta(x+\hat{\mu}-y)\\
&+\frac{r+\gamma_\mu}{2a}U_\mu^\dagger(x-\hat{\mu})\,\delta(x-\hat{\mu}-y)\Bigg]\delta_{st}\\
&+\frac{M-4r}{a}\delta(x-y)\,\delta_{st},
\end{aligned} \tag{3.4}$$

$$\begin{aligned}
D_{st}^5(x,y)=&\left[\frac{1-\gamma_5}{2a_5}\delta_{s+1,t}+\frac{1+\gamma_5}{2a_5}\delta_{s-1,t}\right]\delta(x-y)\\
&-\frac{1}{a_5}\delta(x-y)\,\delta_{st},
\end{aligned} \tag{3.5}$$

where D^W is the ordinary Wilson-Dirac operator in four dimensions, M is the domain-wall height which has to be adjusted to ensure the existence of chiral modes, e.g., $0<M<2$ at tree level, and r is the Wilson parameter which we choose to be unity. The operator D^5 is the extended part in the fifth direction in which the coordinate is bounded by $1\leqslant s,t\leqslant N_5$.

Using the chirality projection operators

$$P_L=\frac{1-\gamma_5}{2},\quad P_R=\frac{1+\gamma_5}{2}, \tag{3.6}$$

quark fields are defined by

$$q(x)=P_L\psi_1(x)+P_R\psi_{N_5}(x), \tag{3.7}$$

$$\overline{q}(x)=\overline{\psi}_{N_5}(x)P_L+\overline{\psi}_1(x)P_R, \tag{3.8}$$

and their mass m_f is introduced as a parameter in the boundary condition in the fifth direction:

$$\psi_{N_5+1}(x)=m_f a\psi_1(x),\quad \psi_0(x)=m_f a\psi_{N_5}(x). \tag{3.9}$$

The operators Q_i and Q_{sub} in our numerical simulation are constructed from q and $\overline{q}$ only, by identifying u, d, and s with q_u, q_d, and q_s.

Axial vector transformations in five dimensions are defined as

$$\begin{aligned}
&\delta\psi_s(x)=iQ(s)\lambda^a\epsilon_s^a(x)\psi_s(x),\\
&\delta\overline{\psi}_s(x)=-i\overline{\psi}_s(x)Q(s)\lambda^a\epsilon_s^a(x),
\end{aligned} \tag{3.10}$$

where $Q(s)=\text{sign}(2N_5-s+1)$ and $\epsilon_s^a(x)$ is an infinitesimal parameter. This definition leads to the variation

$$\delta q(x)=i\gamma_5\lambda^a\epsilon^a(x)q(x), \tag{3.11}$$

$$\delta\overline{q}(x)=i\overline{q}(x)\gamma_5\lambda^a\epsilon^a(x), \tag{3.12}$$

in terms of quark fields, and the axial-vector current takes the form

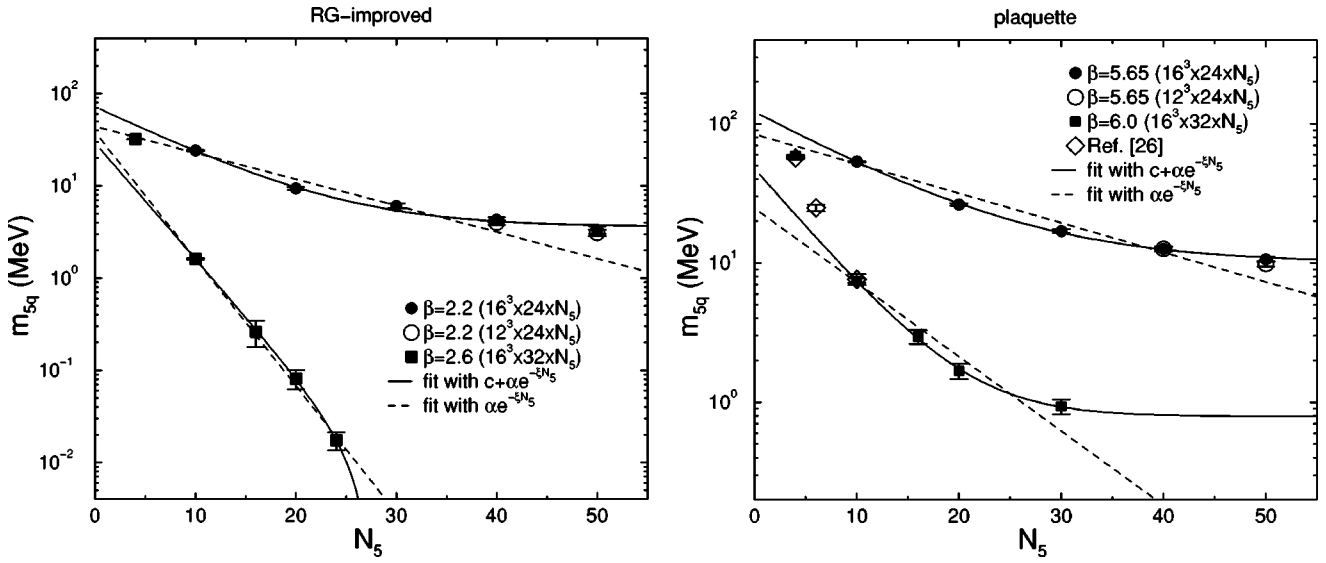

FIG. 1. (Left) Anomalous quark mass m_{5q} as a function of N_5 in the $m_f a \to 0$ limit for the RG-improved action. Filled (empty) circles represent data at $(\beta,M)=(2.2,1.7)$ on a $16^3(12^3)\times 24$ lattice. Filled squares are those at $(\beta,M)=(2.6,1.8)$ on a $16^3\times 32$ lattice. For the latter, data at four larger N_5 are used for fits with the functions $\alpha e^{-\xi N_5}$ (dotted line) and $c+\alpha e^{-\xi N_5}$ (solid line). (Right) Same for the plaquette action at $(\beta,M)=(5.65,1.7)$ and (6.0, 1.8).

$$A_\mu^a(x) \equiv \sum_{s=1}^{N_5} Q(s) \frac{1}{2} [\bar{\psi}_s(x)(1-\gamma_\mu) U_\mu(x) \lambda^a \psi_s(x+\hat{\mu}) + \bar{\psi}_s(x+\hat{\mu})(1+\gamma_\mu) U_\mu^\dagger(x) \lambda^a \psi_s(x)]. \tag{3.13}$$

Taking the divergence of A_μ^a, one obtains

$$\nabla_\mu A_\mu^a(x) = 2 J_{5q}^a(x) + 2 m_f a P^a \tag{3.14}$$

with

$$J_{5q}^a(x) = \bar{\psi}_{N_5/2}(x) P_L \lambda^a \psi_{N_5/2+1}(x) - \bar{\psi}_{N_5/2+1}(x) P_R \lambda^a \psi_{N_5/2}(x) \tag{3.15}$$

and

$$P^a = \bar{q}(x) \lambda^a \gamma_5 q(x). \tag{3.16}$$

The axial vector current A_μ^a does not conserve automatically even in the chiral limit $m_f \to 0$ due to the first term J_{5q} on the right-hand side. Effects of this breaking term, however, are expected to vanish as $N_5 \to \infty$. In practice it is necessary to determine the value of N_5 for a given set of lattice parameters and a type of gluon action, so that the chiral breaking effect due to this term is acceptably small.

In Refs. [26,27], the chiral property of the domain-wall fermion was investigated in detail in the quenched numerical simulation. Defining an anomalous quark mass by [26]

$$m_{5q} a \equiv \frac{\langle 0 | \sum_{\mathbf{x}} J_{5q}^a(\mathbf{x},t) P^b(0) | 0 \rangle}{\langle 0 | \sum_{\mathbf{x}} P^a(\mathbf{x},t) P^b(0) | 0 \rangle}, \tag{3.17}$$

the axial Ward-Takahashi identity (3.14) yields

$$\nabla_\mu \left\langle \sum_{\mathbf{x}} A_\mu^a(x) P^b(0) \right\rangle = 2a(m_f + m_{5q}) \left\langle \sum_{\mathbf{x}} P^a(x) P^b(0) \right\rangle. \tag{3.18}$$

In Fig. 1, we quote results of m_{5q} as a function of N_5 from Refs. [25,26]. In the right panel data from the standard plaquette gluon action for $a^{-1} \approx 1$ GeV (circles, $\beta=5.65$) and $a^{-1} \approx 2$ GeV (squares, $\beta=6.0$) are summarized with two types of exponential fits. The counterparts from the RG-improved gluon action are found in the left panel, where $\beta=2.2$ and 2.6 correspond to $a^{-1} \approx 1$ and 2 GeV, respectively. The anomalous quark mass for the RG-improved action is an order of magnitude smaller than that for the plaquette action for both $a^{-1} \approx 1$ and 2 GeV. This clearly demonstrates the advantage of the use of RG-improved gluon action, which we therefore adopt in our work.

B. Simulation parameters

Our numerical simulations are carried out in the quenched approximation at the inverse gauge coupling of $\beta=2.6$. From the string tension $\sqrt{\sigma}=440$ MeV [38–40], this value of β corresponds to

$$1/a = 1.94(7) \ \text{GeV}, \tag{3.19}$$

which we adopt in our analyses. If we use other quantities such as the rho meson mass or the pion decay constant to determine the scale, the lattice spacing is different from the above value, due to the quenched ambiguity as well as the scaling violation. We do not include such an ambiguity of a in the systematic uncertainty of our results.

TABLE I. Number of gauge configurations, independently generated for each value of $m_f a$, in our numerical simulation.

$m_f a$	$16^3\times 32$	$24^3\times 32$
0.02	407	432
0.03	406	200
0.04	406	200
0.05	432	200
0.06	435	200

Denoting the five-dimensional lattice size as $N_s^3\times N_t\times N_5$, we choose the fifth-dimensional length to be $N_5=16$ and the domain wall height of the quark action to be $M=1.8$. For these parameter choices the anomalous quark mass at $\beta=2.6$ is given by $m_{5q}=0.283(42)$ MeV [26]. We expect this magnitude to be sufficiently small for viability of the χPT reduction formulas. Chiral properties of matrix elements will be discussed in detail in Sec. IV A.

To investigate the effect of finite spatial volume $V=N_s^3$, two sizes of lattices given by $N_s=16$ and 24 are examined, in both cases using the temporal size $N_t=32$.

We work with degenerate quark masses for u,d, and s quarks, and denote the common bare quark mass as $m_f=m_u=m_d=m_s$. Matrix elements are evaluated for the bare quark masses $m_f a=0.02,0.03,0.04,0.05$, and 0.06. Masses and decay constants of the pseudoscalar meson calculated on the lattice, which are common for pion and kaon, are denoted as m_M and f_M.

Gauge configurations are generated by combining one sweep of the five-hit pseudo heat bath algorithm and four overrelaxation sweeps, which we call an iteration. We skip 200 iterations between configurations for measurements. In Table I, the numbers of configurations used in our analyses are given.

We emphasize that *we generate gauge configurations independently for each value of* $m_f a$. This is practically feasible since most of the computer time in our runs is spent in calculating quark propagators. A clear advantage is a removal of correlations between data at different values of m_f, and hence a more reliable control of the chiral extrapolation as a function of m_f or meson mass squared m_M^2 on the basis of χ^2 fitting of data. For error analyses at each m_f a single elimination jackknife estimation is employed throughout the present work.

Table II shows m_M^2 for both sizes of $16^3\times 32$ and $24^3\times 32$. The intercepts in m_f and m_M^2 are obtained by taking a linear extrapolation. Values of m_f in the limit of $m_M^2\to 0$ are 0.95(62) MeV and 1.09(31) MeV on $16^3\times 32$ and $24^3\times 32$ lattices, respectively. These values are larger than the value $m_{5q}=0.283(42)$ MeV at $m_f=0$. As pointed out in Ref. [26], the discrepancy between the direct measurement of m_{5q} and the estimate from the pion mass is largely explained by finite spatial size effects on the pion mass. We use m_M^2 as a variable in our chiral extrapolation throughout this paper. We have checked that our results remain identical within estimated statistical errors if m_f is used in chiral fits.

TABLE II. Lattice pseudoscalar meson mass squared m_M^2 [GeV^2] at each $m_f a$. The x and y intercepts are obtained through a linear chiral extrapolation. Physical scale of lattice spacing equals $1/a=1.94$ GeV determined by $\sqrt{\sigma}=440$ MeV.

$16^3\times 32$		$24^3\times 32$	
$m_f a$	m_M^2[GeV^2]	$m_f a$	m_M^2[GeV^2]
−0.00049(32)	0.00	−0.00056(16)	0.00
0.00	0.0059(37)	0.00	0.0066(19)
0.02	0.2434(26)	0.02	0.2445(11)
0.03	0.3568(29)	0.03	0.3534(17)
0.04	0.4741(28)	0.04	0.4714(19)
0.05	0.5932(29)	0.05	0.5957(19)
0.06	0.7134(30)	0.06	0.7158(20)

C. Calculation of matrix elements

In Fig. 2 we display the quark line diagrams of three- and two-point correlation functions needed for our simulation. Filled squares represent the weak operator $Q_i^{(I)}$ or $Q_{\rm sub}$ located at the site $(\mathbf{x},t)$. Crosses are meson operators. We fix gauge configurations to the Coulomb gauge. A wall source for pion is placed at $t=0$ and that for kaon at $t=T\equiv N_t-1$. Quark propagators are solved by the conjugate gradient algorithm, imposing the Dirichlet boundary condition in time and the periodic boundary condition in space. The stopping condition is given by

$$||(D+m)\cdot x-b||^2<10^{-9}||b||^2, \tag{3.20}$$

where b is the source vector, x is the solution vector, and D is the lattice fermion operator. With this stopping condition a precision of better than 0.1% is achieved for arbitrary elements of three-point correlation functions.

The three-point correlation functions for $K\to\pi$ matrix elements have the contractions of Figs. 2(a), 2(b), and 2(d). For calculating the $I=0$ amplitudes $\langle\pi^+|Q_i^{(0)}|K^+\rangle$, both the figure-eight contraction of 2(a) and the eye contraction of 2(b) are needed, while for the $I=2$ amplitudes $\langle\pi^+|Q_i^{(2)}|K^+\rangle$ only the figure-eight contributes. Writing $\mathcal{O}(t)=1/V\Sigma_{\mathbf{x}}\mathcal{O}(\mathbf{x},t)$, we extract the matrix elements from calculation of the ratio of form

$$\frac{\langle 0|\pi^+(T)Q_i^{(I)}(t)(K^+)^\dagger(0)|0\rangle}{\langle 0|\pi^+(T)A_4(t)|0\rangle\langle 0|A_4(t)(K^+)^\dagger(0)|0\rangle} \overset{T\gg t\gg 1}{\simeq} \frac{\langle\pi^+|Q_i^{(I)}|K^+\rangle}{\langle\pi^+|A_4|0\rangle\langle 0|A_4|K^+\rangle} \tag{3.21}$$

$$=\frac{1}{2m_M^2 f_M^2}\times\langle\pi^+|Q_i^{(I)}|K^+\rangle. \tag{3.22}$$

We note that a local current $A_\mu(x)=\overline{q}(x)\gamma_\mu\gamma_5 q(x)$ is employed in the denominator rather than the conserved current

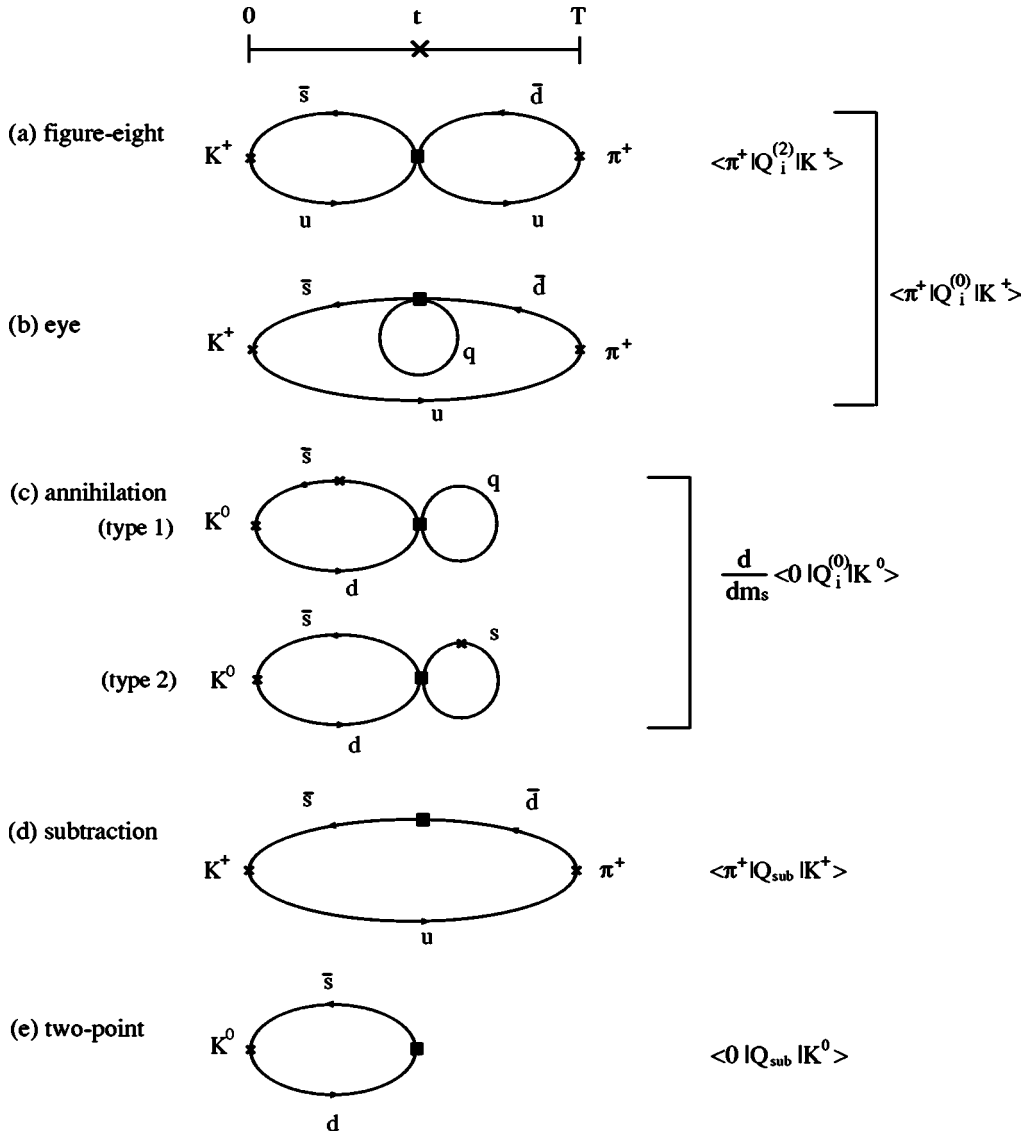

FIG. 2. Types of contractions needed for our calculation. Solid lines represent quark propagators on a background gauge field. Crosses represent points where meson sources are placed, while filled squares denote four quark operators or the subtraction operator. (a) ''figure-eight,'' (b) ''eye'' which contributes only for matrix elements of $Q_i^{(0)}$, (c) ''annihilation'' with a quark mass derivative in the external line (type 1) or in the quark loop (type 2), (d) ''subtraction,'' and (e) ''two-point.''

given in Eq. (3.13) in order to match with the local form of the four-quark operator in the numerator.

The contractions in Fig. 2(c) show the $K^0 \to 0$ (vacuum) annihilation matrix elements from which the parameters α_i in the χPT reduction formulas (2.50) are obtained. If d and s quarks are nondegenerate, these parameters are easily obtained from the ratio of propagators:

$$\frac{\langle 0|Q_i^{(0)}(t)(K^0)^\dagger(0)|0\rangle}{\langle 0|Q_{\rm sub}(t)(K^0)^\dagger(0)|0\rangle} \overset{t\to\infty}{\simeq} \frac{\langle 0|Q_i^{(0)}|K^0\rangle}{\langle 0|Q_{\rm sub}|K^0\rangle} = \alpha_i . \quad (3.23)$$

In the limit of degenerate quark masses, which applies to our numerical simulation, some care is needed. From the definition of $Q_{\rm sub}$ (2.41) and the fact that *CPS* symmetry gives $\langle 0|Q_i|K^0\rangle|_{m_s=m_d}=0$, we derive

$$\alpha_i = -\lim_{m_s\to m_d} \frac{\langle 0|Q_i^{(0)}|K^0\rangle|_{m_s>m_d}}{(m_s-m_d)\langle 0|\bar{s}\gamma_5 d|K^0\rangle} \quad (3.24)$$

$$= -\frac{\dfrac{d}{dm_s}\langle 0|Q_i^{(0)}|K^0\rangle|_{m_s=m_d}}{\langle 0|\bar{s}\gamma_5 d|K^0\rangle}. \quad (3.25)$$

The derivative acts both on the operator $Q_i^{(0)}$ and on the kaon, and hence there are two contributions as shown in Fig. 2(c). The necessary derivative of the quark propagator is obtained through

$$\frac{dG(x,y)}{dm} = -\sum_z G(x,z)G(z,y). \quad (3.26)$$

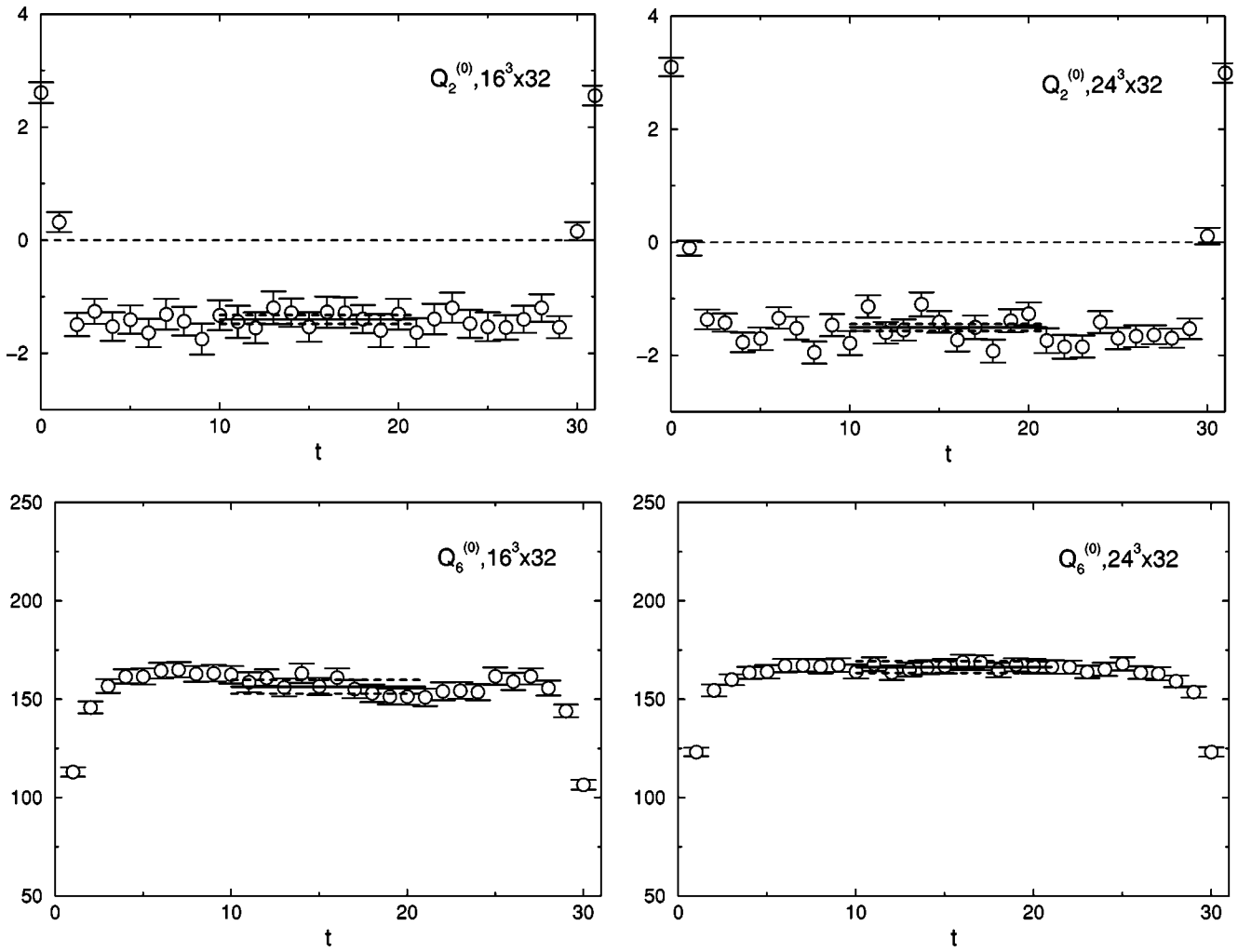

FIG. 3. Time dependence of the propagator ratio defined by Eq. (3.22) for $Q_2^{(0)}$ (upper) and $Q_6^{(0)}$ (lower) for $m_f a = 0.03$. Left and right columns are for the lattice size $16^3 \times 32$ and $24^3 \times 32$, respectively.

To calculate the quark loops that appear in the eye and annihilation contractions, we employ the random $U(1)$ noise method. We generate $\zeta^{(j)}(x) = e^{i\theta(x)} (j = 1, \ldots, N)$ from a uniform random number $\theta(x)$ in the interval $0 \leqslant \theta < 2\pi$. In the limit $N \to \infty$, we have

$$\frac{1}{N} \sum_{i=1}^{N} \zeta^{(i)*}(x) \zeta^{(i)}(y) \overset{N\to\infty}{\to} \delta(x-y). \tag{3.27}$$

Therefore, calculating quark propagators with $\zeta^{(i)}(x)$ as the source,

$$\eta^{(i)}(x) \equiv \sum_{x'} (D+m)^{-1}(x,x') \zeta^{(i)}(x'), \tag{3.28}$$

we find

$$\frac{1}{N} \sum_{i=1}^{N} \eta^{(i)}(x) \zeta^{(i)*}(x) \overset{N\to\infty}{\to} (D+m)^{-1}(x,x) \tag{3.29}$$

as the quark loop amplitude for each gauge configuration.

In our calculation, we generate two noises for *each spinor and color degree of freedom*, i.e., $2 \times$(No. color) $\times$(No. spinor) $= 24$ noises for each configuration. In Figs. 3 and 4 we show propagator ratios for the $Q_2^{(0)}$ and $Q_6^{(0)}$ operators, and those for α_2 and α_6. The horizontal lines indicate the values extracted from a constant fit over $t = 10$–21 and the one standard deviation error band. Here correlations between different time slices are not taken into account for the fit. Instead errors are estimated by the jackknife method. We observe reasonable signals, which show that 24 noises for each configuration we employ is sufficient to evaluate the quark loop amplitude. From Eq. (3.22), the χPT reduction formulas derived in Secs. II C and II D are converted to the following forms at the lowest order of χPT:

For $i = 1, \ldots, 6, 9, 10$:

$$\langle \pi^+ \pi^- | Q_i^{(0)} | K^0 \rangle = \sqrt{2} f_\pi (m_K^2 - m_\pi^2) \times \frac{\langle \pi^+ | Q_i^{(0)} - \alpha_i Q_{\rm sub} | K^+ \rangle}{\langle \pi^+ | A_4 | 0 \rangle \langle 0 | A_4 | K^+ \rangle}, \tag{3.30}$$

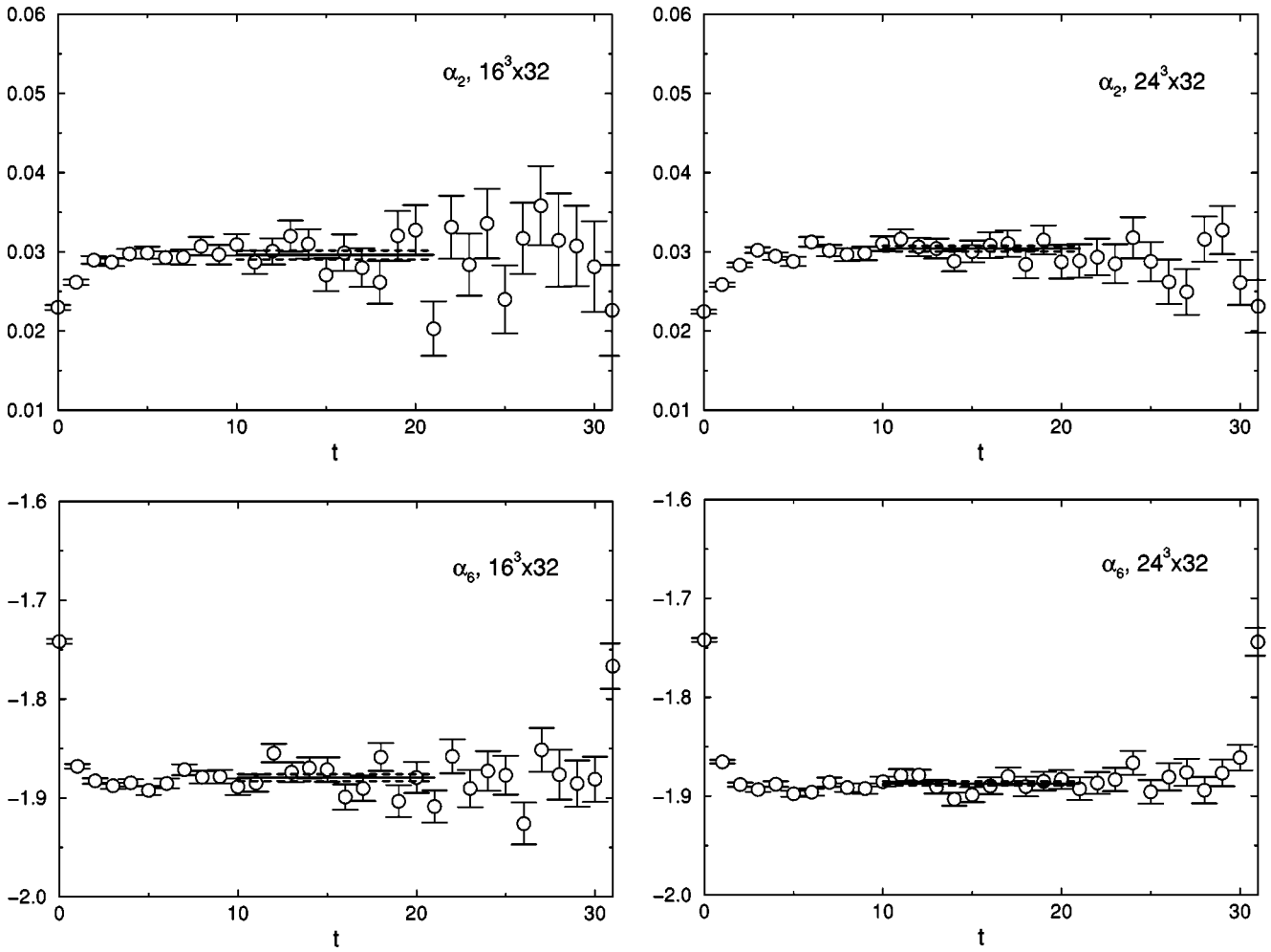

FIG. 4. Time dependence of the propagator ratio defined by Eq. (3.25) to calculate the parameter $a^2\times\alpha_2$ (upper) and $a^2\times\alpha_6$ (lower) at $m_f a=0.03$. Left and right columns are for the lattice size $16^3\times32$ and $24^3\times32$, respectively.

$$\langle\pi^+\pi^-|Q_i^{(2)}|K^0\rangle=\sqrt{2}f_\pi(m_K^2-m_\pi^2)\times\frac{\langle\pi^+|Q_i^{(2)}|K^+\rangle}{\langle\pi^+|A_4|0\rangle\langle0|A_4|K^+\rangle},\quad(3.31)$$

for $i=7,8$ $(I=0,2)$:

$$\langle\pi^+\pi^-|Q_i^{(I)}|K^0\rangle=-\sqrt{2}f_\pi m_M^2\times\frac{\langle\pi^+|Q_i^{(I)}|K^+\rangle}{\langle\pi^+|A_4|0\rangle\langle0|A_4|K^+\rangle},\quad(3.32)$$

where we set $p_K=(im_M,\vec{0})$ and $p_\pi=(-im_M,\vec{0})$ for $K^+\to\pi^+$ matrix elements on the right-hand side. We identify f_M with f, and assign to it the physical value of f_π, since f_M agrees with f_π in the chiral limit. On the other hand, the meson masses m_K^2 and m_π^2 in Eqs. (3.30) and (3.31) represent the experimental values since they arise from the physical $K\to\pi\pi$ matrix elements. All of the experimental values used in our calculation are summarized in Appendix B. We emphasize that these formulas are valid to the lowest order in χPT. If higher order corrections are small, the right-hand sides of Eqs. (3.30)–(3.32) should depend only weakly on the lattice meson mass m_M^2.

The two-pion states in the isospin basis are decomposed as

$$|(\pi\pi)_0\rangle=\sqrt{\frac{2}{3}}|\pi^+\pi^-\rangle+\sqrt{\frac{1}{3}}|\pi^0\pi^0\rangle,\quad(3.33)$$

$$|(\pi\pi)_2\rangle=\sqrt{\frac{1}{3}}|\pi^+\pi^-\rangle-\sqrt{\frac{2}{3}}|\pi^0\pi^0\rangle.\quad(3.34)$$

Therefore, matrix elements in this basis are given by $\langle\pi^+\pi^-|Q_i^{(I)}|K^0\rangle$ times constants:

$$\langle(\pi\pi)_0|Q_i|K^0\rangle=\sqrt{\frac{3}{2}}\langle\pi^+\pi^-|Q_i^{(0)}|K^0\rangle;\quad(3.35)$$

$$\langle(\pi\pi)_2|Q_i|K^0\rangle=\sqrt{3}\langle\pi^+\pi^-|Q_i^{(2)}|K^0\rangle.\quad(3.36)$$

We use a shorthand notation

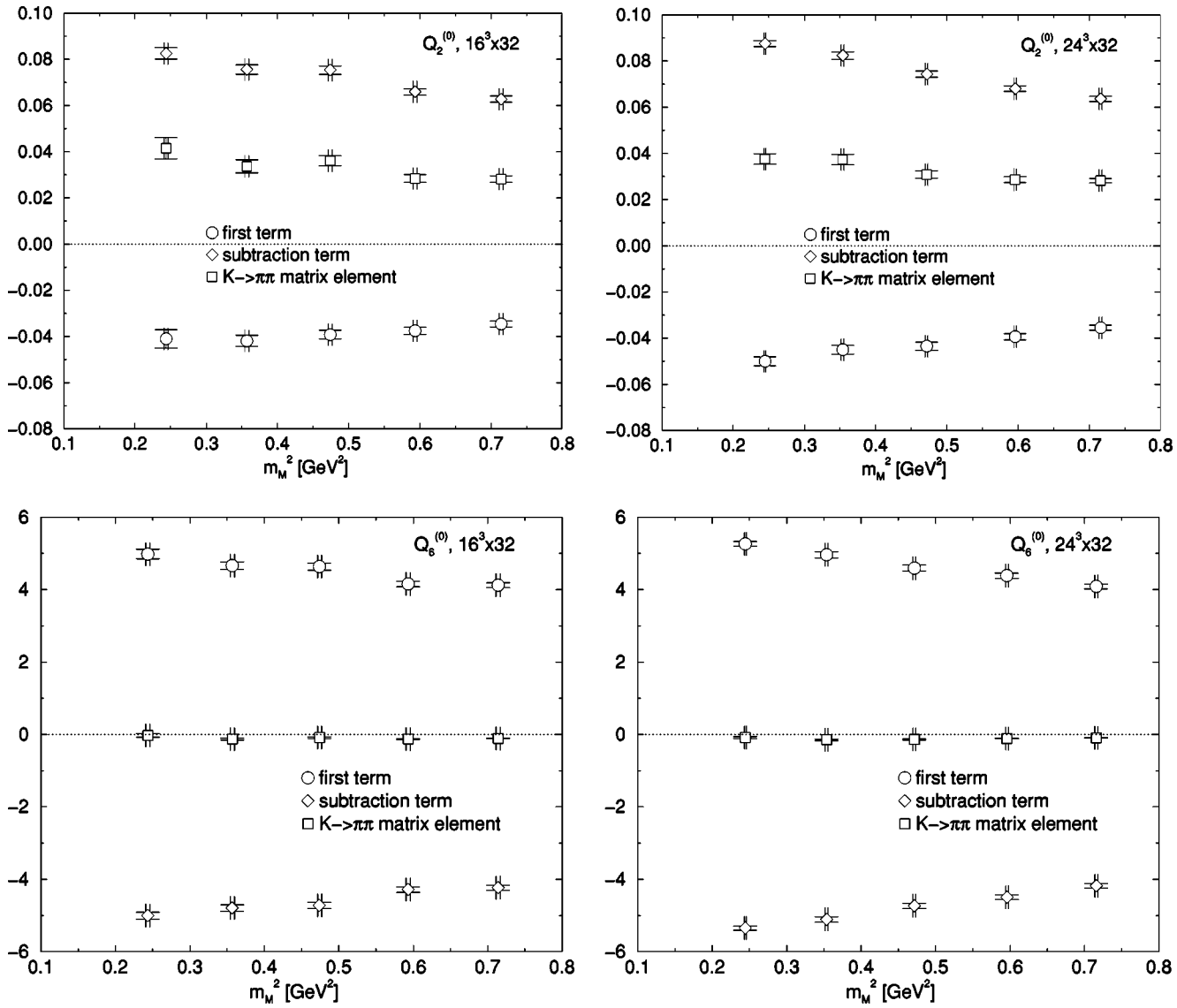

FIG. 5. Effect of subtractions illustrated for $Q_2^{(0)}$ (upper) and $Q_6^{(0)}$ (lower) as a function of m_M^2. The original matrix element $\langle \pi^+|Q_i^{(0)}|K^+\rangle$ (circles) and the subtraction term $-\alpha_i\langle \pi^+|Q_{\rm sub}|K^+\rangle$ (diamonds) are added to obtain the physical matrix element (squares). Values are multiplied with a factor $\sqrt{2}f_\pi(m_K^2-m_\pi^2)/\langle \pi^+|A_4|0\rangle\langle 0|A_4|K^+\rangle$ so that the vertical axis has dimension [GeV^3]. Left and right columns are for the lattice sizes $16^3\times 32$ and $24^3\times 32$, respectively.

$$\langle Q_i\rangle_I \equiv \langle (\pi\pi)_I|Q_i|K^0\rangle, \quad I=0,2 \tag{3.37}$$

for the matrix elements in the isospin basis hereafter.

D. Subtractions in $\Delta I=1/2$ matrix elements

According to Eq. (3.30) the contribution of the unphysical operator $Q_{\rm sub}$ has to be subtracted for calculating the $\Delta I=1/2$ matrix elements. Figure 5 shows the original matrix element $\langle \pi^+|Q_i^{(0)}|K^+\rangle$ (circles), the subtraction term $-\alpha_i\langle \pi^+|Q_{\rm sub}|K^+\rangle$ (diamonds), and their sum (squares), multiplied with a factor $\sqrt{2}f_\pi(m_K^2-m_\pi^2)/\langle \pi^+|A_4|0\rangle\langle 0|A_4|K^+\rangle$ for conversion to the $K\to\pi\pi$ matrix elements [see Eq. (3.30)]. The left and right columns correspond to the spatial sizes 16^3 and 24^3, respectively, and the upper and lower rows exhibit the data for $Q_2^{(0)}$ and $Q_6^{(0)}$ as typical examples. These matrix elements play a dominant role in the $\Delta I=1/2$ rule and ε'/ε as we see in later sections. The numerical details of subtractions for all of the relevant operators $Q_i^{(0)}$ for $i=1,2,3,5,6$ are collected in Table III.

We observe that the subtraction term represents a crucial contribution in the physical matrix element. In the case of $Q_2^{(0)}$ the subtraction term is twice larger than the original matrix element and opposite in sign. Thus the physical matrix element is similar in magnitude but flipped in sign compared to the original matrix element.

For the case of $Q_6^{(0)}$ the subtraction term almost cancels the original matrix element so that the physical matrix element is an order of magnitude reduced in size. Nonetheless, as one can see from inspection of Table III, the physical matrix elements are well determined with errors of 10–20 %.

TABLE III. Subtraction in $K\to\pi$ matrix element $\langle\pi^+|Q_i^{(0)}|K^+\rangle$ for $i=1,2,3,5,6$ multiplied with a factor $\sqrt{2}f_\pi(m_K^2-m_\pi^2)/\langle\pi^+|A_4|0\rangle\langle 0|A_4|K^+\rangle$. The values of the $K^+\to\pi^+$ matrix element (first), the subtraction term $-\alpha_i\langle\pi^+|Q_{\rm sub}|K^+\rangle$ (subtraction), and their sum (total) are given in units of GeV^3.

		$16^3\times 32$			$24^3\times 32$		
	$m_f a$	first	subtraction	total	first	subtraction	total
$Q_1^{(0)}$	0.02	−0.0135(44)	−0.0134(25)	−0.0269(56)	−0.0028(23)	−0.0164(12)	−0.0192(28)
	0.03	−0.0084(29)	−0.0133(20)	−0.0217(39)	−0.0052(24)	−0.0115(14)	−0.0167(30)
	0.04	−0.0091(21)	−0.0107(16)	−0.0198(30)	−0.0082(14)	−0.0092(10)	−0.0174(21)
	0.05	−0.0096(16)	−0.0085(13)	−0.0181(24)	−0.0056(12)	−0.0076(10)	−0.0131(18)
	0.06	−0.0071(14)	−0.0073(12)	−0.0144(20)	−0.0085(11)	−0.00752(82)	−0.0160(16)
$Q_2^{(0)}$	0.02	−0.0410(40)	0.0825(25)	0.0415(46)	−0.0500(19)	0.0875(13)	0.0375(23)
	0.03	−0.0419(24)	0.0755(21)	0.0336(29)	−0.0450(19)	0.0823(16)	0.0373(22)
	0.04	−0.0392(18)	0.0752(18)	0.0361(22)	−0.0434(18)	0.0743(14)	0.0309(16)
	0.05	−0.0375(15)	0.0659(14)	0.0284(16)	−0.0394(13)	0.0680(12)	0.0286(13)
	0.06	−0.0346(13)	0.0627(13)	0.0281(14)	−0.0354(11)	0.0636(11)	0.02821(94)
$Q_3^{(0)}$	0.02	−0.130(17)	0.1253(90)	−0.005(21)	−0.1151(81)	0.1256(46)	0.010(10)
	0.03	−0.118(10)	0.1107(81)	−0.007(14)	−0.1140(84)	0.1311(53)	0.017(11)
	0.04	−0.1137(76)	0.1179(61)	0.004(11)	−0.1198(61)	0.1206(42)	0.0008(80)
	0.05	−0.1132(65)	0.1055(50)	−0.0077(86)	−0.1052(46)	0.1146(43)	0.0094(66)
	0.06	−0.1000(50)	0.1031(47)	0.0032(75)	−0.1049(44)	0.1051(35)	0.0002(55)
$Q_5^{(0)}$	0.02	1.719(45)	−1.743(36)	−0.024(24)	1.832(24)	−1.853(185)	−0.022(11)
	0.03	1.608(37)	−1.657(32)	−0.048(15)	1.731(31)	−1.768(261)	−0.036(11)
	0.04	1.591(33)	−1.633(30)	−0.042(11)	1.593(27)	−1.635(249)	−0.0420(80)
	0.05	1.438(26)	−1.482(25)	−0.0444(82)	1.521(25)	−1.553(224)	−0.0321(67)
	0.06	1.430(26)	−1.465(23)	−0.0359(71)	1.412(23)	−1.448(205)	−0.0361(53)
$Q_6^{(0)}$	0.02	4.98(13)	−5.01(10)	−0.025(51)	5.264(67)	−5.350(54)	−0.086(22)
	0.03	4.66(10)	−4.792(91)	−0.129(26)	4.960(88)	−5.110(76)	−0.150(20)
	0.04	4.632(97)	−4.721(86)	−0.089(19)	4.595(80)	−4.732(71)	−0.137(14)
	0.05	4.155(78)	−4.287(71)	−0.132(12)	4.385(72)	−4.496(65)	−0.111(11)
	0.06	4.121(73)	−4.234(67)	−0.1129(95)	4.087(65)	−4.183(60)	−0.0957(88)

These results show that the subtraction plays a crucial role in calculations with the reduction method. Numerically this procedure is well controlled in our case.

E. Renormalization and RG-running

Throughout this paper, the renormalization of the operators and the RG-running of the matrix elements are carried out within the perturbation theory in modified minimal subtraction $\overline{\rm MS}$ scheme with naive dimensional reduction (NDR).

The physical $K\to\pi\pi$ amplitudes in the isospin basis A_I are given by

$$A_I=\frac{G_F}{\sqrt{2}}V_{\rm us}V_{\rm ud}^*\sum_{i=1}^{10}W_i(\mu)\langle Q_i\rangle_I^{\overline{\rm MS}}(\mu), \tag{3.38}$$

where we set $\delta_I=0$ since our calculation at the tree level of χPT does not incorporate the effect of the final state interaction; this effect begins from the next to leading order of χPT. The Wilson coefficient functions have a form

$$W_i(\mu)=z_i(\mu)+\tau\cdot y_i(\mu) \tag{3.39}$$

where y_i are nonvanishing only for $i=3,\ldots,10$ and $\tau\equiv-(V_{\rm ts}^*V_{\rm td})/(V_{\rm us}^*V_{\rm ud})$ is a complex constant. With our choice of scale $\mu=m_c=1.3$ GeV, the functions $z_i(m_c)$ are negligibly small for $i=3,\ldots,10$ [41].

The coefficient functions $y_i(\mu)$ and $z_i(\mu)$ at $m_c=1.3$ GeV have been calculated for several values of the QCD parameter $\Lambda_{\overline{\rm MS}}^{(4)}$ [41]. We employ $\Lambda_{\overline{\rm MS}}^{(4)}=325$ MeV for our main results, and also consider $\Lambda_{\overline{\rm MS}}^{(4)}=215$ and 435 MeV to examine the magnitude of the systematic error. The choice of the central value is motivated by recent phenomenological compilations of the strong coupling constant, e.g., Ref. [42] quotes $\Lambda_{\overline{\rm MS}}^{(4)}=296^{+46}_{-44}$ MeV corresponding to $\alpha_S^{\overline{\rm MS}}(M_{Z^0})=0.1184(31)$. We list the values of coefficient functions we use in Table IV. The experimental parameters are summarized in Appendix B.

To calculate the renormalized matrix elements in the $\overline{\rm MS}$ scheme $\langle Q_i\rangle_I^{\overline{\rm MS}}(\mu)$, we first translate the lattice values into the renormalized ones at a matching scale q^*:

TABLE IV. Wilson coefficient functions [41].

$\Lambda^{(4)}_{\overline{\rm MS}}$	z_1	z_2	y_3	y_4	y_5	y_6	y_7/α	y_8/α	y_9/α	y_{10}/α
215 MeV	−0.346	1.172	0.023	−0.048	0.007	−0.068	−0.031	0.103	−1.423	0.451
325 MeV	−0.415	1.216	0.029	−0.057	0.005	−0.089	−0.030	0.136	−1.479	0.547
435 MeV	−0.490	1.265	0.036	−0.068	0.001	−0.118	−0.029	0.179	−1.548	0.664

$$\langle Q_i\rangle_I^{\overline{\rm MS}}(q^*)=\mathcal{Z}_{ij}(q^*a)\langle Q_j\rangle_I^{\rm latt}(1/a). \tag{3.40}$$

This step is carried out using the renormalization factor calculated to one-loop order of perturbation theory [43–46]. The detailed form of the one-loop terms and explicit numerical values for $q^*=1/a$ in quenched QCD, appropriate for our case, are given in Appendix C.

The next step is to evolve the renormalized matrix elements from the scale $q^*=1/a$ to $\mu=m_c$ using the renormalization group, and combine them with the Wilson coefficient functions $W_i(\mu)$. The RG-evolution of the matrix elements $\langle Q_i\rangle_I^{\overline{\rm MS}}(\mu)$ is inverse to that of the coefficient functions $W_i(\mu)$, i.e.,

$$W_i(\mu_1)=U(\mu_1,\mu_2)_{ij}W_j(\mu_2), \tag{3.41}$$

$$\langle Q_i\rangle_I^{\overline{\rm MS}}(\mu_1)=[U^{-1}(\mu_1,\mu_2)^T]_{ij}\langle Q_j\rangle_I^{\overline{\rm MS}}(\mu_2). \tag{3.42}$$

Perturbative calculations of $U(m_c,q^*)$ at the next-to-leading order are available [41]. In Appendix C we adapt the known results to calculate the numerical values of the evolution matrix for our case in which $\mu_1=m_c=1.3$ GeV and $\mu_2=1/a=1.94$ GeV. The evolution may be made either for quenched QCD or for $N_f=3$ flavors corresponding to u, d, and s quarks, depending on the view if the matching at $\mu=1/a$ is made to the quenched theory or to the $N_f=3$ theory in the continuum space-time. This is an uncertainty inherent in quenched lattice QCD, and we choose the $N_f=3$ evolution in our calculation. We have also tested the evolution with quenched QCD, and found that the results for hadronic matrix elements do not change beyond a 10–20 % level.

For the coupling constant in our $N_f=3$ evolution, we employ the two-loop form

$$\alpha_S^{\overline{\rm MS}}(\mu)=\frac{4\pi}{\beta_0\ln\dfrac{\mu^2}{\Lambda^2_{\overline{\rm MS}}}}\left[1-\frac{\beta_1}{\beta_0^2}\frac{\ln\ln\dfrac{\mu^2}{\Lambda^2_{\overline{\rm MS}}}}{\ln\dfrac{\mu^2}{\Lambda^2_{\overline{\rm MS}}}}\right], \tag{3.43}$$

with $\Lambda^{(3)}_{\overline{\rm MS}}=372$ MeV, which corresponds to $\Lambda^{(4)}_{\overline{\rm MS}}=325$ MeV. In order to check systematic errors associated with this choice, we also make calculations for $\Lambda^{(3)}_{\overline{\rm MS}}=259$ MeV ($\Lambda^{(4)}_{\overline{\rm MS}}=215$ MeV) and $\Lambda^{(3)}_{\overline{\rm MS}}=478$ MeV ($\Lambda^{(4)}_{\overline{\rm MS}}=435$ MeV).

IV. RESULTS OF HADRONIC MATRIX ELEMENTS

A. Chiral properties of $K\to\pi$ matrix elements

As we mentioned in Sec. III B, the RG-improved gauge action provides the advantage that the measure of residual chiral symmetry breaking m_{5q} due to finite N_5 is small at $a^{-1}\simeq 2$ GeV. It is nonetheless desirable to check the size of the chiral symmetry breaking effect directly for the $K\to\pi$ matrix elements.

Explicit chiral symmetry breaking, if present, causes mixing of the $I=0$ four-quark operators $Q_i^{(0)}$ with the lower dimensional operator $\bar{s}d$ without quark mass suppression, so that $K\to\pi$ matrix elements at $m_d=m_s=m_f$ behave as

$$\langle\pi^+|Q_i^{(0)}-\alpha_iQ_{\rm sub}|K^+\rangle=\frac{2m_M^2}{f^2}(a_i-c_i^{(0)})+\left(\frac{\beta_i}{a^3}+\frac{\gamma_i}{a^2}m_f\right)\times\langle\pi^+|\bar{s}d|K^+\rangle+\mathcal{O}(m_M^4) \tag{4.1}$$

for $(8_L,1_R)$ operators, and

$$\langle\pi^+|Q_i^{(0)}|K^+\rangle=\frac{4}{f^2}d_i^{(0)}+\frac{\delta_i}{a^3}\langle\pi^+|\bar{s}d|K^+\rangle+\mathcal{O}(m_M^2) \tag{4.2}$$

for $(8_L,8_R)$ operators. Here β_i, γ_i, and δ_i are dimensionless quantities which represent magnitudes of residual chiral symmetry breaking, and hence are proportional to e^{-cN_5} with some constant c. The matrix element $\langle\pi^+|\bar{s}d|K^+\rangle$ stays nonzero in the chiral limit. Motivated by Eqs. (2.41) and (3.14), one may consider modifications of the subtraction operator such as

$$Q_{\rm sub}\to(m_s+m_d+2m_{5q})\bar{s}d-(m_s-m_d)\bar{s}\gamma_5 d. \tag{4.3}$$

Such modifications, however, will not ensure the complete removal of residual chiral symmetry breaking from the matrix elements.

The $I=2$ operators $Q_{1,2}^{(2)}$ do not mix with the $\bar{s}d$ operator. Their matrix elements can have constant terms in the chiral limit, however, due to mixings with dimension 6 operators such as $Q_{7,8}^{(2)}$ in the presence of chiral symmetry breaking. Hence we also consider the chiral behavior of these matrix elements.

Of the ten operators Q_i, we recall that $Q_{4,9,10}$ are dependent operators as shown in Eqs. (2.11)–(2.13). Furthermore, there is an identity $Q_1^{(2)}=Q_2^{(2)}$ which follows from Eqs. (2.22), (2.23), and the $I=2$ component is absent in the $Q_{3,5,6}$ operators. Thus we only need to examine the matrix elements of $Q_{1,2,3,5,6}^{(0)}$ and $Q_1^{(2)}$.

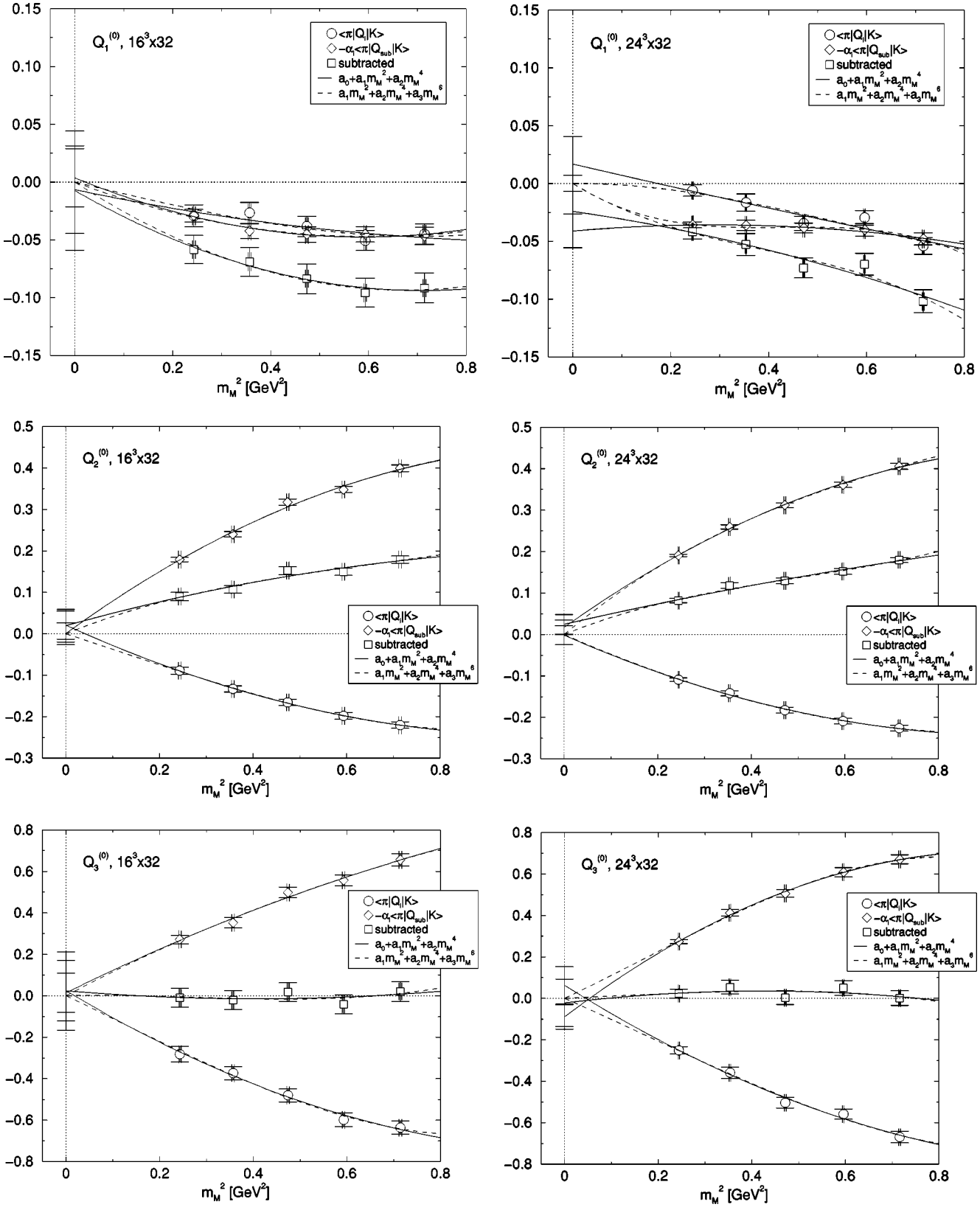

FIG. 6. Ratio of matrix elements $\langle \pi^+|X_i^{(I)}|K^+\rangle/\langle \pi^+|A_4|0\rangle\langle 0|A_4|K^+\rangle \times m_M^2 a^2$ as a function of $m_M^2[\mathrm{GeV}^2]$ for $i=1,2,3,5,6$ $(I=0)$ and $i=1$ $(I=2)$ from top to bottom. Left and right columns are for the lattice sizes $16^3\times 32$ and $24^3\times 32$, respectively. Solid lines represent the chiral extrapolation to $m_M^2 \to 0$ with a quadratic function of m_M^2, while dashed lines are with a cubic function as described in the text.

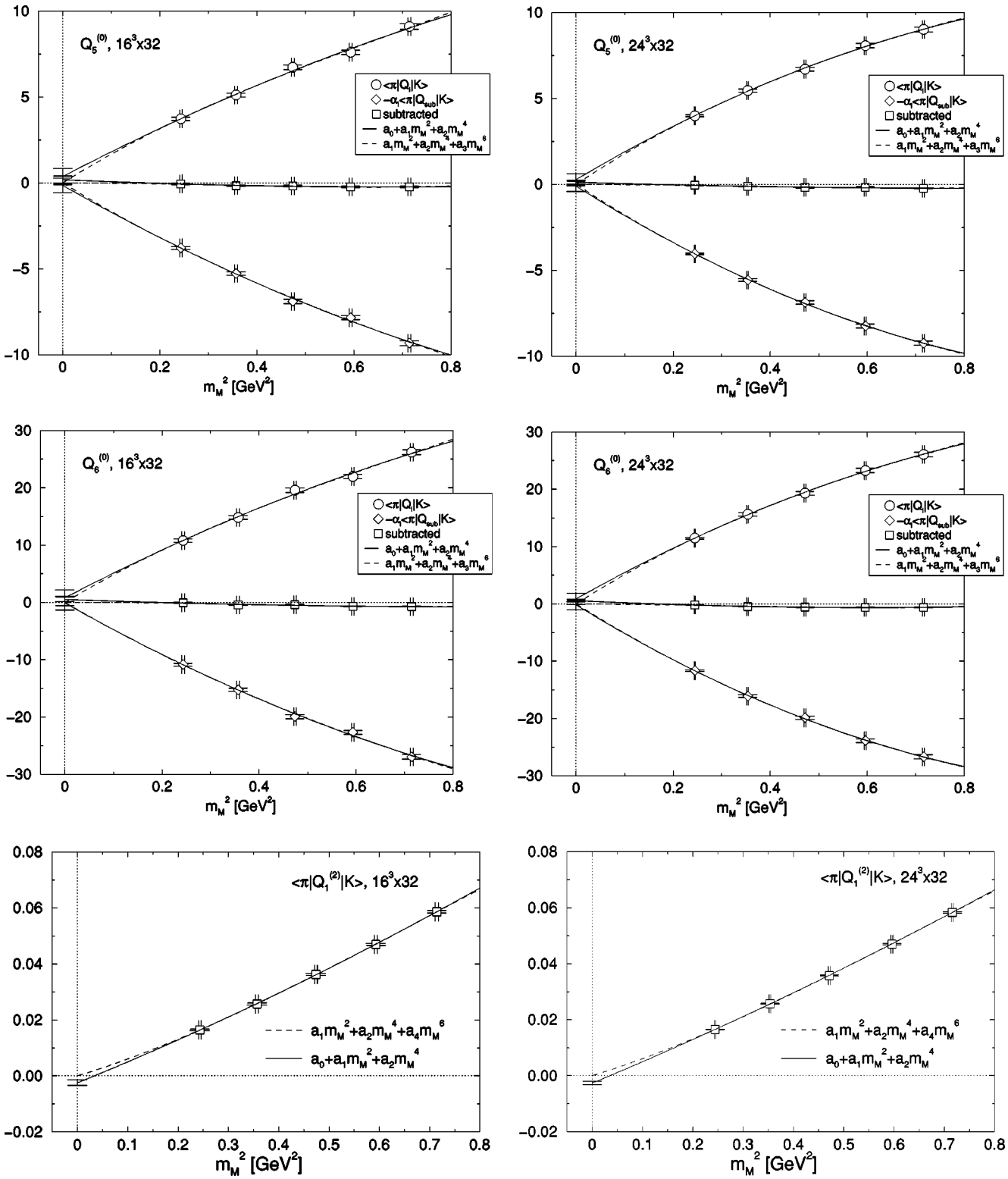

FIG. 6. (*Continued*).

Figure 6 shows these matrix elements as functions of m_M^2 (GeV^2) for the two spatial volumes $V=16^3$ (left column) and $V=24^3$ (right column), adopting the normalization defined by

$$\frac{\langle \pi^+|X_i^{(I)}|K^+\rangle}{\langle \pi^+|A_4|0\rangle\langle 0|A_4|K^+\rangle}\times m_M^2 a^2=\frac{a^2}{2f_M^2}\langle \pi^+|X_i^{(I)}|K^+\rangle. \tag{4.4}$$

TABLE V. Fit parameters for the chiral extrapolation of the $K\to\pi$ matrix elements defined by Eq. (4.4) which should vanish in the chiral limit. The parameters (a_0,a_1,a_2) are determined by the fit function $a_0+a_1m_M^2+a_2(m_M^2)^2$.

	$16^3\times32$				$24^3\times32$			
	a_0	$a_1[\mathrm{GeV}^{-2}]$	$a_2[\mathrm{GeV}^{-4}]$	χ^2/dof	a_0	$a_1[\mathrm{GeV}^{-2}]$	$a_2[\mathrm{GeV}^{-4}]$	χ^2/dof
$Q_1^{(0)}$	−0.007(38)	−0.09(17)	0.04(17)	0.63	0.017(24)	−0.10(11)	0.01(12)	1.88
$-\alpha_1Q_{\mathrm{sub}}$	0.004(25)	−0.17(12)	0.15(13)	0.19	−0.041(15)	0.037(74)	−0.064(81)	0.06
$Q_1^{(0)}-\alpha_1Q_{\mathrm{sub}}$	−0.007(51)	−0.24(24)	0.17(24)	0.12	−0.024(31)	−0.06(15)	−0.06(16)	1.16
$Q_2^{(0)}$	0.021(34)	−0.51(15)	0.25(15)	0.07	−0.002(23)	−0.50(11)	0.26(12)	0.35
$-\alpha_2Q_{\mathrm{sub}}$	0.000(26)	0.82(13)	−0.37(13)	2.43	0.017(18)	0.802(92)	−0.37(10)	0.71
$Q_2^{(0)}-\alpha_2Q_{\mathrm{sub}}$	0.019(40)	0.31(18)	−0.13(18)	2.09	0.024(25)	0.26(11)	−0.06(12)	1.40
$Q_3^{(0)}$	0.02(15)	−1.36(64)	0.59(65)	0.42	0.063(90)	−1.43(44)	0.58(47)	0.92
$-\alpha_3Q_{\mathrm{sub}}$	0.0014(95)	1.12(46)	−0.31(49)	0.89	−0.089(59)	1.71(30)	−0.92(33)	0.34
$Q_3^{(0)}-\alpha_3Q_{\mathrm{sub}}$	0.02(19)	−0.19(86)	0.23(89)	0.58	−0.02(11)	0.27(56)	−0.32(60)	0.87
$Q_5^{(0)}$	0.37(48)	14.7(2.3)	−3.7(2.5)	2.56	0.27(34)	16.8(1.7)	−6.4(1.9)	0.48
$-\alpha_5Q_{\mathrm{sub}}$	−0.15(42)	−16.1(2.0)	4.7(2.2)	2.56	−0.11(29)	−17.8(1.5)	7.0(1.7)	0.40
$Q_5^{(0)}-\alpha_5Q_{\mathrm{sub}}$	0.020(20)	−1.27(90)	0.95(92)	0.17	0.13(12)	−0.85(57)	0.51(61)	0.48
$Q_6^{(0)}$	0.8(1.4)	44.1(6.6)	−12.4(7.1)	2.96	0.86(97)	47.6(5.0)	−17.2(5.6)	0.31
$-\alpha_6Q_{\mathrm{sub}}$	−0.1(1.2)	−47.8(5.8)	14.8(6.3)	2.61	−0.19(85)	−52.1(4.5)	21.0(5.0)	0.42
$Q_6^{(0)}-\alpha_6Q_{\mathrm{sub}}$	0.053(38)	−3.0(1.6)	1.7(1.6)	2.27	0.59(22)	−4.0(1.0)	3.3(1.1)	0.62
$Q_1^{(2)}$	−0.0023(13)	0.0727(64)	0.0178(68)	0.19	−0.00264(65)	0.0751(33)	0.0140(37)	0.28
	b_0	$b_1[\mathrm{GeV}^{-2}]$	$b_2\ [\mathrm{GeV}^{-4}]$	χ^2/dof	b_0	$b_1\ [\mathrm{GeV}^{-2}]$	$b_2\ [\mathrm{GeV}^{-4}]$	χ^2/dof
$\overline{sd}$	−170(11)	116(46)	−64(45)	2.21	−186.2(4.0)	151(19)	−82(19)	3.72

For the $I=0$ channel, three data sets are plotted, corresponding to the original matrix element $X_i^{(I)}=Q_i^{(I)}$ (circles), the subtraction term $-\alpha_iQ_{\mathrm{sub}}$ (diamonds), and the subtracted matrix element $Q_i^{(I)}-\alpha_iQ_{\mathrm{sub}}$ (squares). For the $I=2$ channel, subtractions are absent and hence $X_i^{(I)}=Q_i^{(I)}$.

The denominator of Eq. (4.4) behaves as

$$\langle\pi^+|A_4|0\rangle\langle0|A_4|K^+\rangle=2f_M^2m_M^2, \tag{4.5}$$

irrespective of whether chiral symmetry holds exactly or not. The advantage of our normalization is that the coefficient of the m_M^2 term of the ratio is directly related to the $K^0\to\pi^+\pi^-$ matrix elements. An alternative normalization is provided by the ratio

$$\frac{\langle\pi^+|X_i^{(I)}|K^+\rangle}{\langle\pi^+|P|0\rangle\langle0|P|K^+\rangle}, \tag{4.6}$$

where $P=\overline{q}\gamma_5q$ is the pseudoscalar density. This method avoids the use of measured values of pion mass, but it loses the straightforward relation to the physical matrix elements. We use the normalization (4.4) in our analyses. We have checked, however, that the conclusion remains unchanged even if Eq. (4.6) is employed instead.

For chiral extrapolation we consider an expansion of the form

$$\frac{a^2}{2f_M^2}\langle\pi^+|X_i^{(I)}|K^+\rangle=a_0+a_1m_M^2+a_2(m_M^2)^2+a_3(m_M^2)^2\times\ln m_M^2+a_4(m_M^2)^3+\cdots. \tag{4.7}$$

Chiral extrapolations using the first three terms are indicated by the solid line in each panel of Fig. 6. The fit parameters are summarized in Table V. The results for the intercept a_0 in the chiral limit are consistent with zero within the fitting errors except for the $I=2$ operator $Q_1^{(2)}$ for the volumes $V=16^3(1.8\sigma)$ and $24^3(4\sigma)$, the $I=0$ subtracted operator $Q_6^{(0)}-\alpha_6Q_{\mathrm{sub}}$ for $V=16^3(1.4\sigma)$ and $24^3(2.7\sigma)$, and the subtraction term for the $i=1$ operator $-\alpha_1Q_{\mathrm{sub}}$ for $V=24^3(2.8\sigma)$. Since no systematic tendency that the intercepts become larger for smaller volume is observed, it is unlikely that the nonzero intercepts of these matrix elements are caused by the finite spatial size effect. Indeed even an opposite tendency that the intercept becomes larger for larger spatial volumes is observed.

The absence of a systematic trend in our data suggests the possibility that nonzero intercepts observed for some of the matrix elements are artifacts of the long extrapolation in m_M^2. To test this point, we attempt a fit with a cubic polynomial of form $a_1m_M^2+a_2(m_M^2)^2+a_4(m_M^2)^3$ and a form with chiral logarithm given by $a_1m_M^2+a_2(m_M^2)^2+a_3(m_M^2)^2\ln m_M^2$, both having a built-in chiral behavior of

TABLE VI. Same as Table V for the fit function $a_1 m_M^2 + a_2 (m_M^2)^2 + a_4 (m_M^2)^3$.

	$16^3 \times 32$				$24^3 \times 32$			
	$a_1[\mathrm{GeV}^{-2}]$	$a_2[\mathrm{GeV}^{-4}]$	$a_4[\mathrm{GeV}^{-6}]$	χ^2/dof	$a_1[\mathrm{GeV}^{-2}]$	$a_2[\mathrm{GeV}^{-4}]$	$a_4[\mathrm{GeV}^{-6}]$	χ^2/dof
$Q_1^{(0)}$	−0.10(11)	0.01(44)	0.06(41)	0.64	0.004(67)	−0.18(28)	0.10(27)	2.07
$-\alpha_1 Q_{\mathrm{sub}}$	−0.159(72)	0.14(30)	−0.01(29)	0.20	−0.271(40)	0.64(18)	−0.49(18)	0.12
$Q_1^{(0)} - \alpha_1 Q_{\mathrm{sub}}$	−0.28(15)	0.21(60)	0.00(57)	0.13	−0.257(87)	0.42(37)	−0.36(36)	0.98
$Q_2^{(0)}$	−0.37(10)	−0.06(39)	0.21(37)	0.10	−0.499(63)	0.23(27)	0.02(28)	0.35
$-\alpha_2 Q_{\mathrm{sub}}$	0.826(75)	−0.39(31)	0.02(30)	2.43	0.942(47)	−0.72(21)	0.26(22)	0.43
$Q_2^{(0)} - \alpha_2 Q_{\mathrm{sub}}$	0.46(12)	−0.46(45)	0.23(42)	2.07	0.461(67)	−0.56(28)	0.37(27)	0.98
$Q_3^{(0)}$	−1.09(43)	−0.2(1.7)	0.6(1.6)	0.35	−1.00(25)	−0.3(1.0)	0.6(1.0)	1.02
$-\alpha_3 Q_{\mathrm{sub}}$	1.20(27)	−0.4(1.1)	0.1(1.1)	0.90	1.07(16)	0.51(71)	−0.97(71)	0.57
$Q_3^{(0)} - \alpha_3 Q_{\mathrm{sub}}$	0.05(55)	−0.4(2.2)	0.5(2.1)	0.55	0.10(32)	0.1(1.3)	−0.3(1.3)	0.87
$Q_5^{(0)}$	17.7(1.4)	−11.1(5.7)	5.6(5.6)	2.36	18.82(88)	−11.0(4.0)	3.3(4.1)	0.50
$-\alpha_5 Q_{\mathrm{sub}}$	−17.5(1.2)	8.5(5.0)	−3.0(5.0)	2.44	−18.68(76)	9.2(3.5)	−1.6(3.7)	0.38
$Q_5^{(0)} - \alpha_5 Q_{\mathrm{sub}}$	0.08(59)	−1.9(2.3)	1.9(2.2)	0.23	0.03(34)	−1.3(1.4)	1.2(1.4)	0.68
$Q_6^{(0)}$	50.9(3.9)	−29(16)	13(16)	2.80	54.0(2.5)	−32(12)	10(12)	0.34
$-\alpha_6 Q_{\mathrm{sub}}$	−49.6(3.4)	21(14)	−6(14)	2.54	−53.6(2.2)	25(10)	−2.8(1.1)	0.41
$Q_6^{(0)} - \alpha_6 Q_{\mathrm{sub}}$	0.6(1.1)	−5.9(4.1)	5.0(3.8)	2.36	0.04(63)	−5.3(2.6)	5.7(2.5)	1.54
$Q_1^{(2)}$	0.0555(38)	0.057(16)	−0.027(15)	0.18	0.0557(17)	0.0573(77)	−0.0299(79)	1.50

vanishing at $m_M^2 = 0$. We show the former fit curves by dashed lines in Fig. 6 and the fitted parameters in Table VI. Numerical results of the chiral logarithm fit are given in Table VII. The fit curves are similar to those of the cubic fit. Both functions provide good fit of data with reasonable χ^2/dof.

Let us try to analyze the chiral behavior of $I=0$ matrix elements in terms of mixing with the $\bar{s}d$ operator as given in Eq. (4.1). The existence of the constant β_i can be detected from the chiral limit of the matrix elements. On the other hand, separating the contribution of γ_i and δ_i from the physical ones would require results at different N_5. We leave such

TABLE VII. Same as Table V for the fit function $a_1 m_M^2 + a_2 (m_M^2)^2 + a_3 (m_M^2)^2 \ln m_M^2$ including a chiral logarithm term.

	$16^3 \times 32$				$24^3 \times 32$			
	$a_1[\mathrm{GeV}^{-2}]$	$a_2[\mathrm{GeV}^{-4}]$	$a_3[\mathrm{GeV}^{-4}]$	χ^2/dof	$a_1[\mathrm{GeV}^{-2}]$	$a_2[\mathrm{GeV}^{-4}]$	$a_3[\mathrm{GeV}^{-4}]$	χ^2/dof
$Q_1^{(0)}$	−0.11(20)	0.07(14)	0.02(39)	0.65	0.04(12)	−0.110(84)	0.13(25)	2.01
$-\alpha_1 Q_{\mathrm{sub}}$	−0.15(13)	0.128(90)	0.01(27)	0.20	−0.369(74)	0.268(49)	−0.46(16)	0.06
$Q_1^{(0)} - \alpha_1 Q_{\mathrm{sub}}$	−0.29(27)	0.21(19)	−0.03(54)	0.13	−0.32(16)	0.15(11)	−0.31(34)	1.05
$Q_2^{(0)}$	−0.32(18)	0.09(13)	0.20(35)	0.09	−0.50(12)	0.259(77)	0.01(25)	0.35
$-\alpha_2 Q_{\mathrm{sub}}$	0.83(13)	−0.376(93)	0.01(28)	2.43	0.987(88)	−0.515(56)	0.23(20)	0.52
$Q_2^{(0)} - \alpha_2 Q_{\mathrm{sub}}$	0.50(21)	−0.29(15)	0.21(41)	2.08	0.53(12)	−0.276(85)	0.33(25)	1.11
$Q_3^{(0)}$	−1.01(76)	0.32(56)	0.5(1.5)	0.38	−0.85(45)	0.10(31)	0.59(97)	0.98
$-\alpha_3 Q_{\mathrm{sub}}$	1.22(49)	−0.40(34)	0.1(1.0)	0.89	0.86(29)	−0.21(19)	−0.93(66)	0.49
$Q_3^{(0)} - \alpha_3 Q_{\mathrm{sub}}$	0.12(98)	−0.01(71)	0.4(2.0)	0.56	0.05(58)	−0.14(39)	−0.2(1.2)	0.87
$Q_5^{(0)}$	18.7(2.4)	−6.8(1.7)	4.8(5.2)	2.44	19.5(1.7)	−8.6(1.0)	3.1(3.8)	0.48
$-\alpha_5 Q_{\mathrm{sub}}$	−17.9(2.1)	6.1(1.4)	−2.4(4.6)	2.49	−19.0(1.4)	7.99(88)	−1.4(3.4)	0.38
$Q_5^{(0)} - \alpha_5 Q_{\mathrm{sub}}$	0.5(1.1)	−0.54(77)	1.9(2.1)	0.21	0.32(61)	−0.46(42)	1.2(1.3)	0.61
$Q_6^{(0)}$	52.9(7.1)	−19.5(4.9)	11(15)	2.87	56.1(4.8)	−24.2(3.0)	10(11)	0.32
$-\alpha_6 Q_{\mathrm{sub}}$	−50.1(6.1)	16.5(4.1)	−4(13)	2.58	−54.1(4.2)	22.6(2.5)	−2.5(9.7)	0.42
$Q_6^{(0)} - \alpha_6 Q_{\mathrm{sub}}$	1.8(1.9)	−2.2(1.5)	5.0(3.7)	2.35	1.4(1.1)	−1.16(80)	5.7(2.3)	1.21
$Q_1^{(2)}$	0.0498(68)	0.0364(47)	−0.026(15)	0.15	0.0494(32)	0.0351(20)	−0.0285(73)	0.99

TABLE VIII. $1/2f_M^2 a\langle\pi^+|\bar{s}d|K^+\rangle$ as a function of $m_f a$.

$m_f a$	0.02	0.03	0.04	0.05	0.06
$16^3\times 32$	−145.0(3.1)	−135.1(2.5)	−132.6(2.3)	−120.9(1.9)	−120.2(1.8)
$24^3\times 32$	−154.7(1.6)	−142.1(2.1)	−131.9(1.9)	−127.4(1.7)	−119.3(1.6)

an investigation for future studies, and assume that the latter contributions are negligible. We also ignore mixings with the dimension five operators $\bar{s}\sigma_{\mu\nu}F_{\mu\nu}d$ since their contributions are subleading in $1/a$.

We estimate β_i from the values of a_0 obtained in the chiral fit of the matrix elements for the subtracted operator $Q_i^{(0)}-\alpha_i Q_{\rm sub}$ given in Table V. For this purpose, we repeat the calculation of Eq. (4.4) for $X_i^{(I)}=\bar{s}d$, and extract

$$\frac{\langle\pi^+|\bar{s}d|K^+\rangle a}{\langle\pi^+|A_4|0\rangle\langle 0|A_4|K^+\rangle a^4}\times m_M^2 a^2=\frac{1}{2f_M^2 a}\langle\pi^+|\bar{s}d|K^+\rangle, \tag{4.8}$$

where powers of a are supplied to absorb dimensions of matrix elements. We then fit the results to a quadratic polynomial $b_0+b_1 m_M^2+b_2(m_M^2)^2$. The numerical values of Eq. (4.8) are given in Table VIII, and the results for b_i are given in Table V. Normalizing with $m_{5q}=0.283$ MeV to take into account the e^{-cN_5} dependence expected for β_i, one has

$$\frac{\beta_i}{m_{5q}a}=\frac{a_0}{b_0}\frac{1}{m_{5q}a}. \tag{4.9}$$

In the case of $V=24^3$, the results are $\beta_i/(m_{5q}a)=0.9(1.1)$ for $i=1$, $-0.91(87)$ for $i=2$, $0.8(4.2)$ for $i=3$, $-4.7(4.4)$ for $i=5$, and $-21.6(8.1)$ for $i=6$. Except for the $i=6$ operator for which the coefficient is exceptionally large, we find values consistent with zero within the errors.

The analyses described here do not show strong evidence for the effect of residual chiral symmetry breaking in the $K\to\pi$ matrix elements. Although more data at smaller quark masses will be needed for the definite conclusion, we conclude here that our results for the matrix elements are consistent with the expected chiral behavior within the statistical precision of our data. Therefore, for the chiral extrapolation in the rest of this paper, we employ the cubic polynomial without a constant term for the central value and use the form with a chiral logarithm to estimate the systematic uncertainty. Since nonzero intercepts beyond statistical errors cannot be excluded for some of the matrix elements, we examine possible effects of the residual chiral symmetry breaking to the physical matrix elements in Sec. V.

Let us also make a comment on the comparison of lattice data with predictions of quenched chiral perturbation theory. For the $I=0$ channel, data for more values of m_f are required for such a comparison because of the presence of a number of unknown parameters as well as a new term of form $b_1 m_M^2\ln m_M^2$ in the predicted matrix elements [47]. On the other hand, quenched chiral logarithm terms are absent for the $I=2$ matrix elements governed by the $(27_L,1_R)$ operator, and the ratio a_3/a_1 for $Q_1^{(2)}$ is predicted to be $a_3/a_1=-6/(16\pi^2 f_\pi^2)=-2.180$ GeV^{-2}. We observe in Table VII that the fitted value agrees in sign but is 3 to 4 times smaller in magnitude than the prediction, e.g., $a_3/a_1=-0.58(10)$ GeV^{-2} on a $24^3\times 32$ lattice.

Quenched chiral perturbation theory makes the same prediction for the coefficient of the logarithm term of the chiral expansion of B_K as it is governed by the same operator in χPT. For this case, similar discrepancies of lattice results from the prediction are found for the case of the staggered fermion action [29] as well as for the domain wall fermion action [28]. A possible explanation for these large discrepancies is that higher order corrections in (quenched) χPT are non-negligible at quark masses employed in the current simulation. Indeed we have confirmed that data for $Q_1^{(2)}$ cannot be fitted by the form $a_1 m_M^2+a_2(m_M^2)^2+a_3(m_M^2)^2\ln m_M^2+a_4(m_M^2)^3$ with $a_3/a_1=-2.180$ GeV^{-2} fixed. The complete form in χPT to this order,

$$a_1 m_M^2+a_2(m_M^2)^2+a_3(m_M^2)^2\ln m_M^2+a_4(m_M^2)^3 + a_5(m_M^2)^3\ln m_M^2+a_6(m_M^2)^3(\ln m_M^2)^2,$$

unfortunately, cannot be employed for our data calculated only at five values of quark masses. Understanding the small value of a_3/a_1 for $Q_1^{(2)}$ requires further studies.

B. Physical values of hadronic matrix elements

We tabulate the values of all the $K\to\pi\pi$ matrix elements in Tables IX (for $16^3\times 32$) and X (for $24^3\times 32$). The upper half of each table lists the bare lattice values, $\langle Q_i\rangle_I^{\rm latt}$, and the lower half the physical values, $\langle Q_i\rangle_I^{\overline{\rm MS}}$, obtained through matching at the scale $q^*=1/a$ followed by an RG-evolution to $\mu=m_c$. Note that $\langle Q_{3-6}\rangle_2^{\overline{\rm MS}}$ become nonzero due to the RG-evolution which breaks the isospin symmetry in the presence of the QED interaction. The two sets of numbers do not differ beyond a 10–20 % level except for $\langle Q_{5,6,7,8}\rangle_0$, for which the difference amounts to 30–40 %. The latter situation arises from a larger magnitude of mixing of order 5–10 % among the $Q_{5,6,7,8}^{(0)}$ operators compared to the other operators which are typically less than 5%. In the following, the superscript $\overline{\rm MS}$ will be omitted unless confusion may arise.

In Table XI we illustrate the magnitude of uncertainty due to the choice of q^* by comparing the values of physical hadronic matrix elements $\langle Q_i\rangle_I(m_c)$ for the choices $q^*=1/a$ and $q^*=\pi/a$ at $m_f=0.02$ on a 24^3 spatial volume. One finds that the difference is at most 20–30 %.

In Fig. 7 we plot the physical matrix elements for the $\Delta I=1/2$ amplitudes $\langle Q_i\rangle_0$ ($i=1,\ldots,6,9,10$) as a function of m_M^2. These eight matrix elements involve the subtraction

TABLE IX. Hadronic matrix elements $\langle Q_i \rangle_0$ and $\langle Q_i \rangle_2$ ($i=1,\ldots,10$) in units of GeV^3 at each $m_f a$ on a $16^3 \times 32$ lattice. The upper half of the table lists the bare values. The lower half are those renormalized in the $\overline{\text{MS}}$ scheme at $\mu = 1/a$ and run to $\mu = 1.3$ GeV for $N_f = 3$ using $\Lambda^{(3)}_{\overline{\text{MS}}} = 372$ MeV, which corresponds to $\Lambda^{(4)}_{\overline{\text{MS}}} = 325$ MeV.

	$m_f a$	0.02	0.03	0.04	0.05	0.06
bare	$\langle Q_1 \rangle_0$	−0.0329(69)	−0.0266(48)	−0.0242(37)	−0.0222(29)	−0.0176(25)
[GeV^3]	$\langle Q_2 \rangle_0$	0.0508(57)	0.0412(35)	0.0442(27)	0.0347(20)	0.0345(17)
	$\langle Q_3 \rangle_0$	−0.006(26)	−0.008(18)	0.005(13)	−0.009(10)	0.0039(91)
	$\langle Q_4 \rangle_0$	0.078(24)	0.059(16)	0.074(12)	0.0475(93)	0.0560(82)
	$\langle Q_5 \rangle_0$	−0.030(29)	−0.059(18)	−0.051(13)	−0.054(10)	−0.0439(88)
	$\langle Q_6 \rangle_0$	−0.031(62)	−0.157(31)	−0.109(23)	−0.161(15)	−0.138(12)
	$\langle Q_7 \rangle_0$	1.635(30)	2.043(33)	2.574(42)	2.835(43)	3.328(49)
	$\langle Q_8 \rangle_0$	5.012(91)	6.25(10)	7.90(13)	8.66(13)	10.18(15)
	$\langle Q_9 \rangle_0$	−0.0464(58)	−0.0357(35)	−0.0389(28)	−0.0285(20)	−0.0284(18)
	$\langle Q_{10} \rangle_0$	0.0372(69)	0.0321(48)	0.0294(38)	0.0284(30)	0.0237(25)
	$\langle Q_1 \rangle_2$	0.01314(15)	0.01402(12)	0.01487(11)	0.015399(98)	0.015957(90)
	$\langle Q_2 \rangle_2$	0.01314(15)	0.01402(12)	0.01487(11)	0.015399(98)	0.015957(90)
	$\langle Q_7 \rangle_2$	0.4110(42)	0.4292(34)	0.4656(28)	0.4863(27)	0.5264(24)
	$\langle Q_8 \rangle_2$	1.238(13)	1.261(11)	1.3357(87)	1.3639(77)	1.4451(70)
	$\langle Q_9 \rangle_2$	0.01971(23)	0.02103(18)	0.02231(16)	0.02310(15)	0.02393(13)
	$\langle Q_{10} \rangle_2$	0.01971(23)	0.02103(18)	0.02231(16)	0.02310(15)	0.02393(13)
	$m_f a$	0.02	0.03	0.04	0.05	0.06
renormalized	$\langle Q_1 \rangle_0$	−0.0291(68)	−0.0234(47)	−0.0206(37)	−0.0191(29)	−0.0144(25)
at 1.3 GeV	$\langle Q_2 \rangle_0$	0.0510(69)	0.0360(43)	0.0415(33)	0.0291(24)	0.0301(20)
[GeV^3]	$\langle Q_3 \rangle_0$	0.004(28)	−0.012(20)	0.007(14)	−0.015(11)	0.0002(99)
	$\langle Q_4 \rangle_0$	0.082(27)	0.049(18)	0.069(13)	0.035(10)	0.0460(92)
	$\langle Q_5 \rangle_0$	−0.026(26)	−0.032(16)	−0.033(12)	−0.0253(94)	−0.0187(82)
	$\langle Q_6 \rangle_0$	−0.012(48)	−0.111(24)	−0.071(18)	−0.115(12)	−0.0960(90)
	$\langle Q_7 \rangle_0$	0.797(17)	1.021(18)	1.269(21)	1.417(21)	1.640(23)
	$\langle Q_8 \rangle_0$	3.428(69)	4.374(73)	5.469(86)	6.046(87)	7.024(94)
	$\langle Q_9 \rangle_0$	−0.0453(70)	−0.0287(43)	−0.0341(34)	−0.0205(24)	−0.0212(21)
	$\langle Q_{10} \rangle_0$	0.0347(68)	0.0306(48)	0.0278(37)	0.0275(29)	0.0231(25)
	$\langle Q_1 \rangle_2$	0.01345(16)	0.01436(13)	0.01524(11)	0.01578(10)	0.016361(91)
	$\langle Q_2 \rangle_2$	0.01328(16)	0.01417(12)	0.01504(11)	0.015571(99)	0.016137(91)
	$\langle Q_3 \rangle_2$	−0.00002740(31)	−0.00003058(27)	−0.00003395(25)	−0.00003677(24)	−0.00004007(23)
	$\langle Q_4 \rangle_2$	−0.0002198(36)	−0.0002349(30)	−0.0002521(25)	−0.0002652(21)	−0.0002830(20)
	$\langle Q_5 \rangle_2$	0.0002056(37)	0.0002196(31)	0.0002357(25)	0.0002483(22)	0.0002656(20)
	$\langle Q_6 \rangle_2$	0.000758(14)	0.000789(11)	0.0008274(91)	0.0008517(77)	0.0008913(70)
	$\langle Q_7 \rangle_2$	0.2045(36)	0.2243(30)	0.2466(25)	0.2655(22)	0.2897(21)
	$\langle Q_8 \rangle_2$	0.846(16)	0.880(13)	0.922(10)	0.9488(86)	0.9922(79)
	$\langle Q_9 \rangle_2$	0.02026(24)	0.02161(19)	0.02295(16)	0.02376(15)	0.02464(14)
	$\langle Q_{10} \rangle_2$	0.02006(24)	0.02141(19)	0.02272(16)	0.02353(15)	0.02439(14)

of unphysical effects. The empty and filled symbols indicate the data from $V = 16^3$ and 24^3 volumes, respectively. Within the statistical errors at each m_f and the fluctuation for different values of m_f, both of which are larger for the smaller spatial size 16^3, the data from the two spatial volumes do not show indications of the presence of finite size effects.

The remaining matrix elements $\langle Q_{7,8} \rangle_0$ for the $\Delta I = 1/2$ amplitude, which do not require the subtraction, are shown in Fig. 8. These matrix elements are well determined and exhibit clear m_M^2 dependences.

The matrix elements for the $\Delta I = 3/2$ channel given by $\langle Q_1 \rangle_2 = \langle Q_2 \rangle_2$ and $\langle Q_{7,8} \rangle_2$ are plotted in Fig. 9. Their statistical quality and m_M^2 dependence are similar to those for $\langle Q_{7,8} \rangle_0$.

As discussed in Sec. IV A, for extracting the values in the chiral limit, we adopt a quadratic polynomial form

$$\langle Q_i \rangle_I = \xi_0 + \xi_1 m_M^2 + \xi_3 m_M^4 . \tag{4.10}$$

In addition we also employ the chiral logarithm form

$$\langle Q_i \rangle_I = \xi_0 + \xi_1 m_M^2 + \xi_2 m_M^2 \ln m_M^2 . \tag{4.11}$$

TABLE X. Same as Table IX for the $24^3\times 32$ lattice.

	$m_f a$	0.02	0.03	0.04	0.05	0.06
bare	$\langle Q_1\rangle_0$	−0.0235(34)	−0.0205(37)	−0.0217(25)	−0.0161(22)	−0.0196(19)
[GeV^3]	$\langle Q_2\rangle_0$	0.0460(28)	0.0457(27)	0.0378(19)	0.0351(16)	0.0345(11)
	$\langle Q_3\rangle_0$	0.013(12)	0.021(13)	0.0010(98)	0.0116(81)	0.0003(68)
	$\langle Q_4\rangle_0$	0.082(11)	0.087(12)	0.0600(91)	0.0627(74)	0.0544(58)
	$\langle Q_5\rangle_0$	−0.027(14)	−0.044(13)	−0.0515(97)	−0.0393(82)	−0.0442(65)
	$\langle Q_6\rangle_0$	−0.105(26)	−0.183(24)	−0.167(17)	−0.136(14)	−0.117(11)
	$\langle Q_7\rangle_0$	1.697(15)	2.157(29)	2.563(35)	2.990(40)	3.295(44)
	$\langle Q_8\rangle_0$	5.211(44)	6.584(85)	7.84(11)	9.13(12)	10.08(13)
	$\langle Q_9\rangle_0$	−0.0417(28)	−0.0412(28)	−0.0324(20)	−0.0299(17)	−0.0295(12)
	$\langle Q_{10}\rangle_0$	0.0278(34)	0.0250(38)	0.0267(26)	0.0212(22)	0.0246(19)
	$\langle Q_1\rangle_2$	0.013154(43)	0.014163(52)	0.014781(48)	0.015335(45)	0.015853(43)
	$\langle Q_2\rangle_2$	0.013154(43)	0.014163(52)	0.014781(48)	0.015335(45)	0.015853(43)
	$\langle Q_7\rangle_2$	0.3996(15)	0.4222(18)	0.4559(15)	0.4900(14)	0.5184(13)
	$\langle Q_8\rangle_2$	1.2119(48)	1.2444(55)	1.3128(45)	1.3783(41)	1.4271(40)
	$\langle Q_9\rangle_2$	0.019730(65)	0.021244(78)	0.022172(72)	0.023003(67)	0.023779(65)
	$\langle Q_{10}\rangle_2$	0.019730(65)	0.021244(78)	0.022172(72)	0.023003(67)	0.023779(65)
	$m_f a$	0.02	0.03	0.04	0.05	0.06
renormalized	$\langle Q_1\rangle_0$	−0.0203(34)	−0.0173(36)	−0.0182(25)	−0.0130(21)	−0.0163(19)
at 1.3 GeV	$\langle Q_2\rangle_0$	0.0433(33)	0.0401(34)	0.0322(23)	0.0309(19)	0.0310(14)
[GeV^3]	$\langle Q_3\rangle_0$	0.015(14)	0.017(14)	−0.004(11)	0.0084(88)	−0.0014(73)
	$\langle Q_4\rangle_0$	0.078(13)	0.076(14)	0.048(10)	0.0535(84)	0.0466(65)
	$\langle Q_5\rangle_0$	−0.008(12)	−0.011(11)	−0.0214(90)	−0.0144(74)	−0.0231(57)
	$\langle Q_6\rangle_0$	−0.072(20)	−0.132(19)	−0.120(14)	−0.095(11)	−0.0790(84)
	$\langle Q_7\rangle_0$	0.8415(80)	1.072(15)	1.271(17)	1.488(19)	1.637(21)
	$\langle Q_8\rangle_0$	3.631(33)	4.566(60)	5.434(70)	6.352(79)	7.002(86)
	$\langle Q_9\rangle_0$	−0.0376(33)	−0.0338(34)	−0.0247(24)	−0.0233(20)	−0.0231(14)
	$\langle Q_{10}\rangle_0$	0.0259(34)	0.0234(37)	0.0256(26)	0.0205(21)	0.0239(19)
	$\langle Q_1\rangle_2$	0.013469(44)	0.014499(53)	0.015140(49)	0.015717(46)	0.016253(44)
	$\langle Q_2\rangle_2$	0.013295(44)	0.014317(53)	0.014944(49)	0.015507(45)	0.016031(43)
	$\langle Q_3\rangle_2$	−0.00002694(11)	−0.00003018(14)	−0.00003331(13)	−0.00003662(13)	−0.00003960(13)
	$\langle Q_4\rangle_2$	−0.0002180(15)	−0.0002301(17)	−0.0002476(15)	−0.0002660(13)	−0.0002807(13)
	$\langle Q_5\rangle_2$	0.0002037(15)	0.0002142(17)	0.0002312(15)	0.0002492(13)	0.0002634(13)
	$\langle Q_6\rangle_2$	0.0007562(57)	0.0007728(63)	0.0008144(54)	0.0008575(48)	0.0008866(46)
	$\langle Q_7\rangle_2$	0.2010(15)	0.2180(17)	0.2409(15)	0.2658(14)	0.2866(14)
	$\langle Q_8\rangle_2$	0.8440(64)	0.8618(70)	0.9078(60)	0.9552(53)	0.9872(51)
	$\langle Q_9\rangle_2$	0.020281(66)	0.021830(80)	0.022796(74)	0.023666(69)	0.024474(66)
	$\langle Q_{10}\rangle_2$	0.020083(66)	0.021623(80)	0.022575(73)	0.023431(68)	0.024228(66)

In Tables XII and XIII, results from these chiral extrapolations are summarized with the values of χ^2/dof. The differences between two types of fits should be taken as a measure of systematic error. For $\langle Q_6\rangle_0$, one observes in Fig. 7 an exceptional behavior of the data at $m_f=0.02$. An additional chiral extrapolation excluding this quark mass is hence also made for comparison and the fit lines indicated in the figures are obtained.

C. *B* parameters

We convert renormalized hadronic matrix elements at $\mu=m_c=1.3$ GeV into B parameters defined by [41]

$$B_1^{(1/2)}=-\frac{9}{X}\langle Q_1\rangle_0, \tag{4.12}$$

$$B_2^{(1/2)}=\frac{9}{5X}\langle Q_2\rangle_0, \tag{4.13}$$

$$B_3^{(1/2)}=\frac{3}{X}\langle Q_3\rangle_0, \tag{4.14}$$

$$B_5^{(1/2)}=\frac{3}{Y}\langle Q_5\rangle_0, \tag{4.15}$$

TABLE XI. Renormalized hadronic matrix elements at $\mu = 1.3$ GeV in units of GeV^3 from different matching points $q^* = 1/a$ (left column) and π/a (right column). Values are taken at $m_f a = 0.02$ on a $24^3 \times 32$ lattice.

	$q^* = 1/a$	$q^* = \pi/a$
$\langle Q_1 \rangle_0$	−0.0203(34)	−0.0152(33)
$\langle Q_2 \rangle_0$	0.0433(33)	0.0424(33)
$\langle Q_3 \rangle_0$	0.015(14)	0.019(14)
$\langle Q_4 \rangle_0$	0.078(13)	0.076(13)
$\langle Q_5 \rangle_0$	−0.008(12)	−0.005(12)
$\langle Q_6 \rangle_0$	−0.072(20)	−0.050(16)
$\langle Q_7 \rangle_0$	0.8415(80)	0.7986(77)
$\langle Q_8 \rangle_0$	3.631(33)	2.873(26)
$\langle Q_9 \rangle_0$	−0.0376(33)	−0.0317(33)
$\langle Q_{10} \rangle_0$	0.0259(34)	0.0257(34)
$\langle Q_1 \rangle_2$	0.013469(44)	0.014314(46)
$\langle Q_2 \rangle_2$	0.013295(44)	0.013760(45)
$\langle Q_7 \rangle_2$	0.2010(15)	0.1912(14)
$\langle Q_8 \rangle_2$	0.8440(64)	0.6678(51)
$\langle Q_9 \rangle_2$	0.020281(66)	0.021754(70)
$\langle Q_{10} \rangle_2$	0.020083(66)	0.021149(69)

$$B_6^{(1/2)} = \frac{1}{Y}\langle Q_6 \rangle_0, \tag{4.16}$$

$$B_7^{(1/2)} = -\frac{\langle Q_7 \rangle_0}{\frac{1}{6}Y(\kappa+1) - \frac{1}{2}X}, \tag{4.17}$$

$$B_8^{(1/2)} = -\frac{\langle Q_8 \rangle_0}{\frac{1}{2}Y(\kappa+1) - \frac{1}{6}X}, \tag{4.18}$$

$$B_1^{(3/2)} = \frac{9}{4\sqrt{2}X}\langle Q_1 \rangle_2, \tag{4.19}$$

$$B_7^{(3/2)} = -\frac{\langle Q_7 \rangle_2}{\frac{\kappa}{6\sqrt{2}}Y + \frac{1}{\sqrt{2}}X}, \tag{4.20}$$

$$B_8^{(3/2)} = -\frac{\langle Q_8 \rangle_2}{\frac{\kappa}{2\sqrt{2}}Y + \frac{\sqrt{2}}{6}X}, \tag{4.21}$$

where

$$\kappa = \frac{f_\pi}{f_K - f_\pi}, \quad X = \sqrt{3} f_\pi (m_K^2 - m_\pi^2),$$

$$Y = -4\sqrt{3}\left[\frac{m_K^2}{m_s + m_d}\right]^2 \frac{f_\pi}{\kappa}. \tag{4.22}$$

We summarize the values of B parameters in the chiral limit obtained by the fit with quadratic polynomial or chiral logarithm in Table XIV. Quark masses and other parameters used in the calculations are given in Appendix B.

Let us compare our values of B parameters with typical ones quoted in phenomenology (see, e.g., [41]). For the B parameters important for the $\Delta I = 1/2$ rule, the experimental value of $\mathrm{Re}\, A_2$ indicates $B_{1,\mathrm{NDR}}^{(3/2)}(m_c) = 0.453$ with $\Lambda_{\overline{\mathrm{MS}}}^{(4)} = 325$ MeV, with which our value $B_1^{(3/2)}(m_c) \approx 0.4$ to 0.5 is consistent. On the other hand, our results $B_1^{(1/2)}(m_c) \approx 8$ to 9 and $B_2^{(1/2)}(m_c) \approx 3$ to 4 are smaller than $B_1^{(1/2)}(m_c) \simeq 15$ and $B_{2,\mathrm{NDR}}^{(1/2)}(m_c) = 6.6$ needed to explain the experimental value of $\mathrm{Re}\, A_0$. For the parameter $B_6^{(1/2)}$ relevant for the direct CP violation, the largest of our estimate $B_6^{(1/2)}(m_c) \approx 0.3$ from the four-point fit of the data from the 24^3 spatial volume is still much smaller than $B_6^{(1/2)} = 1$ in the $1/N_c$ approach, while $B_8^{(3/2)}(m_c) \approx 0.9$ is comparable to $B_8^{(3/2)} = 1$ again in the $1/N_c$ approach. In general the B parameters for $I = 0$ are smaller than the usual estimates.

Previous studies gave $B_7^{(3/2)}$ ($\mu = 2$ GeV,NDR) $= 0.58(7)$ and $B_8^{(3/2)}(\mu = 2$ GeV,NDR$) = 0.81(4)$ [20], $B_7^{(3/2)}$ ($\mu = 2$ GeV,RI(MOM)) $= 0.38(11)$ and $B_8^{(3/2)}(\mu = 2$ GeV,RI(MOM)$) = 0.77(9)$ [21], $B_7^{(3/2)}$ ($\mu = 2$ GeV,NDR) $= 0.58(9)$ and $B_8^{(3/2)}(\mu = 2$ GeV,NDR$) = 0.80(9)$ [22], from quenched lattice QCD, and $B_7^{(3/2)}(\mu = 2$ GeV,NDR$) = 0.55(12)$ and $B_8^{(3/2)}(\mu = 2$ GeV,NDR$) = 1.11(28)$ from dispersive sum rules where $m_s + m_d = 100$ MeV is used [48]. Our values are $B_7^{(3/2)}(\mu = 1.3$ GeV,NDR$) = 0.62(3)$ and $B_8^{(3/2)}(\mu = 1.3$ GeV,NDR$) = 0.92(4)$ on a $24^3 \times 32$ lattice in broad agreement with the above. Note that the scale μ is different between our results and those of other studies.

V. PHYSICAL RESULTS

A. $\Delta I = 1/2$ rule

The real part of A_I relevant for the $\Delta I = 1/2$ rule is written as

$$\mathrm{Re}\, A_I = \frac{G_F}{\sqrt{2}} |V_{\mathrm{ud}}| \cdot |V_{\mathrm{us}}| \left[\sum_{i=1,2} z_i(m_c) \langle Q_i \rangle_I(m_c) + (\mathrm{Re}\, \tau) \sum_{i=3}^{10} y_i(m_c) \langle Q_i \rangle_I(m_c) \right]. \tag{5.1}$$

In Table XV, we list the values of $\mathrm{Re}\, A_0$, $\mathrm{Re}\, A_2$, and $\omega^{-1} = \mathrm{Re}\, A_0 / \mathrm{Re}\, A_2$ for each value of m_f and spatial volume, and for the three choices of the Λ parameter $\Lambda_{\overline{\mathrm{MS}}}^{(4)} = 325$, 215, and 435 MeV.

Figure 10 plots $\mathrm{Re}\, A_2$ (left panel) and $\mathrm{Re}\, A_0$ (right panel) as functions of m_M^2 for $\Lambda_{\overline{\mathrm{MS}}}^{(4)} = 325$ MeV. In both panels, empty and filled symbols denote the results from the volume $V = 16^3$ and 24^3, respectively. Signals for $\mathrm{Re}\, A_2$ are quite clean, while those for $\mathrm{Re}\, A_0$ exhibit more fluctuations. Since both amplitudes show a variation with m_M^2, we need to extrapolate them to the chiral limit to extract the physical pre-

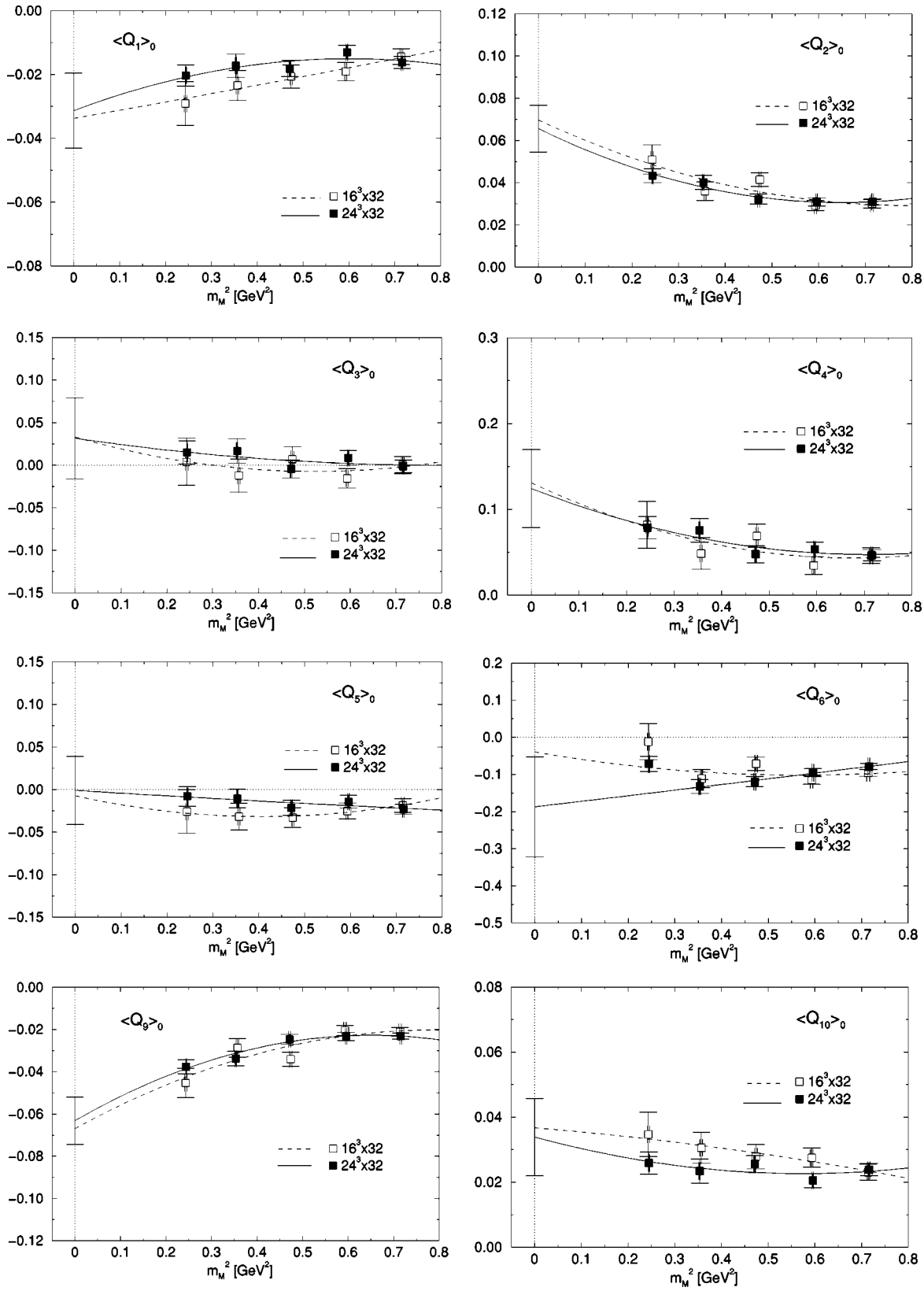

FIG. 7. Physical hadronic matrix elements $\langle Q_i \rangle_0$ for $i=1,2,3,4,5,6,9,$ and 10 as a function of m_M^2 from top to bottom. These matrix elements involve subtractions of unphysical effects. Empty and filled symbols are from the spatial volume $V=16^3$ and 24^3, respectively. Chiral extrapolations with a quadratic polynomial are shown by solid ($V=24^3$) and dashed ($V=16^3$) lines. Fit error in the chiral limit is added for the former.

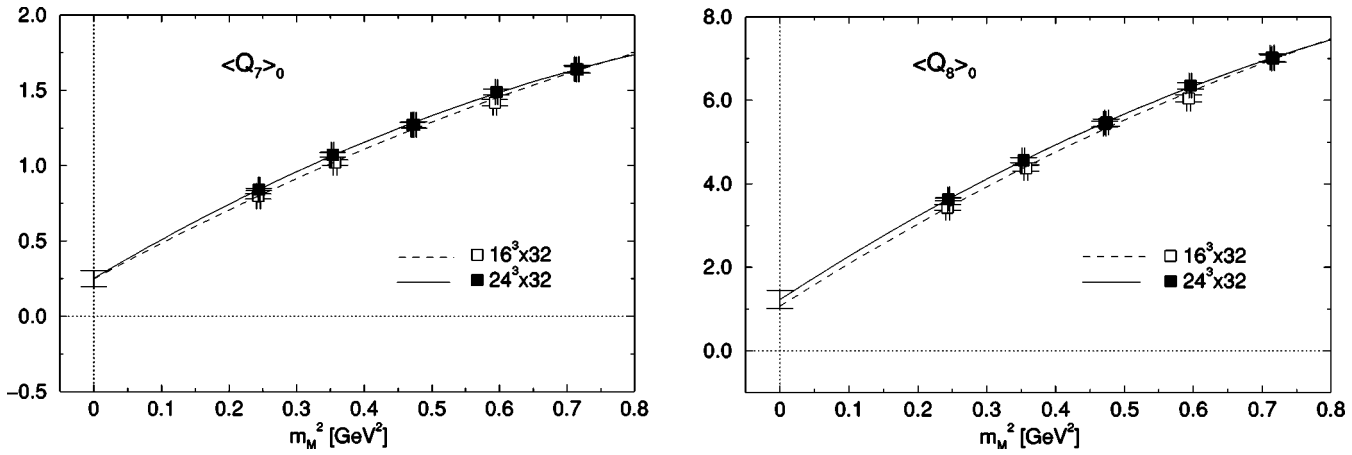

FIG. 8. Physical hadronic matrix elements $\langle Q_{7,8}\rangle_0$ as a function of m_M^2. The organization of each panel is the same as that in Fig. 7.

diction. Following the analysis in Sec. IV A, we examine two types of fit functions given by

$$\mathrm{Re}\,A_I = \begin{cases} \xi_0+\xi_1 m_M^2+\xi_3 (m_M^2)^2 & \text{(quadratic polynomial)}, \\ \xi_0+\xi_1 m_M^2+\xi_2 m_M^2 \ln m_M^2 & \text{(chiral logarithm)}. \end{cases} \tag{5.2}$$

Chiral extrapolations from the quadratic fit are indicated by solid lines, and those from the chiral logarithm fit by dashed lines in Fig. 10.

For the $\Delta I=3/2$ amplitude plotted on the left, the extrapolated values show good agreement with the experimental value $\mathrm{Re}\,A_2=1.50\times10^{-8}$ GeV indicated by the horizontal arrow. On the other hand, the $\Delta I=1/2$ amplitude $\mathrm{Re}\,A_0$ is small at measured values of quark masses, and only amounts to about 50–60 % of the experimental value 33.3×10^{-8} GeV even after the chiral extrapolation.

A breakdown of the amplitudes into contributions from the ten operators Q_i with $i=1,\ldots,10$ is illustrated in Fig. 11 for $m_f a=0.03$. The histograms for the $V=16^3$ and 24^3 cases are shown by dashed and solid lines, respectively. The horizontal lines with statistical errors indicate the total amplitude, the dashed and solid lines corresponds to $V=16^3$ and 24^3. An apparent absence of contributions from the operators with $i=3,\ldots,10$ is due to the small value of the parameter $\mathrm{Re}\,\tau\approx0.002$; the real part of the decay amplitudes is determined by the matrix elements $\langle Q_1\rangle_I$ and $\langle Q_2\rangle_I$, with the latter providing the dominant part.

The ratio $\omega^{-1}=\mathrm{Re}\,A_0/\mathrm{Re}\,A_2$ is shown in Fig. 12. Reflecting an insufficient enhancement of the $\Delta I=1/2$ amplitude, it only rises to about half of the experimental value $\omega^{-1}\approx22$. The situation hardly changes for $\Lambda^{(4)}_{\overline{\mathrm{MS}}}=215$ or 435 MeV, for which the amplitudes shift by about 5–10 % (see Table XV). We collect chiral fit parameters for the case of larger spatial volume $V=24^3$ in Table XVI.

Altogether we find

$$\mathrm{Re}\,A_0=16.5(2.2)(+4.2)(+0.7)(^{+0.8}_{-1.6})\times10^{-8}\ \ [\mathrm{GeV}], \tag{5.3}$$

$$\mathrm{Re}\,A_2=1.531(26)(-178)(-4)(^{+70}_{-38})\times10^{-8}\ \ [\mathrm{GeV}], \tag{5.4}$$

$$\omega^{-1}=9.5(1.1)(+2.8)(0.6)(^{+0.7}_{-1.3}). \tag{5.5}$$

The central values are taken from the result on a $24^3\times32$ lattice from the quadratic polynomial fit with $\Lambda^{(4)}_{\overline{\mathrm{MS}}}=325$ MeV. The first error is statistical, the second one is an estimate of uncertainty of chiral extrapolation using the chiral logarithm fit, the third one is finite-size variation estimated by the change of value for the $V=16^3$ lattice, and the fourth one, associated with renormalization, is estimated as the largest variation under changes of $\Lambda^{(4)}_{\overline{\mathrm{MS}}}$, q^*, and the RG-running. If the chiral symmetry breaking term ξ_{-1}/m_M^2 is included in the chiral fit (5.2), a nonzero value of ξ_{-1} beyond the statistical error is obtained only for $\mathrm{Re}\,A_2$, resulting in a 60% increase of the value of $\mathrm{Re}\,A_2$. The disagreement from experiment becomes worse in this case. The scaling violation and the quenching error, which cannot be estimated in our calculation, are not included in our systematic uncertainty. In particular, the physical scale of lattice spacing set by the string tension in this paper may differ by about 10–20 % from scales determined by other physical quantities due to the quenched approximation. This uncertainty is not included in the above error estimate.

B. Direct *CP* violation (ε'/ε)

The formula (1.4) for ε'/ε can be rewritten as

$$\varepsilon'/\varepsilon=\mathrm{Im}(V_{ts}^* V_{td})[P^{(1/2)}-P^{(3/2)}], \tag{5.6}$$

$$P^{(1/2)}=r\sum_i y_i(\mu)\langle Q_i\rangle_0(\mu)(1-\Omega_{\eta+\eta'}), \tag{5.7}$$

$$P^{(3/2)}=\frac{r}{\omega}\sum_i y_i(\mu)\langle Q_i\rangle_2(\mu), \tag{5.8}$$

where

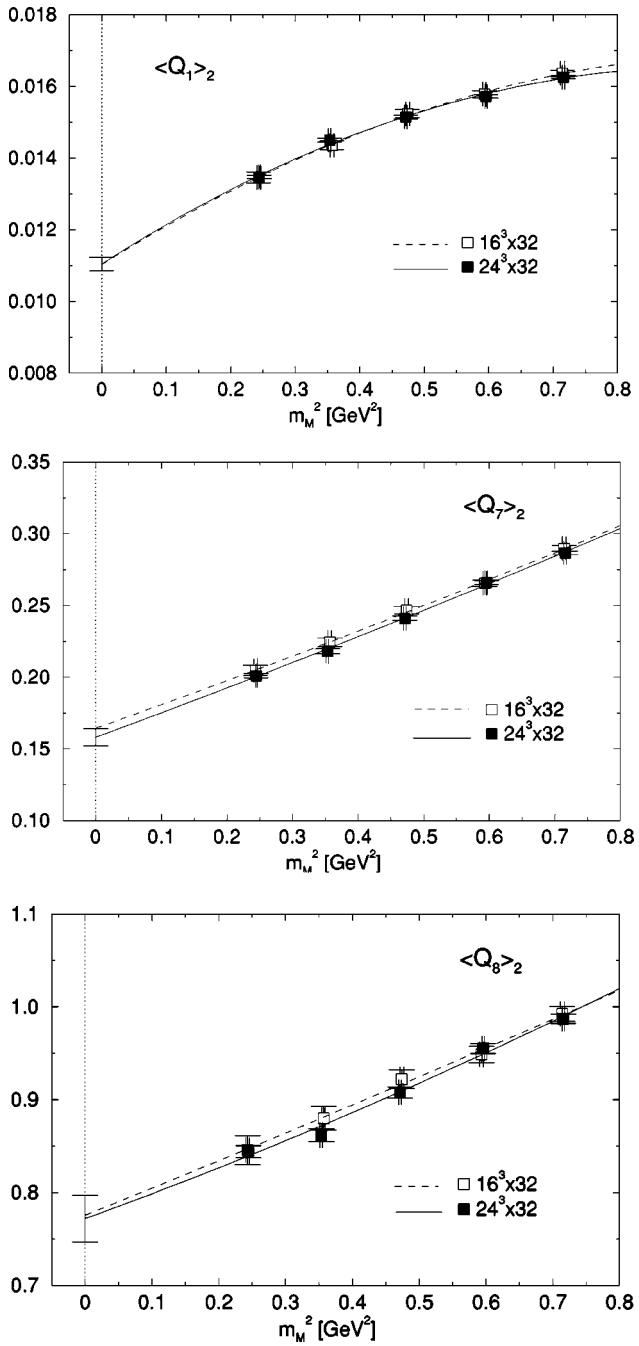

FIG. 9. Physical hadronic matrix elements $\langle Q_1\rangle_2$ and $\langle Q_{7,8}\rangle_2$ as a function of m_M^2. The organization of each panel is the same as that in Fig. 7.

$$r \equiv \frac{G_F \omega}{2|\varepsilon| \mathrm{Re}\, A_0} \tag{5.9}$$

and the parameter $\Omega_{\eta+\eta'}=0.25(5)$ reflects the isospin breaking. Since the $\Delta I=1/2$ rule is only partially reproduced with our data, we employ the experimental values for $\mathrm{Re}\, A_0$, ω, and ε as input.

In Fig. 13 our data for $P^{(3/2)}$ (left panel) and $P^{(1/2)}$ (right panel) calculated with $\Lambda^{(4)}_{\overline{\mathrm{MS}}}=325$ MeV are plotted as a function of m_M^2. Results for ε'/ε are shown in Fig. 14. Since $P^{(1/2)}$ is smaller than $P^{(3/2)}$ in our data, ε'/ε tends to be negative.

TABLE XII. Hadronic matrix elements in units of GeV^3 in the chiral limit $m_M^2 \to 0$ on a $16^3\times 32$ lattice. The columns named "quadratic," "chiral log." correspond to two types of fit forms described in the text. Chiral extrapolations are made using data at all $m_f a = 0.02$–0.06 (5 points) except for an alternative extrapolation of $\langle Q_6\rangle_0$ excluding the point at $m_f a = 0.02$ (4 points).

	quadratic	χ^2/dof	chiral log.	χ^2/dof
$\langle Q_1\rangle_0$	−0.034(20)	0.14	−0.035(36)	0.14
$\langle Q_2\rangle_0$	0.070(19)	3.03	0.083(34)	3.05
$\langle Q_3\rangle_0$	0.033(82)	0.91	0.06(15)	0.94
$\langle Q_4\rangle_0$	0.131(78)	1.68	0.17(14)	1.71
$\langle Q_5\rangle_0$	−0.008(72)	0.03	0.03(13)	0.02
$\langle Q_6\rangle_0$	0.08(12)	2.64	0.20(21)	2.63
$\langle Q_6\rangle_0$ (4 pts.)	−0.04(17)	4.32	−0.02(31)	4.38
$\langle Q_7\rangle_0$	0.247(78)	1.78	0.11(15)	1.69
$\langle Q_8\rangle_0$	1.07(32)	2.87	0.48(60)	2.77
$\langle Q_9\rangle_0$	−0.067(19)	3.32	−0.082(35)	3.35
$\langle Q_{10}\rangle_0$	0.037(21)	0.17	0.037(37)	0.17
$\langle Q_1\rangle_2$	0.01102(54)	0.34	0.00990(98)	0.29
$\langle Q_2\rangle_2$	0.01087(54)	0.33	0.00975(97)	0.28
$\langle Q_3\rangle_2$	−0.0000203(12)	0.49	−0.0000195(21)	0.46
$\langle Q_4\rangle_2$	−0.000188(12)	0.33	−0.000187(22)	0.37
$\langle Q_5\rangle_2$	0.000177(12)	0.33	0.000179(23)	0.34
$\langle Q_6\rangle_2$	0.000694(46)	0.31	0.000694(83)	0.31
$\langle Q_7\rangle_2$	0.164(12)	0.36	0.167(23)	0.38
$\langle Q_8\rangle_2$	0.776(51)	0.30	0.775(92)	0.31
$\langle Q_9\rangle_2$	0.01660(81)	0.34	0.0149(15)	0.29
$\langle Q_{10}\rangle_2$	0.01642(81)	0.33	0.0147(15)	0.29

A breakdown of $P^{(3/2)}$ and $P^{(1/2)}$ into contributions from the operators $Q_i (i=3,\ldots,10)$ is displayed for the case of $m_f a=0.03$ in Fig. 15, where dashed and solid lines denote data from $V=16^3$ and 24^3, respectively. This figure demonstrates that $\langle Q_8\rangle_2$ and $\langle Q_6\rangle_0$ are, respectively, dominant in $P^{(3/2)}$ and $P^{(1/2)}$ as usually considered. However, the matrix element of $\langle Q_6\rangle_0$ is too small; if the experimental value of ε'/ε is to be reproduced by a change of this matrix element, it has to be increased by about a factor of 5.

Numerical values of $P^{(1/2)}, P^{(3/2)}$, and ε'/ε for each m_f are summarized in Table XVII. In addition to the features of the data discussed above, we observe that changing the Λ parameter from $\Lambda^{(4)}_{\overline{\mathrm{MS}}}=325$ to 215 MeV decreases $P^{(1/2)}$ by 20% and $P^{(3/2)}$ by 25%. Employing $\Lambda^{(4)}_{\overline{\mathrm{MS}}}=435$ MeV leads to an increase by similar percentages for the two functions. Therefore the trend toward a negative value of ε'/ε is not altered.

If we make a quadratic chiral extrapolation we find $\varepsilon'/\varepsilon = -7.7(2.0)\times 10^{-4}$ with $\chi^2/\mathrm{dof}=1.75$ on a $24^3\times 32$ lattice. Including the chiral symmetry breaking term ξ_{-1}/m_M^2 in the fit changes this value to $+30(20)\times 10^{-4}$ with $\chi^2/\mathrm{dof} = 0.0015$. The small χ^2 indicates that more data points, in particular data at smaller masses, are necessary to constrain

TABLE XIII. Same as Table XII for the $24^3\times 32$ lattice.

	quadratic	χ^2/dof	chiral log.	χ^2/dof
$\langle Q_1\rangle_0$	−0.031(12)	0.98	−0.039(21)	1.04
$\langle Q_2\rangle_0$	0.066(11)	0.36	0.082(20)	0.43
$\langle Q_3\rangle_0$	0.032(48)	0.83	0.044(86)	0.82
$\langle Q_4\rangle_0$	0.124(45)	0.69	0.155(82)	0.69
$\langle Q_5\rangle_0$	0.001(40)	0.44	0.003(73)	0.43
$\langle Q_6\rangle_0$	0.014(66)	1.53	0.16(12)	1.20
$\langle Q_6\rangle_0$(4 pts.)	−0.19(13)	0.10	−0.18(25)	0.10
$\langle Q_7\rangle_0$	0.252(53)	0.43	0.07(11)	0.45
$\langle Q_8\rangle_0$	1.23(22)	0.27	0.58(43)	0.35
$\langle Q_9\rangle_0$	−0.063(11)	0.45	−0.082(20)	0.53
$\langle Q_{10}\rangle_0$	0.034(12)	1.09	0.039(22)	1.14
$\langle Q_1\rangle_2$	0.01104(19)	4.55	0.00979(36)	2.99
$\langle Q_2\rangle_2$	0.01089(19)	4.79	0.00964(35)	3.16
$\langle Q_3\rangle_2$	−0.00001942(50)	0.25	−0.00001832(96)	0.18
$\langle Q_4\rangle_2$	−0.0001848(59)	1.28	−0.000187(11)	1.25
$\langle Q_5\rangle_2$	0.0001737(61)	1.67	0.000179(11)	1.57
$\langle Q_6\rangle_2$	0.000691(22)	2.08	0.000708(42)	1.98
$\langle Q_7\rangle_2$	0.1580(60)	1.27	0.163(11)	1.18
$\langle Q_8\rangle_2$	0.772(25)	2.09	0.792(47)	1.99
$\langle Q_9\rangle_2$	0.01663(28)	4.48	0.01476(54)	2.94
$\langle Q_{10}\rangle_2$	0.01646(28)	4.66	0.01458(53)	3.07

the fit parameters well. The existence of large uncertainties associated with the possible presence of the chiral breaking term, and also a subtle quenching effect mentioned below, make it difficult to draw a conclusive estimate of ε'/ε.

Recently, Golterman and Pallante pointed out that the relation between $K\to\pi$ and $K\to\pi\pi$ matrix elements in chiral perturbation theory should be modified in the quenched theory [49]. We have applied the modified relation to the $Q^{(0)}_{5,6}$ matrix elements and found that the effect is large, ranging between 20% and 100% in magnitude. For example, the renormalized $\langle Q_6\rangle_0$ on a $24^3\times 32$ lattice increases in magnitude to $-0.154(17)$, $-0.182(16)$, $-0.144(11)$, $-0.1238(90)$, and $-0.0969(72)$ at $m_f=0.02$, 0.03, 0.04, 0.05, and 0.06, respectively. (This modification has been tested also in the case of the staggered fermion [50], and an increase of $\langle Q_6\rangle_0$ of a similar magnitude has been observed.) In terms of ε'/ε, the modified relation leads to $-1.70(53)$, $-0.53(51)$, $-1.48(32)$, $-2.09(26)$, and $-2.85(19)$ for $\Lambda^{(4)}_{\overline{\rm MS}}=325$ MeV. The modification increases the value of ε'/ε, but it is still negative. A complete analysis still remains to be made both in the theoretical analyses of the relation in quenched chiral perturbation theory and in numerical simulations.

TABLE XIV. B parameters in the chiral limit with the chiral logarithm fit.

	$16^3\times 32$		$24^3\times 32$	
	quadratic	chiral log.	quadratic	chiral log.
$B^{(1/2)}_1$	8.3(5.0)	8.6(8.9)	7.7(2.9)	9.6(5.2)
$B^{(1/2)}_2$	3.43(95)	4.1(1.7)	3.23(55)	4.04(98)
$B^{(1/2)}_3$	2.7(6.7)	5(12)	2.6(3.9)	3.6(7.1)
$B^{(1/2)}_4$	3.6(2.1)	4.5(3.8)	3.4(1.2)	4.3(2.3)
$B^{(1/2)}_5$	0.04(40)	−0.15(71)	0.01(22)	−0.02(41)
$B^{(1/2)}_6$	−0.14(22)	−0.38(38)	−0.03(12)	−0.29(22)
$B^{(1/2)}_6$(4 pts.)	0.07(31)	0.03(58)	0.35(25)	0.34(47)
$B^{(1/2)}_7$	0.49(15)	0.22(29)	0.50(10)	0.14(21)
$B^{(1/2)}_8$	0.73(22)	0.32(41)	0.83(15)	0.39(29)
$B^{(1/2)}_9$	5.5(1.6)	6.8(2.8)	5.19(92)	6.7(1.7)
$B^{(1/2)}_{10}$	3.0(1.7)	3.0(3.0)	2.78(98)	3.2(1.8)
$B^{(3/2)}_1$	0.480(24)	0.431(43)	0.4809(82)	0.426(16)
$B^{(3/2)}_2$	0.473(23)	0.425(42)	0.4745(81)	0.420(15)
$B^{(3/2)}_7$	0.640(49)	0.651(88)	0.616(23)	0.634(44)
$B^{(3/2)}_8$	0.924(61)	0.92(11)	0.920(30)	0.944(55)
$B^{(3/2)}_9$	0.482(24)	0.433(43)	0.4830(82)	0.429(16)
$B^{(3/2)}_{10}$	0.477(24)	0.428(43)	0.4779(82)	0.423(15)

VI. CONCLUSIONS

In this paper we have presented results of our investigation into the reduction method in the framework of chiral perturbation theory at the lowest order to calculate the $K\to\pi\pi$ decay amplitudes. The $K\to\pi$ and $K\to 0$ hadronic matrix elements of four-quark operators were calculated in a quenched numerical simulation using domain-wall fermion action for quarks and an RG-improved gauge action for gluons to satisfy the requirements of chiral symmetry on the lattice. We have seen that the calculation of quark loop contractions which appear in Penguin diagrams by the random noise method works successfully. As a result the $\Delta I=1/2$ amplitudes which require subtractions with the quark loop contractions were obtained with a statistical accuracy of about 10%. We have investigated the chiral properties required for the $K\to\pi$ matrix elements. If we leave aside $Q^{(0)}_6$, we have found no strong sign for the existence of the chiral symmetry breaking effect within the statistical precision of our data in the range of quark masses employed in our simulations. However, $Q^{(0)}_6$ appears to show an exceptionally large chiral symmetry breaking effect compared to other channels. It is not clear to us if this is an effect beyond statistical fluctuation. For the definite conclusion on this point, more data, particularly at smaller quark masses, will be needed. Matching the lattice matrix elements to those in the continuum at $\mu=1/a$ with the perturbative renormalization factor to one loop order, and running to the scale $\mu=m_c=1.3$ GeV with the renormalization group, we obtained all the matrix elements needed for the decay amplitudes. Unfortunately the physical amplitudes thus calculated show unsatisfactory features.

One of the pathologies of our results is a poor enhancement of the $\Delta I=1/2$ decay amplitude; the value of $\mathrm{Re}\,A_0$ is about 50–60 % of the experimental one in contrast to $\mathrm{Re}\,A_2$ which reaches the expected value in the chiral limit. Another deficiency is a small value of the $\Delta I=1/2$ contribution to ε'/ε; if we assume that the $\Delta I=3/2$ contribution has a correct order of magnitude, the $\Delta I=1/2$ contribution is too small by about a factor of 5 to explain the experimental value $\simeq 2\times 10^{-3}$.

TABLE XV. Values of $\mathrm{Re}\,A_0$, $\mathrm{Re}\,A_2$, and ω^{-1} obtained at each $m_f a$ for both lattice sizes, with $\Lambda^{(4)}_{\overline{\mathrm{MS}}}=325$, 215, and 435 MeV.

	$16^3\times 32$			$24^3\times 32$		
	$\mathrm{Re}\,A_0[10^{-8}\mathrm{GeV}]$	$\mathrm{Re}\,A_2[10^{-8}\mathrm{GeV}]$	ω^{-1}	$\mathrm{Re}\,A_0[10^{-8}\mathrm{GeV}]$	$\mathrm{Re}\,A_2[10^{-8}\mathrm{GeV}]$	ω^{-1}
$\Lambda^{(4)}_{\overline{\mathrm{MS}}}=325$ MeV						
0.02	13.1(1.4)	1.867(22)	7.01(78)	10.80(69)	1.8689(62)	5.78(37)
0.03	9.45(84)	1.992(17)	4.75(43)	9.90(69)	2.0129(74)	4.92(35)
0.04	10.42(68)	2.114(15)	4.93(33)	8.26(45)	2.1006(68)	3.93(22)
0.05	7.66(49)	2.188(14)	3.50(22)	7.61(38)	2.1792(64)	3.49(17)
0.06	7.52(40)	2.267(13)	3.32(17)	7.86(28)	2.2527(61)	3.49(12)
$\Lambda^{(4)}_{\overline{\mathrm{MS}}}=215$ MeV						
0.02	12.5(1.4)	1.911(23)	6.55(72)	10.40(66)	1.9130(63)	5.43(34)
0.03	9.12(81)	2.039(18)	4.47(40)	9.59(66)	2.0602(76)	4.66(32)
0.04	10.04(64)	2.164(16)	4.64(31)	8.01(43)	2.1500(70)	3.72(20)
0.05	7.41(47)	2.240(14)	3.31(21)	7.38(36)	2.2306(65)	3.31(16)
0.06	7.30(38)	2.321(13)	3.15(16)	7.60(26)	2.3058(63)	3.29(12)
$\Lambda^{(4)}_{\overline{\mathrm{MS}}}=435$ MeV						
0.02	13.7(1.5)	1.821(22)	7.52(84)	11.20(72)	1.8228(60)	6.14(40)
0.03	9.78(89)	1.943(17)	5.03(46)	10.18(73)	1.9635(72)	5.19(38)
0.04	10.80(71)	2.062(15)	5.24(35)	8.50(48)	2.0489(67)	4.15(23)
0.05	7.87(51)	2.134(14)	3.69(24)	7.82(40)	2.1254(62)	3.68(19)
0.06	7.74(42)	2.211(12)	3.50(19)	8.11(29)	2.1970(60)	3.69(13)

The hadronic matrix elements for $\Delta I=1/2$ involve significant subtractions. For some of the matrix elements, this results in flips of sign and a reduction in the magnitude. Hence insufficient choices of lattice parameters in simulations may lead to sizable systematic errors in these matrix elements. Possible origins of the errors are (i) finite fifth-dimensional size N_5 of the domain wall fermion, (ii) finite spatial size N_s, (iii) finite lattice spacing a, (iv) quenching effects, and (v) the neglect of the charm quark. Our use of (vi) renormalization factors in one-loop order of perturbation theory is another source of error in the renormalized matrix elements. Finally (vii) higher order corrections in chiral perturbation theory is also a possible source of error. It may well be that the origin of the deficiency resides in physical phenomena

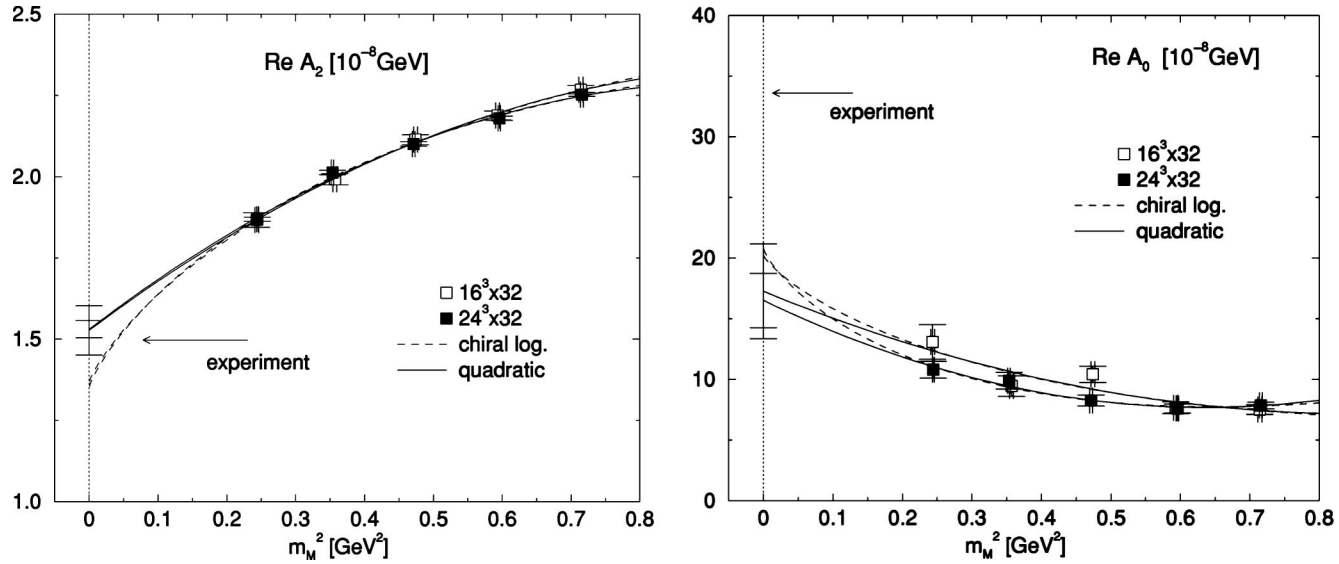

FIG. 10. $\mathrm{Re}\,A_2$ (left) and $\mathrm{Re}\,A_0$ (right) in units of GeV as a function of m_M^2. For chiral extrapolation, quadratic (solid) and chiral logarithm (dashed) forms are used. For the former, fit errors are shown in the chiral limit. Filled and empty symbols are for the spatial volume 24^3 and 16^3, respectively.

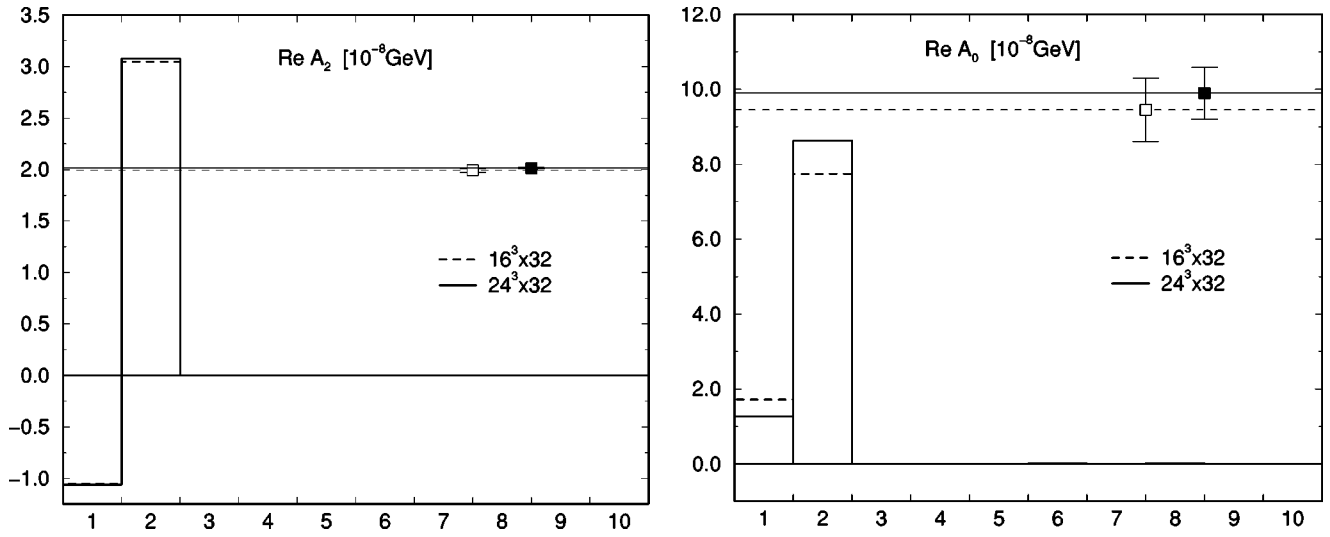

FIG. 11. Breakdown of $\mathrm{Re}\,A_2$ (left) and $\mathrm{Re}\,A_0$ (right) into contributions from the operators $Q_i (i=1,\ldots,10)$ at $m_f a = 0.03$. Data points placed on horizontal lines show total values and errors. The solid and dashed lines are for the spatial volume 24^3 and 16^3, respectively.

such as the effect of σ resonance which are difficult to take into account once the reduction to $K\to\pi$ matrix elements is made.

ACKNOWLEDGMENTS

We thank P. Weisz for informative discussions on the anomalous dimension of the four-quark operators. J.N., S.A., Y.A., S.H., and T.I. also thank the Institute for Nuclear Theory at the University of Washington for its hospitality and the Department of Energy for partial support during the completion of this work. This work was supported in part by Grants-in-Aid of the Ministry of Education (Nos. 10640246, 10640248, 10740107, 11640250, 11640294, 11740162, 12014202, 12304011, 12640253, 12740133, and 13640260). V.L. was supported by the JSPS Research for the Future Program (No. JSPS-RFTF 97P01102). J.N., S.E., and K.N. would like to thank the JSPS for financial support.

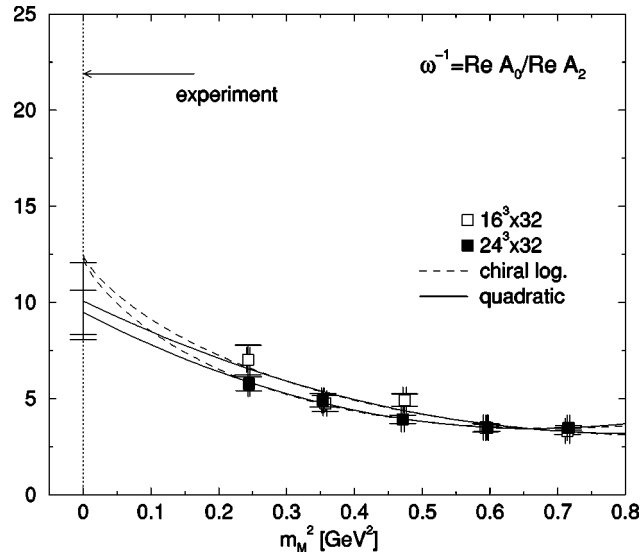

FIG. 12. $\mathrm{Re}\,A_0/\mathrm{Re}\,A_2$ as a function of m_M^2. For chiral extrapolation, quadratic form (solid line with the fit error at $m_M^2=0$) and chiral logarithm form (dashed line) are used. Empty and filled symbols are for the spatial volume 16^3 and 24^3, respectively.

APPENDIX A: DECOMPOSITION OF Q_i's INTO $\Delta I=1/2$ AND $\Delta I=3/2$ PARTS

Four-quark operators which transform under the irreducible representations of $SU(3)_L\otimes SU(3)_R$ chiral group and having definite isospin $I=0$ or 2 are given by

$$\mathcal{X}^{(2)}_{\mathbf{27,1}} = (\bar{s}d)_L[(\bar{u}u)_L - (\bar{d}d)_L] + (\bar{s}u)_L(\bar{u}d)_L, \quad \text{(A1)}$$

$$\mathcal{X}^{(0)}_{\mathbf{27,1}} = (\bar{s}d)_L[(\bar{u}u)_L + 2(\bar{d}d)_L - 3(\bar{s}s)_L] + (\bar{s}u)_L(\bar{u}d)_L, \quad \text{(A2)}$$

$$\mathcal{X}^{(0)}_{\mathbf{8,1}} = (\bar{s}d)_L(\bar{u}u)_L - (\bar{s}u)_L(\bar{u}d)_L, \quad \text{(A3)}$$

$$\tilde{\mathcal{X}}^{(0)}_{\mathbf{8,1}} = (\bar{s}d)_L[(\bar{u}u)_L + 2(\bar{d}d)_L + 2(\bar{s}s)_L] + (\bar{s}u)_L(\bar{u}d)_L, \quad \text{(A4)}$$

$$\mathcal{Y}^{(0)}_{\mathbf{8,1}} = (\bar{s}d)_L[(\bar{u}u)_R + (\bar{d}d)_R + (\bar{s}s)_R], \ \mathcal{Y}^{(0)c}_{\mathbf{8,1}}, \quad \text{(A5)}$$

$$\mathcal{Y}^{(0)}_{\mathbf{8,8}} = (\bar{s}d)_L[(\bar{u}u)_R - (\bar{s}s)_R] - (\bar{s}u)_L(\bar{u}d)_R, \quad \mathcal{Y}^{(0)c}_{\mathbf{8,8}}, \quad \text{(A6)}$$

$$\mathcal{Y}^{(2)}_{\mathbf{8,8}} = (\bar{s}d)_L[(\bar{u}u)_R - (\bar{d}d)_R] + (\bar{s}u)_L(\bar{u}d)_R, \quad \mathcal{Y}^{(2)c}_{\mathbf{8,8}}, \quad \text{(A7)}$$

where we use the notation of $\mathcal{X}$'s and $\mathcal{Y}$'s for the Lorentz structure $L\otimes L$ and $L\otimes R$. The subscripts "**i,j**" stand for the representation (i_L, j_R) of the operator and the superscript (0) or (2) denotes the isospin. A shorthand notation, e.g.,

TABLE XVI. Fit parameters for $\mathrm{Re}\,A_0$, $\mathrm{Re}\,A_2$, and ω^{-1} with $\xi_0+\xi_1 m_M^2+\xi_3(m_M^2)^2$ (quadratic fit) and $\xi_0+\xi_1 m_M^2+\xi_2 m_M^2 \ln m_M^2$ (chiral logarithm fit). Results on a $24^3\times 32$ lattice with $\Lambda_{\overline{\mathrm{MS}}}^{(4)}=325$ MeV are shown.

$24^3\times 32$		ξ_0	ξ_1	ξ_2	ξ_3	χ^2/dof
quadratic	$\mathrm{Re}\,A_0[10^{-8}\mathrm{GeV}]$	16.5(2.2)	−27.7(9.2)		21.8(8.8)	0.34
	$\mathrm{Re}\,A_2[10^{-8}\mathrm{GeV}]$	1.531(26)	1.62(12)		−0.86(13)	4.91
	ω^{-1}	9.5(1.1)	−18.2(4.6)		13.7(4.3)	0.13
chiral log.	$\mathrm{Re}\,A_0[10^{-8}\mathrm{GeV}]$	20.7(4.0)	−11.4(2.8)	20.1(8.3)		0.50
	$\mathrm{Re}\,A_2[10^{-8}\mathrm{GeV}]$	1.353(50)	0.977(31)	−0.82(11)		3.25
	ω^{-1}	12.3(2.0)	−8.0(1.5)	12.9(4.1)		0.26

$(\overline{sd})_L=\overline{s}\gamma_\mu(1-\gamma_5)d$, is employed as in Eqs. (2.17)–(2.21), and $\mathcal{Y}_{\mathbf{i,j}}^{(I)c}$ equals $\mathcal{Y}_{\mathbf{i,j}}^{(I)}$ with its color summation changed to cross the two currents. In terms of these operators the independent local operators are rewritten as

$$Q_1=\frac{1}{2}\mathcal{X}_{\mathbf{8,1}}^{(0)}+\frac{1}{10}\tilde{\mathcal{X}}_{\mathbf{8,1}}^{(0)}+\frac{1}{15}\mathcal{X}_{\mathbf{27,1}}^{(0)}+\frac{1}{3}\mathcal{X}_{\mathbf{27,1}}^{(2)}, \tag{A8}$$

$$Q_2=-\frac{1}{2}\mathcal{X}_{\mathbf{8,1}}^{(0)}+\frac{1}{10}\tilde{\mathcal{X}}_{\mathbf{8,1}}^{(0)}+\frac{1}{15}\mathcal{X}_{\mathbf{27,1}}^{(0)}+\frac{1}{3}\mathcal{X}_{\mathbf{27,1}}^{(2)}, \tag{A9}$$

$$Q_3=\frac{1}{2}\mathcal{X}_{\mathbf{8,1}}^{(0)}+\frac{1}{10}\tilde{\mathcal{X}}_{\mathbf{8,1}}^{(0)}, \tag{A10}$$

$$Q_5=\mathcal{Y}_{\mathbf{8,1}}^{(0)}, \tag{A11}$$

$$Q_6=\mathcal{Y}_{\mathbf{8,1}}^{(0)c}, \tag{A12}$$

$$Q_7=\frac{1}{2}[\mathcal{Y}_{\mathbf{8,8}}^{(0)}+\mathcal{Y}_{\mathbf{8,8}}^{(2)}], \tag{A13}$$

$$Q_8=\frac{1}{2}[\mathcal{Y}_{\mathbf{8,8}}^{(0)c}+\mathcal{Y}_{\mathbf{8,8}}^{(2)c}]. \tag{A14}$$

Therefore the decomposition of the local operators into $\Delta I=1/2$ and $\Delta I=3/2$ parts is summarized as follows:

$\Delta I=1/2$:

$$Q_1^{(0)}=\frac{1}{3}[-(\overline{s}_a d_b)_L(\overline{u}_b u_a)_L+2(\overline{s}_a u_b)_L(\overline{u}_b d_a)_L +(\overline{s}_a d_b)_L(\overline{d}_b d_a)_L], \tag{A15}$$

$$Q_2^{(0)}=\frac{1}{3}[-(\overline{sd})_L(\overline{uu})_L+2(\overline{su})_L(\overline{ud})_L +(\overline{sd})_L(\overline{dd})_L], \tag{A16}$$

$$Q_3^{(0)}=(\overline{sd})_L[(\overline{uu})_L+(\overline{dd})_L+(\overline{ss})_L], \tag{A17}$$

$$Q_4^{(0)}=(\overline{s}_a d_b)_L[(\overline{u}_b u_a)_L+(\overline{d}_a d_b)_L+(\overline{s}_b s_a)_L], \tag{A18}$$

$$Q_5^{(0)}=(\overline{sd})_L[(\overline{uu})_R+(\overline{dd})_R+(\overline{ss})_R], \tag{A19}$$

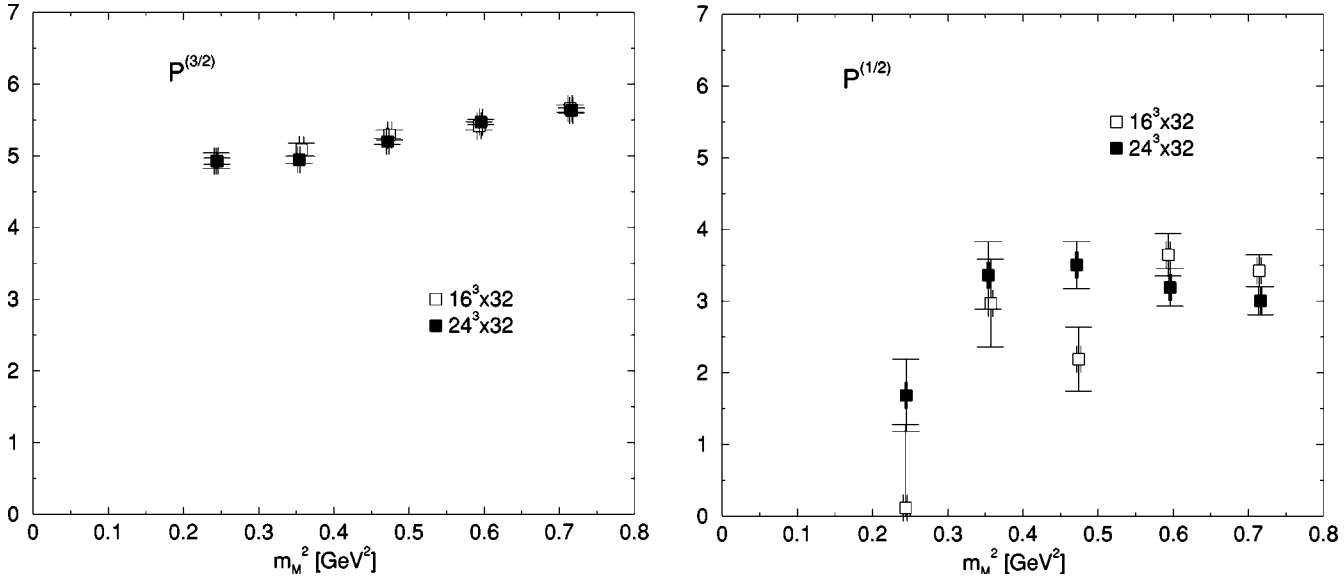

FIG. 13. $P^{(3/2)}$ (left) and $P^{(1/2)}$ (right) as a function of m_M^2. Empty and filled symbols are for the spatial volume 16^3 and 24^3, respectively.

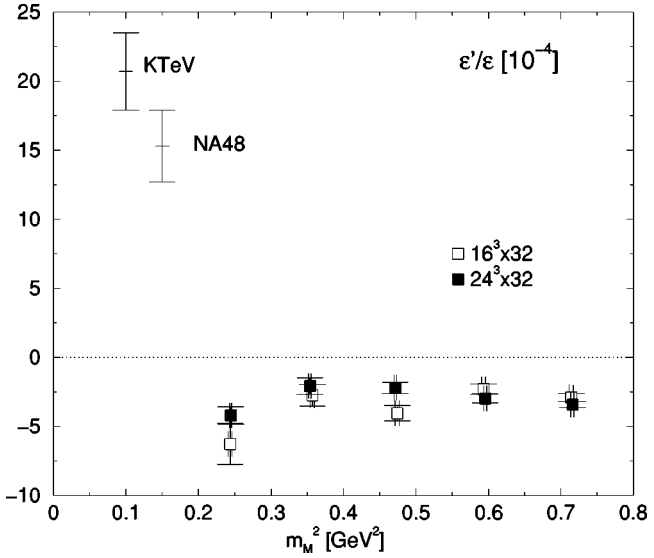

FIG. 14. ε'/ε as a function of m_M^2. Empty and filled symbols are for the spatial volume 16^3 and 24^3, respectively. Experimental values quoted in Eq. (1.4) are also shown.

$$Q_6^{(0)}=(\bar{s}_a d_b)_L[(\bar{u}_b u_a)_R+(\bar{d}_a d_b)_R+(\bar{s}_b s_a)_R], \quad \text{(A20)}$$

$$Q_7^{(0)}=\frac{1}{2}[(\bar{s}d)_L(\bar{u}u)_R-(\bar{s}u)_L(\bar{u}d)_R-(\bar{s}d)_L(\bar{s}s)_R], \quad \text{(A21)}$$

$$Q_8^{(0)}=\frac{1}{2}[(\bar{s}_a d_b)_L(\bar{u}_b u_a)_R-(\bar{s}_a u_b)_L(\bar{u}_b d_a)_R -(\bar{s}_a d_b)_L(\bar{s}_b s_a)_R], \quad \text{(A22)}$$

$$Q_9^{(0)}=\frac{1}{2}[(\bar{s}d)_L(\bar{u}u)_L-(\bar{s}u)_L(\bar{u}d)_L-(\bar{s}d)_L(\bar{s}s)_L], \quad \text{(A23)}$$

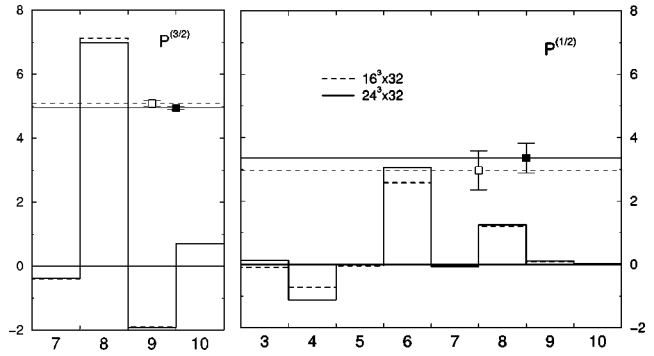

FIG. 15. Breakdown of $P^{(3/2)}$ (left) and $P^{(1/2)}$ (right) into contributions from the operators $Q_i (i=3,\ldots,10)$ at $m_f a=0.03$. Data points placed on horizontal lines show total values and errors. The solid and dashed lines are for the spatial volume 24^3 and 16^3, respectively.

$$Q_{10}^{(0)}=\frac{1}{2}[(\bar{s}_a d_b)_L(\bar{u}_b u_a)_L-(\bar{s}_a u_b)_L(\bar{u}_b d_a)_L -(\bar{s}_a d_b)_L(\bar{s}_b s_a)_L], \quad \text{(A24)}$$

$\Delta I=3/2$:

$$Q_1^{(2)}=Q_2^{(2)}=\frac{1}{3}[(\bar{s}d)_L(\bar{u}u)_L+(\bar{s}u)_L(\bar{u}d)_L-(\bar{s}d)_L(\bar{d}d)_L], \quad \text{(A25)}$$

$$Q_3^{(2)}=Q_4^{(2)}=Q_5^{(2)}=Q_6^{(2)}=0, \quad \text{(A26)}$$

$$Q_7^{(2)}=\frac{1}{2}[(\bar{s}d)_L(\bar{u}u)_R+(\bar{s}u)_L(\bar{u}d)_R-(\bar{s}d)_L(\bar{d}d)_R], \quad \text{(A27)}$$

$$Q_8^{(2)}=\frac{1}{2}[(\bar{s}_a d_b)_L(\bar{u}_b u_a)_R+(\bar{s}_a u_b)_L(\bar{u}_b d_a)_R -(\bar{s}_a d_b)_L(\bar{d}_b d_a)_R], \quad \text{(A28)}$$

$$Q_9^{(2)}=Q_{10}^{(2)}=\frac{3}{2}Q_1^{(2)}, \quad \text{(A29)}$$

where color indices are understood within each current in the operators with two color traces. The equivalence between $Q_1^{(2)}$ and $Q_2^{(2)}$ is valid due to Fierz rearrangement, hence $Q_9^{(2)}=Q_{10}^{(2)}$ follows.

APPENDIX B: EXPERIMENTAL INPUT PARAMETERS

We collect the input parameters which were used in our numerical calculation [51,52].

Quark mass: $m_u=5$ MeV, $m_d=8$ MeV, (B1)

$m_s=120$ MeV, $m_c=1.3$ GeV, (B2)

$m_b=4.2$ GeV, $m_t=170$ GeV. (B3)

Meson mass: $m_\pi=139.6$ MeV, $m_K=497.7$ MeV. (B4)

Decay constant: $f_\pi=92.4$ MeV, $f_K=113.1$ MeV. (B5)

Coupling constant: $\alpha\equiv e^2/(4\pi)=1/129$ (at $\mu=m_W$), (B6)

$$G_F\equiv\frac{\sqrt{2}g_2{}^2}{8m_W^2}=1.166\times10^{-5}\ \text{GeV}^{-2} \quad \text{(B7)}$$

$(m_W=80.2$ GeV).

TABLE XVII. Values of $P^{(1/2)}$, $P^{(3/2)}$, and ε'/ε at each $m_f a$ for both lattice volumes, with $\Lambda^{(4)}_{\overline{\rm MS}}=325$, 215, and 435 MeV.

	$16^3\times 32$			$24^3\times 32$		
	$P^{(1/2)}$	$P^{(3/2)}$	$\varepsilon'/\varepsilon[10^{-4}]$	$P^{(1/2)}$	$P^{(3/2)}$	$\varepsilon'/\varepsilon[10^{-4}]$
$\Lambda^{(4)}_{\overline{\rm MS}}=325$ MeV						
0.02	0.1(1.2)	4.93(11)	−6.3(1.5)	1.69(50)	4.923(45)	−4.21(64)
0.03	2.97(61)	5.084(88)	−2.74(78)	3.36(47)	4.944(49)	−2.06(60)
0.04	2.19(44)	5.291(70)	−4.03(56)	3.50(33)	5.200(41)	−2.21(41)
0.05	3.65(29)	5.416(59)	−2.30(37)	3.19(26)	5.470(37)	−2.96(33)
0.06	3.42(22)	5.657(53)	−2.90(28)	3.01(19)	5.632(35)	−3.41(24)
$\Lambda^{(4)}_{\overline{\rm MS}}=215$ MeV						
0.02	0.06(94)	3.713(87)	−4.7(1.2)	1.34(41)	3.707(36)	−3.07(52)
0.03	2.38(50)	3.815(70)	−1.86(63)	2.70(38)	3.701(39)	−1.31(49)
0.04	1.74(36)	3.962(56)	−2.89(45)	2.81(26)	3.892(33)	−1.40(33)
0.05	2.93(24)	4.049(47)	−1.45(30)	2.56(21)	4.094(27)	−1.99(27)
0.06	2.75(18)	4.228(42)	−1.92(22)	2.41(16)	4.211(28)	−2.34(19)
$\Lambda^{(4)}_{\overline{\rm MS}}=435$ MeV						
0.02	0.1(1.4)	6.16(13)	−7.8(1.8)	2.05(61)	6.150(54)	−5.33(78)
0.03	3.63(75)	6.36(11)	−3.56(95)	4.09(58)	6.197(58)	−2.74(73)
0.04	2.67(54)	6.629(84)	−5.15(68)	4.26(40)	6.518(50)	−2.93(50)
0.05	4.43(36)	6.790(71)	−3.06(46)	3.88(32)	6.853(44)	−3.87(40)
0.06	4.16(27)	7.091(64)	−3.82(34)	3.65(24)	7.059(42)	−4.43(29)

Quantities relevant

to Kaon decays: $\quad \mathrm{Re}\,A_0 = 33.3\times 10^{-8}$ GeV, (B8)

$$\mathrm{Re}\,A_2 = 1.50\times 10^{-8}\ \text{GeV}, \tag{B9}$$

$$|\omega| = 0.045, \tag{B10}$$

$$\Omega_{\eta+\eta'} = 0.25, \tag{B11}$$

$$|\varepsilon| = 2.280\times 10^{-3}, \tag{B12}$$

CKM elements: $\quad |V_{\rm us}| = 0.22,\ |V_{\rm ud}| = 0.974,$ (B13)

$$\mathrm{Im}(V_{\rm ts}^* V_{\rm td}) = 1.3\times 10^{-4}, \tag{B14}$$

$$\mathrm{Re}\,\tau = -\mathrm{Re}\left(\frac{V_{\rm ts}^* V_{\rm td}}{V_{\rm us}^* V_{\rm ud}}\right) = 0.002. \tag{B15}$$

APPENDIX C: RENORMALIZATION FACTORS AND RG-EVOLUTION MATRIX

In this appendix, we summarize the renormalization factors and the RG-evolution matrix, and calculate their numerical values for our choice of parameters. Throughout this paper, we employ the perturbative calculation in $\overline{\rm MS}$ scheme with NDR.

The renormalization formula has the form

$$\langle Q_i\rangle^{\overline{\rm MS}}(q^*) = \mathcal{Z}^g_{ij}(q^*a)\langle Q^{\rm latt}_j\rangle(1/a) + \mathcal{Z}^{\rm pen}_i(q^*a)\langle Q^{\rm latt}_{\rm pen}\rangle(1/a), \tag{C1}$$

where

$$Q^{\rm latt}_{\rm pen} \equiv Q_4 + Q_6 - \frac{(Q_3+Q_5)}{N_c} \quad (N_c = 3{:}\ \text{No. of color}) \tag{C2}$$

is the sum of contributions from penguin operators. Since our matrix elements are obtained in the form of propagator ratios, $\mathcal{Z}^g$ and $\mathcal{Z}^{\rm pen}$ are also ratios of the renormalization factors Z^g_{ij} and $Z^{\rm pen}_i$ calculated from corresponding vertex functions and that of the local axial current Z_A [43]:

$$\mathcal{Z}^g_{ij} = \frac{Z^g_{ij}}{Z_A^2}, \quad \mathcal{Z}^{\rm pen}_i = \frac{Z^{\rm pen}_i}{Z_A^2}. \tag{C3}$$

The diagonal parts Z^g_{ii} are given by

$$Z_{ii}^{g}=\begin{cases} 1+\dfrac{g^2}{16\pi^2}\left[\dfrac{3}{N_c}\ln(q^*a)^2+\dfrac{z_++z_-}{2}\right], & i=1,2,3,4,9,10, \\ 1+\dfrac{g^2}{16\pi^2}\left[-\dfrac{3}{N_c}\ln(q^*a)^2+z_1-v_{21}\right], & i=5,7, \\ 1+\dfrac{g^2}{16\pi^2}\left[\dfrac{3(N_c^2-1)}{N_c}\ln(q^*a)^2+z_2+v_{21}\right], & i=6,8, \end{cases} \tag{C4}$$

while for off-diagonal parts, one has

$$Z_{ij}^{g}=\begin{cases} \dfrac{g^2}{16\pi^2}\left[-\dfrac{3}{N_c}\ln(q^*a)^2+\dfrac{z_+-z_-}{2}\right], & (i,j)=(1,2),(2,1),(3,4), \\ & (4,3),(9,10),(10,9), \\ \dfrac{g^2}{16\pi^2}\left[3\ln(q^*a)^2+\dfrac{z_2-z_1+v_{21}-v_{12}}{N_c}\right], & i=(5,6),(7,8), \\ -\dfrac{g^2}{16\pi^2}N_c v_{21}, & i=(6,5),(8,7), \\ 0, & \text{others}. \end{cases} \tag{C5}$$

Similarly the contributions from the penguin operators [45] are given by

$$Z_i^{\rm pen}=\frac{g^2}{16\pi^2}\frac{C_i}{3}[-\ln(q^*a)^2+z_i^{\rm pen}], \tag{C6}$$

where $C_2=1, C_3=2, C_4=C_6=N_f, C_8=C_{10}=N_u-N_d/2, C_9=-1$, and $C_i=0$ for other i with N_f, N_u, N_d being the number of flavors, up-like quarks, and down-like quarks in Q_i's, and $z_i^{\rm pen}$ are constants. In our calculation, we should set $N_f=3, N_u=1$, and $N_d=2$. Finally the axial vector renormalization constant has the form

$$Z_A=1+\frac{g^2}{12\pi^2}z_A. \tag{C7}$$

In the above $z_\pm, z_1, z_2, v_{12}, v_{21}$, and z_A are constants depending on the choices of simulation parameters and renormalization scheme. With the use of mean field improvement at one-loop level, we obtain the following values [46] at $\beta=2.6$ and $M=1.8$ for the RG-improved gauge action:

$$g^2\equiv g^2_{\overline{\rm MS}}(1/a)=2.273, \tag{C8}$$

$$\tilde{M}=1.419\,79, \tag{C9}$$

$$z_A=-4.6930, \tag{C10}$$

$$z_+=-13.612,\quad z_-=-10.319, \tag{C11}$$

$$z_1=-10.063,\quad z_2=-16.125, \tag{C12}$$

$$v_{12}=8,\quad v_{21}=1, \tag{C13}$$

$$z_i^{\rm pen}=\begin{cases} 4.494 & (\text{for } i=2,3,5,7,9) \\ 3.494 & (\text{for } i=4,6,8,10). \end{cases} \tag{C14}$$

From the definition of $Q^{\rm pen}$, $Z_i^{\rm pen}$ can be written in the form of a 10×10 matrix $\hat{Z}^{\rm pen}$, defined as $\hat{Z}^{\rm pen}_{i3}=\hat{Z}^{\rm pen}_{i5}=-z_i^{\rm pen}/N_c, \hat{Z}^{\rm pen}_{i4}=\hat{Z}^{\rm pen}_{i6}=z_i^{\rm pen}$, and $\hat{Z}^{\rm pen}_{ij}=0$ for other j. The renormalization factor can then be summarized as a 10×10 matrix given by

$\mathcal{Z}^g + \hat{\mathcal{Z}}^{\rm pen}$

$$= \begin{bmatrix}
0.9997 & -0.0350 & 0 & 0 & 0 & 0 & 0 & 0 & 0 & 0 \\
-0.0350 & 0.9997 & -0.0106 & 0.0318 & -0.0106 & 0.0318 & 0 & 0 & 0 & 0 \\
0 & 0 & 0.9785 & 0.0287 & -0.0212 & 0.0636 & 0 & 0 & 0 & 0 \\
0 & 0 & -0.0597 & 1.0739 & -0.0247 & 0.0742 & 0 & 0 & 0 & 0 \\
0 & 0 & 0 & 0 & 1.0154 & -0.0924 & 0 & 0 & 0 & 0 \\
0 & 0 & -0.0247 & 0.0742 & -0.0884 & 1.0190 & 0 & 0 & 0 & 0 \\
0 & 0 & 0 & 0 & 0 & 0 & 1.0154 & -0.0924 & 0 & 0 \\
0 & 0 & 0 & 0 & 0 & 0 & -0.0637 & 0.9448 & 0 & 0 \\
0 & 0 & 0.0106 & -0.0318 & 0.0106 & -0.0318 & 0 & 0 & 0.9997 & -0.0350 \\
0 & 0 & 0 & 0 & 0 & 0 & 0 & 0 & -0.0350 & 0.9997
\end{bmatrix}. \tag{C15}$$

For the derivation of the RG-evolution matrix, we start with constructing the renormalization group equation (RGE) of $W_i(\mu)$'s, and hence of $U(\mu,1/a)$'s. If we write the renormalization of Q_i as $Q_i^{(0)}=Z_{ij}Q_j$ where the superscript (0) indicates the value at tree level, RGE for Q_i's are readily obtained as

$$\frac{d}{d\ln\mu}Q_i = -\gamma_{ij}Q_j, \quad \gamma \equiv \left(Z^{-1}\frac{d}{d\ln\mu}Z\right). \tag{C16}$$

On the other hand, interpreting W_i's as coupling constants in the effective Hamiltonian, renormalization of W_i's is possible, $W_i^{(0)}=Z_{ij}^c W_j$, in place of that of Q_i's. From the equivalence of these renormalizations, $Z^c=(Z^{-1})^T$ follows. Therefore using Eq. (C16) we obtain

$$\frac{d}{d\ln\mu}W_i = \gamma_{ij}^T W_j,$$

hence

$$\frac{d}{d\ln\mu}U_{ij}(\mu,1/a) = (\gamma^T)_{ik}U_{kj}(\mu,1/a). \tag{C17}$$

Using the 10×10 anomalous dimension matrix γ, defined in Eq. (C16), the RGE for $U(\mu,1/a)$ has been solved for the QCD β function and anomalous dimension γ calculated at next to leading order [53,54]:

$$\beta(g) = -\beta_0\frac{g^3}{16\pi^2} - \beta_1\frac{g^5}{(16\pi^2)^2}, \tag{C18}$$

$$\beta_0 = \frac{11N_c-2N_f}{3},$$

$$\beta_1 = \frac{34}{3}N_c^2 - \frac{10}{3}N_cN_f - 2C_FN_f, \tag{C19}$$

$$\gamma(\alpha_S,\alpha) = \gamma_S(g^2) + \frac{\alpha}{4\pi}\Gamma(g^2), \tag{C20}$$

$$\gamma_S(g^2) = \gamma_S^{(0)}\frac{\alpha_S}{4\pi} + \gamma_S^{(1)}\left(\frac{\alpha_S}{4\pi}\right)^2, \tag{C21}$$

$$\Gamma(g^2) = \gamma_e^{(0)} + \frac{\alpha_S}{4\pi}\gamma_{\rm se}^{(1)}. \tag{C22}$$

The solution at this order is written as

$$U(\mu_1,\mu_2,\alpha) = U(\mu_1,\mu_2) + \frac{\alpha}{4\pi}R(\mu_1,\mu_2). \tag{C23}$$

Using the matrix V that diagonalizes the $\gamma_S^{(0)T}$, we obtain $\mathrm{diag}[\gamma_{Di}^{(0)}]=V^{-1}\gamma^{(0)T}V$ and $G=V^{-1}\gamma^{(1)T}V$. Then,

$$U(\mu_1,\mu_2) = U^{(0)}(\mu_1,\mu_2) + \frac{\alpha_S(\mu_1)}{4\pi}JU^{(0)}(\mu_1,\mu_2) - U^{(0)}(\mu_1,\mu_2)\frac{\alpha_S(\mu_2)}{4\pi}J, \tag{C24}$$

$$U^{(0)}(\mu_1,\mu_2)=V\left(\frac{\alpha_S(\mu_2)}{\alpha_S(\mu_1)}\right)^{\gamma_D^{(0)}/2\beta_0}V^{-1}, \tag{C25}$$

$$J=VHV^{-1}, \tag{C26}$$

$$H_{ij}=\delta_{ij}\gamma_{Di}^{(0)}\frac{\beta_1}{2\beta_0^2}-\frac{G_{ij}}{2\beta_0+\gamma_{Di}^{(0)}-\gamma_{Dj}^{(0)}}. \tag{C27}$$

Moreover, with $M^{(0)}\equiv V^{-1}\gamma_e^{(0)T}V$,

$$R(\mu_1,\mu_2)=-\frac{2\pi}{\beta_0}V\left[K^{(0)}(\mu_1,\mu_2)+\frac{1}{4\pi}\sum_{i=1}^{3}K_i^{(1)}(\mu_1,\mu_2)\right]V^{-1}, \tag{C28}$$

$$K^{(0)}(\mu_1,\mu_2)_{ij}=\frac{2\beta_0 M_{ij}^{(0)}}{\gamma_{Di}^{(0)}-\gamma_{Dj}^{(0)}-2\beta_0}\times\left[\left(\frac{\alpha_S(\mu_2)}{\alpha_S(\mu_1)}\right)^{\gamma_{Dj}^{(0)}/2\beta_0}\frac{1}{\alpha_S(\mu_1)}-\left(\frac{\alpha_S(\mu_2)}{\alpha_S(\mu_1)}\right)^{\gamma_{Di}^{(0)}/2\beta_0}\frac{1}{\alpha_S(\mu_2)}\right], \tag{C29}$$

$$K_1^{(1)}(\mu_1,\mu_2)_{ij}=\frac{2\beta_0 M_{ij}^{(1)}}{\gamma_{Di}^{(0)}-\gamma_{Dj}^{(0)}}\left[\left(\frac{\alpha_S(\mu_2)}{\alpha_S(\mu_1)}\right)^{\gamma_{Dj}^{(0)}/2\beta_0}-\left(\frac{\alpha_S(\mu_2)}{\alpha_S(\mu_1)}\right)^{\gamma_{Di}^{(0)}/2\beta_0}\right], \tag{C30}$$

$$M^{(1)}=V^{-1}\left(\gamma_{\rm se}^{(1)T}-\frac{\beta_1}{\beta_0}\gamma_e^{(0)T}+[\gamma_e^{(0)T},J]\right)V, \tag{C31}$$

$$K_2^{(1)}(\mu_1,\mu_2)=-\alpha_S(\mu_2)K^{(0)}(\mu_1,\mu_2)H, \tag{C32}$$

$$K_3^{(1)}(\mu_1,\mu_2)=\alpha_S(\mu_1)HK^{(0)}(\mu_1,\mu_2), \tag{C33}$$

where $\mu_1=\mu_c=1.3$ GeV, and $\mu_2=1/a$.

Using the value of the strong coupling constant $\alpha_S^{\overline{\rm MS}}(1/a)=0.301\,71$ and $\alpha_S^{\overline{\rm MS}}(1.3\ {\rm GeV})=0.396\,01$ with $\Lambda_{\overline{\rm MS}}^{(3)}=372$ MeV, together with γ functions presented in Ref. [41], we obtain the matrix $U(m_c,1/a,\alpha)$ given in Eq. (C23) and the RG-evolution matrix:

$$[U^{-1}(m_c,1/a)]^T=\begin{bmatrix}
0.9738 & 0.0730 & 0.0035 & -0.0003 & -0.0033 & -0.0002 & 0.0005 & 0 & 0.0005 & 0.0001\\
0.0731 & 0.9736 & -0.0024 & 0.0149 & -0.0053 & 0.0116 & 0.0002 & 0 & 0.0001 & 0.0001\\
0 & 0 & 0.9794 & 0.1043 & -0.0212 & 0.0247 & -0.0002 & 0 & -0.0006 & -0.0001\\
0 & 0 & 0.0731 & 1.0105 & -0.0186 & 0.0306 & -0.0005 & 0 & -0.0004 & 0\\
0 & 0 & -0.0083 & -0.0065 & 1.0465 & -0.0996 & 0.0005 & 0 & 0 & 0\\
0 & 0 & -0.0090 & 0.0228 & -0.0421 & 0.7878 & 0 & 0.0007 & 0 & 0\\
0 & 0 & 0 & 0 & 0.0002 & 0 & 1.0349 & -0.0929 & 0.0008 & 0\\
0 & 0 & 0 & 0 & 0 & 0.0004 & -0.0367 & 0.7602 & 0.0001 & -0.0001\\
0 & 0 & 0.0021 & -0.0149 & 0.0053 & -0.0116 & 0.0009 & 0.0001 & 0.9750 & 0.0731\\
0 & 0 & -0.0035 & -0.0001 & 0.0032 & 0.0002 & 0.0006 & 0 & 0.0736 & 0.9740
\end{bmatrix}. \tag{C34}$$

In order to check the systematic error associated with the matching procedure above, we also employ an alternative procedure in which the RG-evolution is carried out in the *quenched* theory from $\mu_2 = q^*$ to $\mu_1 = \mu_c = 1.3$ GeV where matching to the $N_f = 3$ theory is made. For the quenched RG-evolution, the two-loop anomalous dimension matrix $\gamma_S^{(1)}$ is modified according to [54]

$$[\gamma_S^{(1)}]_{\text{quenched}} = [\gamma_S^{(1)}]_{\text{full}} - \Delta\gamma_S^{(1)}, \tag{C35}$$

where $\Delta\gamma_S^{(1)} = \text{diag}[\Gamma_1, \Gamma_2, \Gamma_3, \Gamma_4, \Gamma_5]$ with the 2×2 matrices Γ_i, which are given by

$$\Gamma_1 = \Gamma_2 = \Gamma_5 = \begin{bmatrix} -\frac{2N_f}{3N_c} & \frac{2N_f}{3} \\ \frac{2N_f}{3} & -\frac{2N_f}{3N_c} \end{bmatrix}, \tag{C36}$$

$$\Gamma_3 = \Gamma_4 = \begin{bmatrix} -\frac{22N_f}{3N_c} & \frac{22N_f}{3} \\ 4N_f & \frac{20C_F N_f}{3} - \frac{4N_f}{N_c} \end{bmatrix}. \tag{C37}$$

Note that $N_f = 3$ in this case. For the gauge coupling in the quenched theory, we employ $\alpha_S^{\overline{\text{MS}}}(1/a) = 0.180\,891$ from Eq. (C8), and $\alpha_S^{\overline{\text{MS}}}(1.3\text{ GeV}) = 0.204\,39$ obtained by the two-loop running with $N_f = 0$.

[1] A. Alavi-Harati *et al.*, Phys. Rev. Lett. **83**, 22 (1999); J. Graham, "A new measurement of ε'/ε," Fermilab Seminar, 2001, http://kpasa.fnal.gov:8080/public/ktev.html

[2] V. Fanti *et al.*, Phys. Lett. B **465**, 335 (1999); G. Unal, "A new measurement of direct CP violation by NA48," CERN Particle Physics Seminar, 2001, http://www.cern.ch/NA48/

[3] M. Kobayashi and T. Maskawa, Prog. Theor. Phys. **49**, 652 (1973).

[4] For reviews, see, A.J. Buras, lectures given at the Les Houches Summer School 1998, hep-ph/9806471; lectures given at the 38th Erice International School of Subnuclear Physics, 2000, hep-ph/0101336.

[5] N. Cabibbo, G. Martinelli, and R. Petronzio, Nucl. Phys. **B244**, 381 (1984).

[6] R. Brower, M. Gavela, R. Gupta, and G. Maturana, Phys. Rev. Lett. **53**, 1318 (1984).

[7] C. Bernard, in *Gauge Theory on a Lattice: 1984*, edited by C. Zachos *et al.* (National Technical Information Service, VA, 1984).

[8] For a recent review, see L. Lellouch, Nucl. Phys. B (Proc. Suppl.) **94**, 142 (2001).

[9] D. Kaplan, Phys. Lett. B **288**, 342 (1992).

[10] Y. Shamir, Nucl. Phys. **B406**, 190 (1993).

[11] V. Furman and Y. Shamir, Nucl. Phys. **B439**, 54 (1995).

[12] For a review, see, Y. Kuramashi, Nucl. Phys. B (Proc. Suppl.) **83**, 24 (2000).

[13] L. Maiani and M. Testa, Phys. Lett. B **245**, 585 (1990).

[14] Early attempts were reviewed in, C. Bernard and A. Soni, Nucl. Phys. B (Proc. Suppl.) **9**, 155 (1989). For recent studies, see Lellouch [8].

[15] C. Bernard, T. Draper, A. Soni, H.D. Politzer, and M.B. Wise, Phys. Rev. D **32**, 2343 (1985).

[16] JLQCD Collaboration, S. Aoki *et al.*, Phys. Rev. D **58**, 054503 (1998).

[17] M. Ciuchini, E. Franco, G. Martinelli, and L. Silvestrini, Phys. Lett. B **380**, 353 (1996).

[18] L. Lellouch and M. Lüscher, Commun. Math. Phys. **219**, 31 (2001).

[19] C.-J.D. Lin, G. Martinelli, C.T. Sacharajda, and M. Testa, Nucl. Phys. **B619**, 467 (2001).

[20] R. Gupta, T. Bhattacharya, and S.R. Sharpe, Phys. Rev. D **55**, 4036 (1997).

[21] C. Donini, V. Gimenez, L. Giusti, and G. Martinelli, Phys. Lett. B **470**, 233 (1999).

[22] L. Lellouch and C.-J. David Lin, Nucl. Phys. B (Proc. Suppl.) **73**, 312 (1999).

[23] D. Pekurovsky and G. Kilcup, Phys. Rev. D **64**, 074502 (2001); D. Pekurovsky, Ph.D. thesis, Ohio State University, hep-lat/9909141.

[24] T. Blum and A. Soni, Phys. Rev. D **56**, 174 (1997); Phys. Rev. Lett. **79**, 3595 (1997).

[25] S. Aoki, T. Izubuchi, Y. Kuramashi, and Y. Taniguchi, Phys. Rev. D **62**, 094502 (2000).

[26] CP-PACS Collaboration, A. Ali Khan *et al.*, Phys. Rev. D **63**, 114504 (2001).

[27] T. Blum *et al.*, Phys. Rev. D (to be published), hep-lat/0007038.

[28] CP-PACS Collaboration, A. Ali Khan *et al.*, Phys. Rev. D **64**, 114506 (2001).

[29] JLQCD Collaboration, S. Aoki *et al.*, Phys. Rev. Lett. **81**, 1778 (1998); Phys. Rev. D **60**, 034511 (1999).

[30] CP-PACS Collaboration, A. Ali Khan *et al.*, Nucl. Phys. B (Proc. Suppl.) **94**, 283 (2001).

[31] RBC Collaboration, T. Blum *et al.*, Nucl. Phys. B (Proc. Suppl.) **94**, 291 (2001).

[32] RBC Collaboration, R.D. Mawhinney, Nucl. Phys. B (Proc. Suppl.) **94**, 315 (2001).

[33] P. Vranas, Nucl. Phys. B (Proc. Suppl.) **94**, 177 (2001).

[34] J. Bijnens and M.B. Wise, Phys. Lett. **137B**, 245 (1984).

[35] V. Cirigliano and E. Golowich, Phys. Lett. B **475**, 351 (2000).

[36] N. Ishizuka (unpublished).

[37] Y. Iwasaki, report, UTHEP-118, 1983; Nucl. Phys. **B258**, 141 (1985).

[38] Y. Iwasaki, K. Kanaya, T. Kaneko, and T. Yoshie, Phys. Rev. D **56**, 151 (1997).

[39] CP-PACS Collaboration, A. Ali Khan *et al.*, Nucl. Phys. B (Proc. Suppl.) **83-84**, 176 (2000).

[40] CP-PACS Collaboration, M. Okamoto *et al.*, Phys. Rev. D **60**, 094510 (1999).
[41] For a review, see, G. Buchalla, A.J. Buras, and M.E. Lautenbacher, Rev. Mod. Phys. **68**, 1125 (1996).
[42] See, for example, S. Bethke, J. Phys. G **26**, R27 (2000).
[43] S. Aoki, T. Izubuchi, Y. Kuramashi, and Y. Taniguchi, Phys. Rev. D **59**, 094505 (1999).
[44] S. Aoki, T. Izubuchi, Y. Kuramashi, and Y. Taniguchi, Phys. Rev. D **60**, 114504 (1999).
[45] S. Aoki and Y. Kuramashi, Phys. Rev. D **63**, 054504 (2001).
[46] S. Aoki, T. Izubuchi, Y. Kuramashi, and Y. Taniguchi, Phys. Rev. D **67**, 094502 (2003).
[47] M. Golterman and E. Pallante, J. High Energy Phys. **08**, 023 (2000).
[48] J. Donogue and E. Golowich, Phys. Lett. B **478**, 172 (2000); see V. Cirigliano, J. Donogue, E. Golowich, and K. Maltman, *ibid.* **522**, 245 (2001) for the latest result.
[49] M. Golterman and E. Pallante, J. High Energy Phys. **10**, 037 (2001).
[50] T. Bhattacharya *et al.*, Nucl. Phys. B (Proc. Suppl.) **106**, 311 (2002).
[51] Particle Data Group, D.E. Groom *et al.*, Eur. Phys. J. C **15**, 1 (2000).
[52] S. Bosch *et al.*, Nucl. Phys. **B565**, 3 (2000).
[53] G. Altarelli, G. Curci, G. Martinelli, and S. Petrarca, Nucl. Phys. **B187**, 461 (1981); M. Ciuchini, E. Franco, G. Martinelli, and L. Reina, Phys. Lett. B **301**, 263 (1993); Nucl. Phys. **B415**, 403 (1994).
[54] A.J. Buras and P.H. Weisz, Nucl. Phys. **B333**, 66 (1990); A.J. Buras, M. Jamin, M.E. Lautenbacher, and P.H. Weisz, *ibid.* **B370**, 69 (1992); **B375**, 501 (1992); **B400**, 37 (1993); A.J. Buras, M. Jamin, and M.E. Lautenbacher, *ibid.* **B400**, 75 (1993); **B408**, 209 (1993).